UNIVERSITÀ
DEGLI STUDI
DI PADOVA

TÉCNICO
LISBOA

UNIVERSITÀ DEGLI STUDI DI NAPOLI
FEDERICO II

Università degli Studi di Padova
Centro Ricerche Fusione (**CRF**)

Universidade de Lisboa
Instituto Superior Técnico **(IST)**

Università degli Studi di Napoli Federico II

JOINT RESEARCH DOCTORATE IN FUSION SCIENCE AND ENGINEERING
Cycle XXXI

Neutral beam fast particle physics in fusion plasma integrated scenarios

Coordinator: Prof. Paolo BETTINI
Supervisor: Dr. Tommaso BOLZONELLA

Ph.D. Student: Matteo VALLAR

Padova, November 2018

Abstract

Neutral beam injection heating is one of the most reliable ways to heat a plasma up to the temperatures needed to achieve steady-state thermonuclear fusion. This system injects neutral particles with energy much higher than the bulk ion energy, introducing a population of energetic particles which collide with the plasma ions and electrons. In this way energy and momentum are transferred to the plasma giving as final result an increase of the target plasma temperature and, depending on the beam characteristics, possible modifications of its flow and current profile.

Numerical modelling of the behaviour of fast particles in tokamak plasma is the subject of this thesis. Analytical and Monte Carlo models have been applied to different devices (RFX-mod, JT-60 SA and TCV) in order to study the impact of these particles in both inductive (standard) and non-inductive (advanced) scenarios. Comparison between the different codes have been made in order to assess if the different models apply correctly to the cases studied.

RFX-mod device is under modification and the installation of a neutral beam injector (with fixed parameters and geometry) is in the upgrade hypothesis. The impact of energetic particles in RFX-mod tokamak plasmas is discussed in this work using METIS fast tokamak simulator and compared with NUBEAM Monte Carlo code.

The impact of energetic particles in JT-60 SA superconducting tokamak is studied with ASCOT Monte Carlo orbit solver. This device relies on a wide and flexible set of beams for plasma heating and current drive, both for standard and advanced scenarios. The behaviour of the fast particles in JT-60 SA standard and advanced tokamak plasmas is analysed, showing the reliability of the neutral beam system in this device.

Neutral beam injection heating in TCV is the last topic studied in this thesis. The impact of electron cyclotron wave injection heating on energetic particles behaviour has been studied in advanced tokamak scenarios, where the expected performances are not achieved using the combination of the two heating systems. Comparison between ASCOT and NUBEAM code is performed in order to check which of the two codes is most suitable for TCV and the two codes are applied for a reference case.

nuclear fusion, tokamak, additional heating, neutral beam injection, numerical modelling, RFX-mod, JT60SA, TCV

Sinossi

L'iniezione di fasci di neutri è uno dei metodi più utilizzati per riscaldare un plasma fino alle temperature necessarie per ottenere la fusione termonucleare controllata in modo stazionario. Questo metodo consiste in iniettare particelle neutri (atomi) con energia significativamente più alta della temperatura del plasma bersaglio, introducendo così una popolazione di particelle energetiche che collidono con gli elettroni e gli ioni presenti nel plasma. In questo modo vengono trasferiti energia e momento al plasma, ottenendo come risultato di aumentare la temperatura del plasma. In base alle caratteristiche del fascio, questo processo può anche modificare il profilo di corrente del plasma.

L'argomento di questa tesi è la modellizzazione numerica del comportamento delle particelle veloci in plasmi di tipo tokamak. Modelli analitici e Monte Carlo sono stati applicati su diversi esperimenti (RFX-mod, JT-60 SA e TCV) per studiare l'impatto di queste particelle sia in scenari induttivi (standard) che non induttivi (avanzati).

L'esperimento RFX-mod sta subendo delle modifiche e l'installazione di un fascio di neutri (a parametri e geometria di iniezione fissati) è considerato come ipotesi per l'upgrade. L'impatto delle particelle energetiche sui plasmi tokamak di RFX-mod è stato studiato usando il simulatore veloce METIS.

L'impatto delle particelle energetiche sul tokamak superconduttivo JT-60SA è stato studiato con il codice Monte Carlo ASCOT. Questo esperimento si basa su un vasto e flessibile sistema di iniettori di neutri per il riscaldamento del plasma e produzione di corrente toroidale per scenari sia avanzati che standard. Il comportamento delle particelle veloce in plasmi tokamak standard e avanzati su JT-60SA è studiato, mostrando l'affidabilità dei fasci di neutri disegnati per questo esperimento.

L'ultimo argomento di questa tesi è l'iniezione di neutri in TCV. Combinando l'azione di fasci di neutri e l'iniezione di onde alla frequenza di risonanza elettronica non sono state raggiunte le performances desiderate; l'impatto di questo tipo di onde sul plasma e il conseguente deterioramento del confinamento delle particelle veloce è studiato in scenari tokamak avanzati. L'iniettore di neutri di TCV è stato installato tre anni fa e il processo di caratterizzazione e ottimizzazione è ancora in corso.

fusione nucleare, tokamak, riscaldamenti addizionali, iniezioni di fasci di neutri, modellizzazione numerica, RFX-mod, JT60SA, TCV

Resumo

O aquecimento por injeção de feixes de neutros é um dos métodos mais fiáveis para aquecer um plasma até às temperaturas necessárias para atingir fusão termonuclear estacionária. Este tipo de sistema injeta neutros com energias muito superiores à energia dos iões que constituem o grosso do plasma, introduzindo uma população de partículas energéticas que, colidindo com os iões e electrões do plasma, transmite a energia ao plasma. Adicionalmente, esta população de partículas energéticas também induz corrente no plasma, contribuindo para a manutenção da descarga.

O tema central desta tese incide na modelização numérica do comportamento de partículas rápidas num plasma de Tokamak. Códigos analíticos e de numéricos de Monte Carlo foram aplicados a diferentes máquinas (RFX-mod, JT-60 SA and TCV) com vista a estudar o impacto destas partículas em cenários de operação indutivos (cenário standard) e não indutivos (avançado).

A máquina RFX-mod está a ser melhorada e a instalação de injectores de feixes neutros (com parâmetros e geometria fixos) é uma das possíveis melhorias. Deste modo, o impacto das partículas energéticas nos plasmas do RFX-mod é discutida neste trabalho usando o código analítico METIS.

O impacto de partículas energéticas no tokamak superconductor JT-60SA é estudado com o código de Monte Carlo ASCOT. Neste Tokamak, o aquecimento do plasma e a geração de corrente, seja em cenário de operação standard ou avançado, é garantido em grande parte por um conjunto de feixes de injeção de neutros. Neste trabalho, a dinâmica das partículas rápidas nos cenários standard e avançado do JT-60SA é analisada, evidenciando a fiabilidade do sistema de injeção de neutros no Tokamak.

Um injector de feixes neutros foi instalado no Tokamak TCV há três anos. Este feixe é importante dado que deposita potência predominantemente nos iões e permite alargar o regime de operação do tokamak. Nesta tese, após uma revisão da condição atual do feixe de neutros e da operação com ele realizada nos últimos três anos, é feito um estudo sobre o impacto do aquecimento por injeção de ondas electro-ciclotrónicas em partículas energéticas em cenários de operação avançados.

Acknowledgements

I would like to thank in first place my family: my father Bepi, my mother Michela, my sister Chiara, Otto, my uncle Osvaldo and my aunt Bianca, my grandmother Gelmina and my grandfather Bruno. Without their support and their education I wouldn't have gone this far in my life.

Thanks to my uncle and aunt Marco and Raffaella, Rino and Bruna and my cousins Giorgio, Simonetta and Lorenzo and their families for the interest they put in what I've been doing.

My supervisor Tommaso has guided me, supported me and helped me throught this Ph.D. with his guidance, his trust in my capabilities and his contacts with the fusion community allover the world and I feel grateful for this.

I'd like to thank Pietro for his scientific and personal support, his friendship and all the adventures we have experienced together.

Consorzio RFX has been a wonderful community to work into and for this I would like to thank Paolo, Marco, Dario, Sandro, Paolo, Massimo, Carla, Fulvio, Matteo, Chiara. Thanks Nicola for the activity we've carried out together. Thanks to Paolo and Fiorella for their management and supervision of the Ph.D. students in Consorzio.

The *stalla dottorandi* is the most crowded and funny place to work into I've been and for this I would like to thank Matteo, Daniele, Leonardo, Maria Giovanna, Vadim, TJ, Yang, Carlo, Oisin, Matteo, Mattia, Ferdinando, Tommaso, Dimitri, Carlo (*nel senso di Carlo Poggi*), Sylvestre, Margherita, Umberto and Marco. Thanks to the smaller Ph.D. office and in particular to Luigi, Giulio, Marco, Antonio and Domenico. For sharing this three years and the Ph.D. courses (but not only that) together, I'd like to thank Daniele, Matteo, Giuseppe, Antonio and Adriano (please notice that the order is from north to south).

Nonetheless I must anckowledge also SPC at EPFL, due of the large amount of time and activities I've done there. Thanks to the people I've worked with, in particular Alexander, Remy, Stefano, Benedikt, Olivier; and to the people that made me feel home: Francesco, Federico, Lorenzo, Cristian, Nico.

A special remark goes to the finnish community at Aalto university, in particular to Taina and Antti (and their dogs), Konsta, Jari, Otto and Paavo.

Many thanks go also to the EUROfusion community people I've worked with, in particular Gerardo, Jeronimo, Jean-François, Jorge, Rui.

Luckily during my Ph.D. I haven't only worked, but I had the possibility to spend time with true friends: thanks to Alessandro, Vincenzo, Michele, Federica, Flavia, Sara, Rosario, Stefano, Michelino, all the PopChords VBPP-PdP (in particular Mattia, Marta, Ester, Jack, Sebastiano, Caterina, Daniel, Caterina, Nicolò, Sebastiano, Giulia and Giorgia)...

...and feel home with the friends scattered around Friuli: Simone, Eleonora, Mattia, Greta, Francesco, Daniele, Giulia, Denny, Danijel, Giuseppe, Sara, Nicholas, Alice, Riccardo, Laura and Chiara.

I'd like to thank Federica for entering so gently and respectfully into my life, making it totally different.

Contents

Abstract **iii**

Sinossi **v**

Acknowledgements **ix**

1 Controlled thermonuclear fusion and magnetic confinement **1**
1.1 The human need for energy 1
1.2 Energy production 2
1.3 Nuclear fusion 3
1.4 Magnetic confinement 4
1.5 Content and structure of this work 6

2 Neutral beam injection **9**
2.1 Additional heating systems 9
2.2 Generation of fast neutrals 11
2.2.1 Source 11
2.2.2 Accelerator 12
2.2.3 Neutraliser & residual ion dump 12
2.2.4 Beam duct & beam port 12
2.3 Energetic particles ionisation and orbits in tokamak 13
2.3.1 Beam ionisation 13
2.3.2 Orbit drifts 15
E field drift 15
$\nabla\mathbf{B}$ drift 16
Curvature drift 17
2.3.3 Trapped and passing orbits 17
2.4 Energetic particles slowing down 19
2.4.1 Coulomb collisions 19
2.4.2 Fokker Plank equation 22
2.5 Losses of fast ions 24
2.6 Current drive 25
2.7 Additional effects 26
2.8 Modelling 27
2.8.1 Codes input 27
2.8.2 Monte Carlo solvers of the Fokker-Planck equation for EP physics - ASCOT and NUBEAM 28
2.9 Improved confinement: H-mode and advanced tokamak . . . 30
2.9.1 H-mode 30
2.9.2 Advanced tokamak scenarios 31

3 Predictive studies on RFX-mod discharges 33
3.1 RFX-mod and its upgrade 33
3.1.1 AIST neutral beam injector & the implementation in RFX-mod 34
3.2 METIS design of RFX-mod tokamak discharges 35
3.3 METIS predictive simulations of NBI on RFX-mod 36
3.3.1 Reference energy and power 37
3.3.2 Reduced energy and power 38
3.3.3 Power redistribution 38
3.3.4 H-mode transition 39
3.3.5 Comparisons of fast ion orbit losses between METIS and NUBEAM 40
3.4 Conclusions 41

4 Predictive NBI studies on JT-60 SA 43
4.1 Introduction 43
4.2 JT-60SA 43
4.3 JT-60 SA NBI system 44
4.3.1 Positive sourced beams 45
4.3.2 Negative sourced beams 45
4.3.3 Modelling of JT-60 SA beams 46
4.3.4 Benchmark with integrated modelling 49
4.4 Reference scenarios 50
4.5 Inductive scenarios 52
4.5.1 Low density - scenario 2 52
Ionisation 52
Particles first orbit 53
Deposition of particles, current and power 56
4.5.2 High density - scenario 3 58
Ionisation 58
Deposition of particles, current and power 59
4.6 Advanced tokamak scenarios 62
4.6.1 Hybrid scenario 62
Ionisation 63
Deposition of power, current and particles 64
4.6.2 High-β_N, full CD - scenario 5 66
Ionisation 66
Deposition of power, current and particles 67
4.7 Banana width in the different scenarios 70
4.8 Impact of Z_{eff} on NBI in JT-60SA 71
4.9 N-NBs energy scan on advanced fully-CD scenarios 74
4.10 Conclusion 75

5 NBI modelling on TCV advanced tokamak scenarios 79
5.1 TCV device 79
5.2 TCV neutral beam 80
5.2.1 NBI operation on TCV 80
5.2.2 Beam profile measurement on W target 81

5.2.3 Scenarios with NBH: ELMy H-mode 83
5.3 NBI modelling on TCV: NUBEAM and ASCOT 84
5.3.1 ASCOT beamlet-by-beamlet implementation 85
5.3.2 ASCOT-NUBEAM beam footprint benchmark 85
5.3.3 ASCOT-NUBEAM comparison on EP slowing down . 88
5.4 Advanced tokamak scenarios on TCV under the EUROfusion consortium 89
5.5 Effect of EC on TCV AT scenarios 91
5.5.1 Edge neutral pressure measurements 91
5.5.2 Impact of EC heating on plasma composition 91
5.6 EC impact on NBI-heated plasma - Shot 58823 93
5.6.1 Experimental results 93
5.6.2 Interpretative modelling with NUBEAM 93
Benchmark with experimental data 95
5.6.3 Power balance and power deposition to ions and electrons 97
5.6.4 Interpretative wall loads using ASCOT 99
5.6.5 Initial position of lost EP 101
5.7 Conclusion 104

Afterword **107**
5.8 My personal contributions and publications 108
5.8.1 Contribution and proceeding in international conferences 108
5.8.2 Publications in refereed journals 110

List of Figures

1.1 Energy consumption in the last decades. Image from [1]. . . . 1
1.2 Human Development Index against energy consumption pro capita (in kg of oil equivalent/person). Data from [2]. 2
1.3 Mix of energy sources in the last decades 2
1.4 Tokamak and stellarator devices. 5
1.5 Tokamak plasma performance in the last years, compared with other fields. Figure from [7]. 6
1.6 ITER tokamak design. The main components are labelled. Figure from [7]. 7

2.1 Heating of a tokamak. Figure from [8] 9
2.2 Neutral beam injection geometries. 10
2.3 Graphical sketch of a neutral beam. Image taken from [4]. . . 11
2.4 Neutralisation efficiency for positive and negative H/D ions with respect to energy [15] 13
2.5 Ionisation cross-sections for the main reactions between fast ions and plasma. Image from [16]. 14
2.6 Trapped (red) and passing (green) orbits. 19
2.7 Orbits of neutral-beam injected particles. The white dots are the born position. Δ is the Shafranov shift. The dotted lines represent orbits colliding with the walls. 20
2.8 Fraction of power to the different plasma species. The vertical dotted lines (from left to right) represent the tokamak TCV, ITER and JT-60SA. 23
2.9 Shielding factor for different Z_{eff} at different ϵ. Z_{beam} has been set to 1. 26
2.10 BBNBI fast ion birth profile for different amount of markers. In the small plot, the variance of the curves is shown against the number of markers in log scale. 29
2.11 Plasma pressure cartoon for different transport barriers. Green line is the mode without any transport barriers (L-mode), dotted red is the H-mode, where only the ETB is present, solid red is the case where an internal transport barrier is created. . . . 31
2.12 Safety factor profile for conventional and advanced tokamak scenarios. 32

3.1 Design of integration of NB system into RFX-mod. (a) overall design, (b) beam detail 35
3.2 Comparison between experimental data and METIS simulation. 36
3.3 Shine-through and first orbit losses as function of the densities. 37

3.4 NBI for injection energy of 25 keV. The colors label the different shots considered (blue-53% n/n_G, black-75% n/n_G, red-100% n/n_G). The grey area represents the injection window. . 38
3.5 NBI for injection energy of 15 keV. The colors label the different shots considered (blue-53% n/n_G, black-75% n/n_G, red-100% n/n_G). The grey area represents the injection window. . 39
3.6 Redistribution between ions and electrons 39
3.7 L-H transition power threshold at 25 keV 40
3.8 Power balance for UH density case ($n_e \sim n_G$) computed from METIS (left) and NUBEAM (right). The numbers refer to the total injected power (800 kW in this case). Yellow is the power lost by unconfined orbits, green is the shine-through fraction, red is the power deposited to electrons and blue is the power deposited to ions. 41

4.1 Target performance of JT-60SA device [59]. 44
4.2 JT-60SA NB injection geometry 45
4.3 Grids of JT-60SA PNBs and NNBs 47
4.4 PNBs modelling grids 47
4.5 Zoom on a grid 48
4.6 NNBs modelling grids 48
4.7 Comparison of beam attenuation computed by NEMO (red) and BBNBI (blue) 49
4.8 Comparison of slowing-down quantity computed by ASCOT (solid lines) and SPOT (dotted lines). 50
4.9 Magnetic configuration for full I_p reference scenario. Left: poloidal flux map, centre: safety factor profile, right: toroidal magnetic field profile 52
4.10 Kinetic profiles for the two cases with full I_p 52
4.11 Fast ion birth profile for full I_p reference scenario, low density. 53
4.12 Ionisation of NNBs for low-density full I_p scenario. Colormap represents the number of markers 54
4.13 Ionisation of all the beams for low-density full I_p scenario. Colormap represents the number of markers 54
4.14 JT60-SA losses to the wall 55
4.15 Initial position of the lost particles in (ρ,ξ) and (R, Z) spaces . 55
4.16 Trapped fraction for positive beams 56
4.17 Power density coming from NBI 56
4.18 Pressure and current density profile from EP. 57
4.19 2D steady-state distribution function for scenario 2 58
4.20 Fast ion birth profile for full I_p reference scenario, high density. 59
4.21 Initial ρ position for NNB-injected particles in trapped orbits in the case of scenario 2 (black) and scenario 3 (red) 60
4.22 Power density coming from NBI 60
4.23 Pressure and current density profile from EP. 60
4.24 2D steady-state distribution function for scenario 3 61
4.25 Magnetic field for hybrid scenario 62
4.26 Kinetic profiles for hybrid scenario 63

4.27 Fast ion birth profile for scenario 4 63
4.28 Power density coming from NBI 64
4.29 Pressure and current density profile from EP. 65
4.30 2D steady-state distribution function for scenario 3 65
4.31 Magnetic field for full CD scenario 66
4.32 Kinetic profiles for full CD scenario 66
4.33 Fast ion birth profile for scenario 5 67
4.34 Power density from NBI 68
4.35 Pressure and current density profile from EP. 68
4.36 2D steady-state distribution function for scenario 5 69
4.37 Histograms with orbit width of the positive beam markers in the different scenarios: 2 (black), 3(light blue), 4 (red), 5(blue) . 70
4.38 Histograms with orbit width of the negative beam markers in the different scenarios: 2 (black), 3(light blue), 4 (red), 5(blue) . 71
4.39 Impurity content input for the scan. Black line is the reference case (constant Z_{EFF} over radius), blue line refers to the case considering impurity accumulation in the core, red line refers to the case considering edge accumulation of the impurities. . 72
4.40 Fast ion birth profile at different Z_{eff} 72
4.41 Power density from NBI to plasma ions 73
4.42 Pressure and current density profile from EP. 73
4.43 NBI deposition at different N-NB energies 74

5.1 Photo of TCV device 79
5.2 Design of heating beam injection on TCV. 80
5.3 NBH in TCV in the last 3 years: fraction of NB shots vs acceleration voltage ΔV (beam energy) and total injected energy E_{TOT} per shot 81
5.4 Neutral power (i.e. power of the neutralized ions extracted from the source) and power in TCV (accounting for beam duct losses) as function of energy. The maximum perveance is achieved at each different energy. 82
5.5 Beam divergence modeled and measured 83
5.6 Example of ELMy H-mode obtained with the additional power of the beam. 83
5.7 ASCOT implementation of TCV heating-NB grid geometry. . . 85
5.8 Histogram of the beam trajectory in the two different codes. Different beamlet divergences have been chosen for ASCOT: 22 mrad (red), 8 mrad (blue) and 36 mrad(green) 86
5.9 Sections of the beam trajectory in the two different codes. . . . 87
5.10 3D trajectory of the beam. 87
5.11 Comparison in power balance scalars between ASCOT and NUBEAM. Light green is the absorbed power, yellow is the shine-through, blue is the orbit losses, red is the charge-exchange. 88
5.12 Comparison in terms of power to plasma and driven current for ASCOT (black) and NUBEAM (red) 89
5.13 Particle energy distribution 89

5.14 Performance of AT scenarios in TCV, under the MST program. The higher the additional power, the better performance are obtained (lower V_{LOOP} and higher β_N) 90
5.15 AT plasma performance as function of the additional power. . 90
5.16 Baratrons measurements faults with additional power in TCV. 91
5.17 Computation of CD contribution to ohmic current. 92
5.18 Experimental results for shot 58 823 93
5.19 Input auxiliary power and shape for shot 58823 94
5.20 Volume-integrated temperature and density for NUBEAM analysis. Vertical lines represent the two time instants which will be used later in this work: 0.9 s is without EC heating, while 1.25 s is with maximum EC heating. 94
5.21 Benchmark between the measured thermal energy content (black) and TRANSP simulation (red). Continuous line is total plasma energy, dotted line is the thermal component to the energy, . . 95
5.22 Neutral density edge value. Black line are experimental data while red line is simulated edge neutral density. 96
5.23 NB power balance. Left figure are the absolute values, right figure shows the relative values. 97
5.24 Power to ions (red) and electrons (black). Top: absolute values; bottom:relative values. Cyan line is the theoretical value for ions deposition 98
5.25 Radial profiles of power deposition and fast ion fraction for shot 58 823 at the different time-slices. 98
5.26 Neutral beam current drive for shot 58823. Top-left: shielded and unshielded current; top-right: shielding factor; bottom-left: NBCD efficiency; bottom-right: NBCD profiles 99
5.27 Fast ion energy and pitch angle distributions as function of energy (a) and pitch (b). In (b) the difference between the two functions (no EC-max EC) is shown in red. 99
5.28 Maximum losses to the wall. 100
5.29 q-profile without EC (black) and with EC (red) 101
5.30 First orbit losses with and without EC. Blue area indicates where particles are born. 102
5.31 Total orbit losses with and without EC. Blue area indicates where particles are born. 102
5.32 ρ born position with and without EC. 103
5.33 Major radius born position for first orbit losses and total losses with and without EC power. 103

List of Tables

1.1 Fuel quantity to produce the same amount of power 3

3.1 Density for reference shots. $\langle n_e \rangle$ is the line-averaged density. The last column list the power required for L-H transition, computed with scaling in [39]. 36

4.1 Parameters of JT-60SA tokamak 43
4.2 Parameters of JT-60SA neutral beams 45
4.3 Parameters of JT-60SA reference scenarios 51
4.4 Integrated quantities for Full-I_p scenario, low density 57
4.5 Integrated quantities for Full-I_p scenario, high density 59
4.6 Integrated quantities for AT hybrid scenario 64
4.7 Integrated quantities for AT fully non-inductive scenario . . . 67
4.8 Integrated NBI deposited quantities 73

5.1 Parameters of TCV tokamak 79

To the beloved memory of my grandmother Gelmina
To the beloved memory of my grandfather Bruno
To my family

The man in black fled across the desert, and the gunslinger followed.
S. King

Chapter 1

Controlled thermonuclear fusion and magnetic confinement

1.1 The human need for energy

Physicists usually study a problem considering its energy and how it changes. The human society can be studied as well investigating the energy consumption, as the United Nation Organization (UNO) has been systematically doing. Some interesting results can be obtained: the consumption of energy in the last decades has been constantly increasing (Figure 1.1) [1]; in order to achieve a Human Development Index (HDI) high enough to be considered a *highly developed country*, a certain amount of energy per capita seems to be required, as figure 1.2 shows [2].

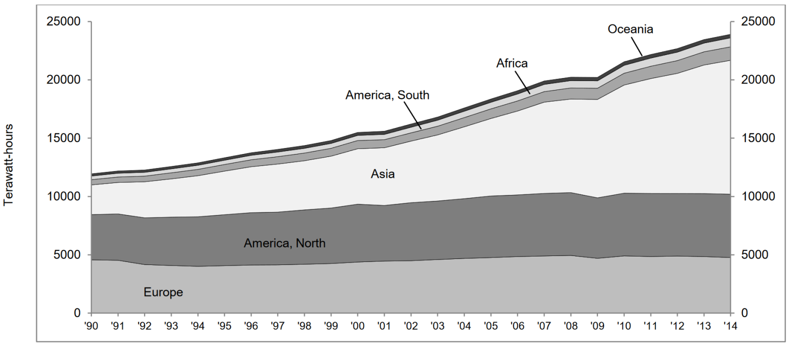

FIGURE 1.1: Energy consumption in the last decades. Image from [1].

These two results are sufficient to conclude that the energy consumption in the future probably won't decrease. The constantly increasing Earth population will cause the energy demand to increase, and countries will use more energy in order to achieve better human conditions.

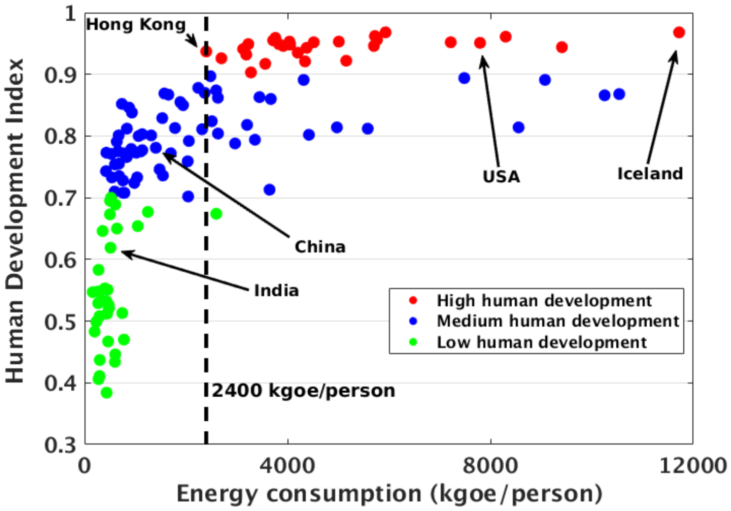

FIGURE 1.2: Human Development Index against energy consumption pro capita (in kg of oil equivalent/person). Data from [2].

1.2 Energy production

In order to satisfy the electrical energy needs, a mix of primary energy sources is used: fossile combustible (coal, oil, natural gas), nuclear fission, hydroenergy, renewable energies (solar power plants, eolic, geothermal, etc.). As figure 1.3 shows, energy production is highly dominated by combustible fuels, i.e. fossile fuels. Burning fossile fuels had a great contribution in releasing high amount of greenhouse gases in the atmosphere (estimated around 75% of the overall production by human activity). The presence of greenhouse gases induces a strong modification in the climate change pattern of the last thousands of years. In particular, in the last century an unexpected increase in atmospheric temperature has been seen, causing melting of arctic ice, shifting of temperature regimes, acidification of the oceans. The main international climate agreement [3] now foresees to stop the temperature increase to 2 °C with respect to the pre-industrial era and this can be done by reducing the greenhouse gases.

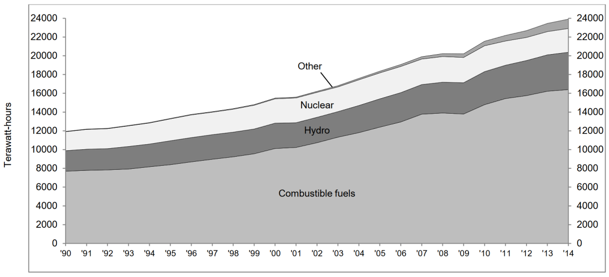

FIGURE 1.3: Mix of energy sources in the last decades

New policies in energy consumption and energy production are under development by the single countries, but all this will hardly be sufficient if keeping the same energy sources mix that we are using now.

Converting all the energy production to CO_2-free technologies would be not feasible due to technological, economical and *social* limits (i.e. the social approval of a certain type of technology must also be taken into account).

1.3 Nuclear fusion

A clean and safe source of energy has to be found. A solution can be nuclear fusion, the opposite process of nuclear fission. While merging two light nuclei, an exothermic reaction is produced if the mass of the products is less than the mass of the reagents.

Nuclear fusion must face with Coulomb force, since the nuclei are positively charged ions. A classical model for nuclear fusion isn't possible, but if we consider the quantum nature of the nuclei, nuclear fusion is possible thanks to the tunnel effect: there is a non-zero probability that the Coulomb repulsive force is overcome in the collision.

The fusion reaction with the most favorable cross-section (in the temperatures regimes considered for this thesis) is the one between deuterium (^{2}H or D) and tritium (^{3}H or T).

$$\mathrm{D} + \mathrm{T} \rightarrow {}^4\mathrm{He}(3.5\,\mathrm{MeV}) + \mathrm{n}(14.1\,\mathrm{MeV}) \tag{1.1}$$

The cross-section of this reaction reaches the value of $\sigma_{DT} \sim 5 \times 10^{24}\,\mathrm{cm}^2$ at E $\sim$100 keV. It is two orders of magnitude lower than U^{235} fission reaction cross-section using a thermal neutron.

Furthermore, power generation from nuclear fusion reactions is relevant because of the its power density (per mass) compared with other power generation fuels power density[4]:

fossil	fission	fusion
106 tonne oil	0.8 tonne uranium	0.14 tonne DT

TABLE 1.1: Fuel quantity to produce the same amount of power

So there is much less need for fuel to produce the same amount of energy.

The reactants of the nuclear reaction are safe and clean as well, in fact D can be filtered from the sea water and T can be produced with the following reactions inside the reactor:

$$^6\mathrm{Li} + \mathrm{n(slow)} \rightarrow {}^4\mathrm{He} + \mathrm{T} + 4.8\,\mathrm{MeV} \tag{1.2a}$$

$$^7\mathrm{Li} + \mathrm{n(fast)} \rightarrow {}^4\mathrm{He} + \mathrm{T} + \mathrm{n} - 2.5\,\mathrm{MeV} \tag{1.2b}$$

T is a radioactive element with a half-life of $\sim$12 years and it is dangerous for human body only if ingested. In the concept of a nuclear fusion power plant based on magnetic confinement, the T should not exit the reactor, so the decayment can take place inside the reactor itself.

Nuclear fusion is the energy of the future: it will be safe (due to the low power density of the reactor, i.e. there are no risks of explosions), clean (no or reduced radioactive waste) as no power source has ever been.

1.4 Magnetic confinement

Shooting a D beam against a T target won't have a remarkable energy-gain, because at that energy the elastic scattering cross-section is much higher than the nuclear reaction cross-section.

The particles should be confined at high temperatures for long enough time, to increase the chances of nuclear reaction between two nuclei. At the temperatures needed, the matter is in the state of plasma, i.e. a gas of ionised particles globally neutral. At fusion-relevant temperatures, plasmas are harmful for materials, thus it must be kept away from the walls of the device.

There are two ways studied nowadays to produce and confine such kind of plasmas:

- *magnetic confinement fusion*: the particles are confined using magnetic fields. In this case the reaction can be run for a long time (at least hours, but even steady-state devices are designed);
- *inertial confinement fusion*: high-power lasers are shot onto a DT pellet, making it implode due to the fast evaporation of its outer layer (compression by radiation). The density in this case is so high that nuclei collide and fuse. This kind of fusion production is intrinsically pulsed (with a confinement time far lower than 1 s).

Magnetic confinement fusion is the topic of this work.

The first magnetic confinement configurations studied were the so-called magnetic bottles [5], linear devices where the charged particles bounce between the zones where the magnetic field is stronger, i.e. at the ends of the devices.

Unfortunately such kind of magnetic fields leads to high losses at the bouncing region, thus toroidal devices have been taken into consideration. In toroidal devices the toroidal magnetic field alone won't provide a sufficient particle confinement time due to drifts (this topic is treated more in detail in section 2.3.2) thus a poloidal magnetic field is needed as well. There are mainly two ways of producing such twist of the magnetic field lines (Figure 1.4):

- *stellarator* devices (figure 1.4b) a set of coils produces the helical magnetic field;
- *tokamak* devices (figure 1.4a) the coils aim to produce a toroidal magnetic field, while the poloidal component is generated inducing a toroidal current in the plasma, using it as the secondary winding of a transformer (the primary winding is the so-called central solenoid).
- *Reversed-Field Pinch* devices are similar to a tokamak,but the toroidal and poloidal components of the magnetic fields are closer in values and the toroidal magnetic field at the edge has the opposite sign with respect to the core. The majority of the magnetic field to confine the plasma is generated by the plasma itself, instead of using a strong external field.

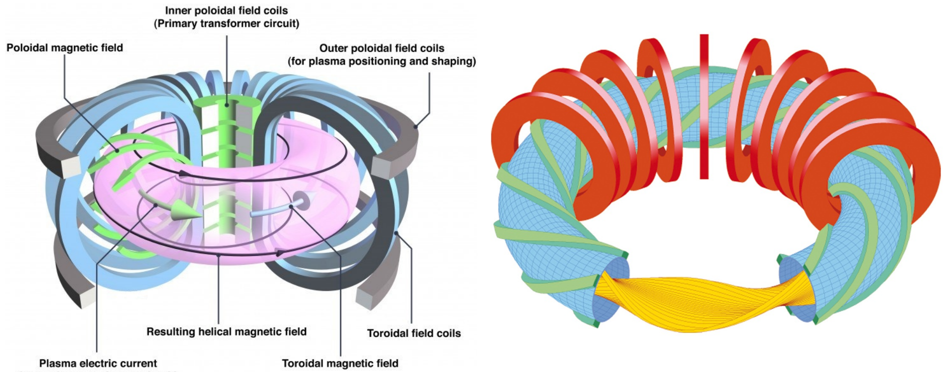
Inner poloidal field coils
(Primary transformer circuit)
Poloidal magnetic field
Outer poloidal field coils
(for plasma positioning and shaping)
Resulting helical magnetic field
Toroidal field coils
Plasma electric current
(secondary transformer circuit)
Toroidal magnetic field

(A) Design of a tokamak machine. The magnetic field given by the toroidal coils and the plasma current results to be helical.

(B) The helical magnetic field is given by the simultaneous action of the two set of coils: toroidal field coils (red) and poloidal (green). Yellow surface is the plasma surface.

FIGURE 1.4: Tokamak and stellarator devices.

This work focuses on the so-called *tokamak*[1], where the toroidal magnetic field is much larger than the poloidal magnetic field.

Stellarators don't need a current to be induced, making the plasma more stable. On the other hand, just to cite one of the main engineering problems, making a helical field using only coils is not an easy task and requires an accurate design of the system and the coil position has a really low tolerance in positioning.

On the other hand, tokamaks are easier to build but inducing a current in the plasma can be the source of instabilities and tokamak plasmas require a higher degree of controllability, compared to stellarator. Tokamak plasmas are better known than stellarator plasmas, and have shown better performances until now.

Triple product

The figure of merit in magnetic confined nuclear fusion is the so-called *triple product* among the quantities n (the plasma density, expressed in m^{-3}), T (its temperature, expressed in eV)[2], τ (the energy confinement time, expressed in s). In order to obtain ignition (i.e. the point at which a nuclear fusion reaction becomes self-sustaining), this product must be greater than $5 \times 10^{21}\,\mathrm{m}^{-3}$keVs, according to the Lawson criteria [6]. The machine which got closest to this value up to now is JET, with $n\mathrm{T}\tau \sim 10^{21}\,\mathrm{m}^{-3}$keVs. Up to years 2000, as figure 1.5 shows, the progress in tokamak plasma performance were increasing with a rate close to the Moore's law for number of transistor in a chip, which doubles every 2 years.

The next step in improving the triple product value should be accomplished by the experiment ITER [7]. A sketch of the ITER tokamak design is shown in figure 1.6. It is the result of an international collaboration between EU, USA, Russia, Japan, India, China, South Korea. It will be the biggest tokamak ever built (major radius: R_0 =6.2 m, minor radius a =2 m). The main

---

[1] russian acronym for *toroidal chamber with axial magnetic field*

[2] $1\,\mathrm{eV}=1.602\,18 \times 10^{-19}\,\mathrm{J}$

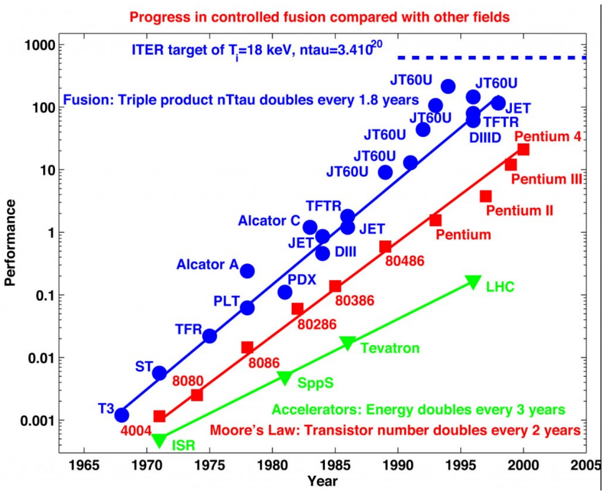

FIGURE 1.5: Tokamak plasma performance in the last years, compared with other fields. Figure from [7].

objectives of ITER are to solve some plasma physics/performance issues, e.g. disruption avoidance, steady state operation, high power generation from fusion (the power coming from nuclear reactions should be 10 times the power coupled to the plasma), . . . and study some of the enabling technology issues, such as the operation of a superconducting machine and the inventory and control of T. In December, 2017 a significant milestone has been set: 50 % of the "total construction work scope towards First Plasma" is completed.

1.5 Content and structure of this work

Nuclear fusion by magnetic confinement relies on neutral beam injection systems in order to become an energy source. Numerical codes capability to correctly investigate the power balance and current driven by neutral beam is well assessed, but different codes make different assumption for resolving the physics equation involved.

In this work, neutral beam capability is studied with different codes (METIS, TRANSP and ASCOT) in three different devices (RFX-mod, JT-60 SA and TCV), to enhance both the importance of such kind of heating systems in tokamak physics and explore the difference which can exist within the different numerical models used. In all the cases explored the beam configuration had been implemented in the framework of this thesis, making thus affordable to explore neutral beam injection heating in integrated modelling codes.

Chapter 2 will give an overview of neutral beam physics and energy particle physics, chapter 3 will present the implementation of a neutral beam injection system in RFX-mod device using mainly the most approximated models, chapter 4 will present the implementation and impact on the plasma from neutral beams in JT60 SA using ASCOT code, chapter 5 will show the results for TCV device, where both NUBEAM and ASCOT tools are used, showing the beam power deposition in advanced tokamak scenarios.

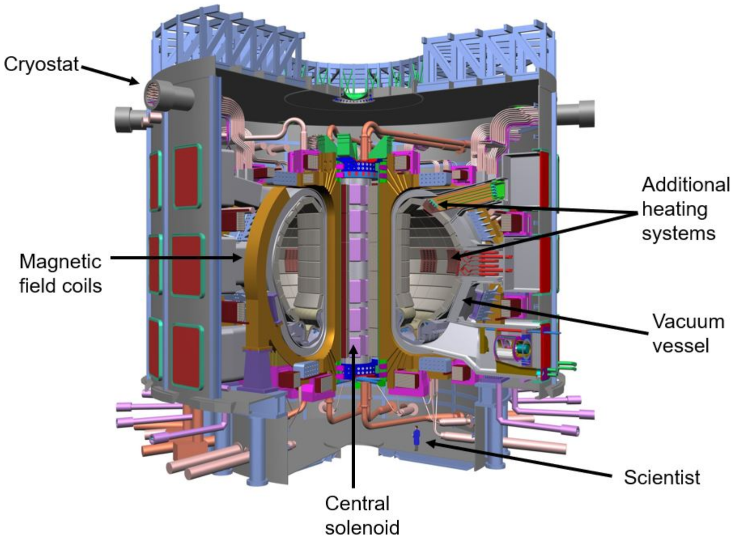
Cryostat
Additional heating systems
Magnetic field coils
Vacuum vessel
Scientist
Central solenoid

FIGURE 1.6: ITER tokamak design. The main components are labelled. Figure from [7].

Chapter 2

Neutral beam injection

2.1 Additional heating systems

The temperature needed by tokamak DT plasma to reach a steady state power balance is at least 15keV [4]. A higher temperature ($\geq$20 keV) is needed for a net energy gain from nuclear fusion. These temperatures can be reached using a set of heating systems, as figure 2.1 shows. In tokamak configuration the first way of heating the plasma is with ohmic heating: $p = \eta j^2$, where p is the power density, η is the resistivity and j the current density. The power coupled in this way to the plasma has an upper limit (3 keV) because the plasma resistivity decreases with the temperature $\eta \sim T^{-3/2}$ [9]. For stellarator configuration this heating source is useless since there is no plasma current.

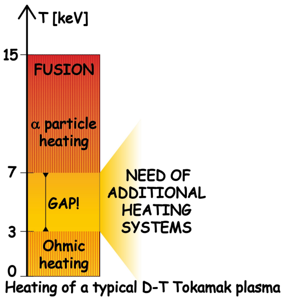
T [keV]
15
FUSION
α particle heating
7
GAP!
NEED OF ADDITIONAL HEATING SYSTEMS
3
Ohmic heating
0
Heating of a typical D-T Tokamak plasma

FIGURE 2.1: Heating of a tokamak. Figure from [8]

Starting from 7 keV on, the heating power of the plasma is given by the slowing down of the 3.5 MeV α particles produced in fusion reactions.

The main issue is to fill the gap between ~3 keV and ~7 keV. This is done using additional heating systems which can be divided in two types: wave injection heating and neutral beam injection (NBI) heating.

The former aims to heat the plasma by injecting electromagnetic waves that couple with the charged particles, thus giving energy to them and heating them. There are three kinds of waves mainly used, whose main difference is the injection frequency:

- electron cyclotron (EC) waves: these waves couple to the plasma electrons, thanks to their gyration motion around the magnetic field lines.

The wave frequency ($\omega = \frac{qB}{m}$ ~100 GHz) must be adapted to the magnetic field in the plasma: the magnetic field depends on $1/R$, being R the major radius, so the resonant layer to be heated lies in a narrow area;

- Ion cyclotron (IC) waves: they work with the same principle as EC waves, coupling mostly with ions. In this case the frequency is around some tens of MHz;
- Lower hybrid (LH) waves: these waves don't couple with the particles gyro-motion. In this case the phase velocity of the wave is slightly bigger than the average thermal speed of the electrons, so that the particles see an electric field since they move almost at the same speed of the wave. The particles faster than the wave are slowed down, giving energy to the wave. The particles slower than the wave gain energy, accelerating and then giving this energy to the plasma through collisions.

Neutral beam injection (NBI) heating works by injecting into the plasma atoms much faster than the thermal average velocity of the bulk particles. The injected atoms get ionised and confined in the magnetic field, heating the plasma by collisional processes. Different injection trajectories (see figure 2.2) can be chosen, depending on the needs for the NBI heating systems: e.g. if current drive is desired, the beam is installed tangentially co-current; if, otherwise, central heating is required, it is installed nearly-perpendicular.

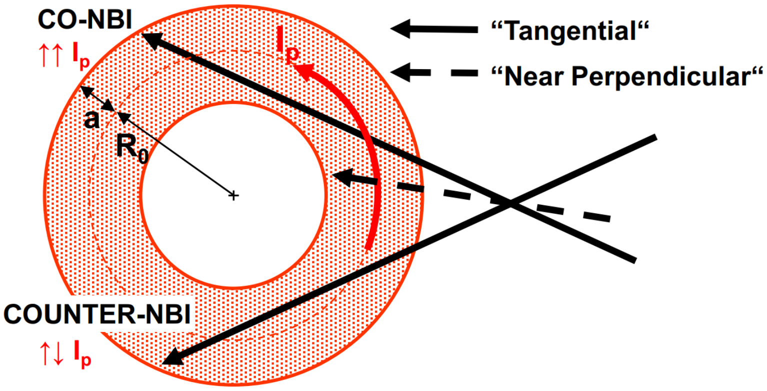

FIGURE 2.2: Neutral beam injection geometries.

NBI heating has been used starting from the 1970s and its effect has been immediately seen as beneficial: $T_i > 4\,\text{keV}$ was a record impossible to reach without it [10].

In TFTR and JET the interaction between the fast ions of the beam and the bulk ions resulted in a high rate of fusion reactions during the DT campaigns. These beam-target reactions were the dominant fusion reactions in the experiments [11], [12], [13], [14].

In smaller devices (e.g. TCV), where the confinement time is low and there is poor coupling between ions and electrons, NBI allows to reach high ion temperature values.

NBI is a fundamental tool to achieve nuclear fusion with magnetic confinement, both for its heating non-inductive current driving capability. Interaction between fast particles injected by neutral beams and tokamak plasma is the topic of this thesis.

2.2 Generation of fast neutrals

Neutral beams (NBs) are one of the most complex tools used in tokamak science. In this section, a brief description of the system generating the fast ions is given. A sketch of the system is given in figure 2.3.

Fast atoms are created by accelerating ions through a set of electrostatic lenses and then neutralised. This last step is necessary in order for the fast particles to penetrate the magnetic fields in the tokamak plasma up to the core, where it is usually desirable to deposit most of the power.

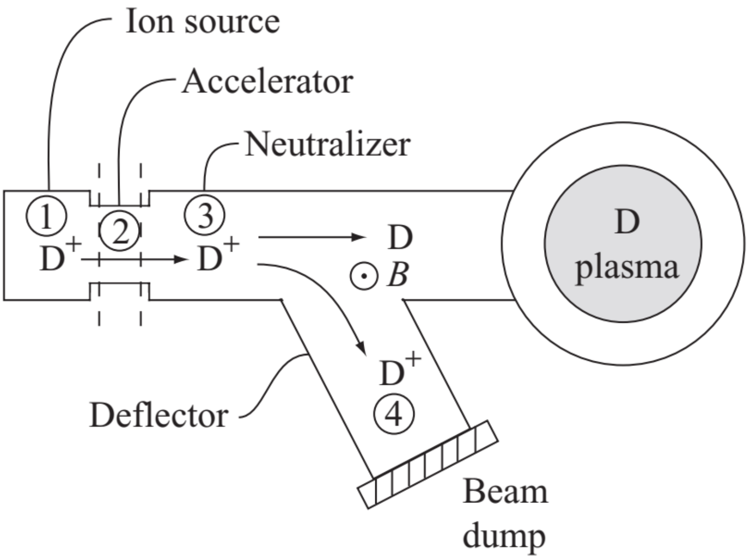

FIGURE 2.3: Graphical sketch of a neutral beam. Image taken from [4].

2.2.1 Source

The ion source must be designed based on the type of ions to be accelerated: positive or negative. Usually an ionised gas is generated and the desired ions are extracted. One of the most common ways to generate the plasma where the ions are created is to use a filament source, i.e. a tungsten wire is heated up to the condition where electrons are ejected from the filament. The potential difference between the wire and the chamber makes the electrons to accelerate and ionise the gas, giving thus the plasma. A modern approach to produce ions is given by radio frequency (RF) sources. In this case a set of RF waves are coupled to the gas and the plasma is created accelerating the free electrons in the gas.

In the case of positive sources, not only single-charged ions are produced, but also single-charged molecules (formed by chemical bonds between two or three atoms in the plasma). During acceleration, these molecules reach fraction of the ions velocity, depending on their mass.

In the case of negative ion sources, some wall conditioning must be used to increase the rate of negative ion production. Usually the species accelerated are H, D, but also T or He can be used.

2.2.2 Accelerator

In the accelerator a set of electrostatic grids creates the electrostatic field to carry the fast ions to the desired energy. The beam optics is fully determined in this area. Usually the grid is subdivided in many holes and the particles passing through each hole form the so-called *beamlet*. These holes are shaped to optimise the direction of the beamlet and its divergence (the spread of the beamlet along its direction).

perveance A limit in the extracted current and the acceleration energy arises in this part. This limit is given by the shape of the accelerator grids and is mathematically expressed using the so-called perveance p:

$$I = p \cdot U_{ACC}^{3/2} \quad \Rightarrow \quad \text{power} = I \cdot U_{ACC} = p \cdot U_{ACC}^{5/2} \tag{2.1}$$

This means that when changing the acceleration voltage (i.e. the energy), the power must be modified accordingly to equation 2.1.

2.2.3 Neutraliser & residual ion dump

The accelerated charged particles exit the electric field zone and enter in the neutraliser, where charge-exchange reactions neutralise the ions. This component of the beam puts a hard limit in the type of ions to be accelerated: in fact the neutralisation efficiency is really different for positive and negative ions as figure 2.4 shows. In the first case, the neutralisation efficiency is maximum at lower energies and drops to values lower than 20 % at energies $\gtrsim$200 keV. For negative ions, the efficiency can reach high values ($>$ 60%) at 1 MeV.

The residual and unwanted ions at the end of the neutraliser are deflected to a designed dump, using electric or magnetic fields.

2.2.4 Beam duct & beam port

The neutraliser cannot be too close to the tokamak coils and a duct is needed. If the beam optics is not properly designed, some losses of the beam power can occur heating the duct wall and, outgassing, damage the vacuum of the system. Even more, the walls can be so stressed to fuse.

A neutral beam is an invasive method for additional heating: a hole in the vacuum vessel connecting it to a different vacuum is something to care about when designing the machine, and in particular the port to the tokamak.

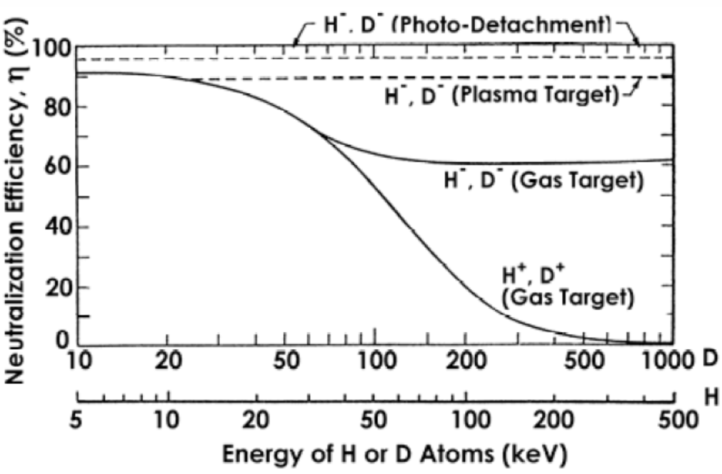

FIGURE 2.4: Neutralisation efficiency for positive and negative H/D ions with respect to energy [15]

2.3 Energetic particles ionisation and orbits in tokamak

In this section, the physical processes affecting beam fast neutrals are presented.

The first physical process particles undergo is ionisation. After ionisation, the particles are confined in the magnetic field and, by Coulomb collisions, give energy to the plasma.

2.3.1 Beam ionisation

The three processes responsible for ionisation are listed in equations 2.2 and apply also for D and T.

Ionisation by electrons (ie) $H_{fast}+e \rightarrow H^{+}_{fast} + e + e$ (2.2a)

Ionisation by ions (ii) $H_{fast}+H^{+}_{slow} \rightarrow H^{+}_{fast} + e + H^{+}_{slow}$ (2.2b)

Charge-exchange (cx) $H_{fast}+H^{+}_{slow} \rightarrow H^{+}_{fast} + H_{slow}$ (2.2c)

The cross-section of the main ionisation processes is plotted in figure 2.5.

The trend of the total cross-section is $\sigma \sim 1/E$, where E is the relative energy between the fast atoms injected and the target.

The charge-exchange cross-section reaction is negligible for $E/A \gtrsim 10^2$ keV/AMU. In future machines, e.g. ITER, the energy of the fast neutrals injected is much higher than this value, so charge-exchange reactions will be negligible.

The slow neutral particles resulting by CX between fast neutrals and slow ions are usually called *halo*. These particles travel ballistically and do charge-exchange reactions with the background ions, resulting in a source of neutrals in the plasma core.

Ionisation by electrons is relevant at lower electron temperature ($\sim$ 1 keV), but decays with energy.

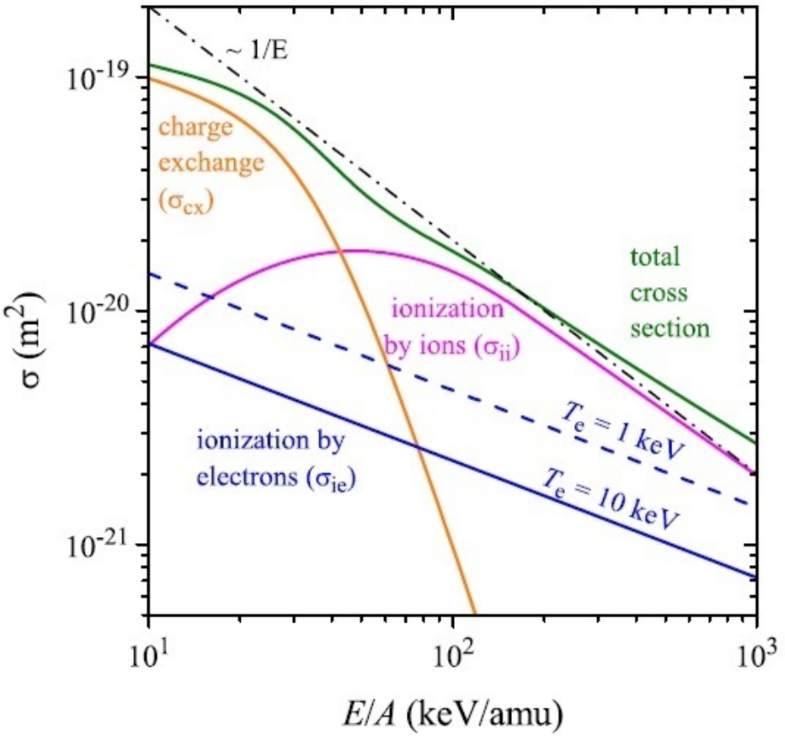

FIGURE 2.5: Ionisation cross-sections for the main reactions between fast ions and plasma. Image from [16].

Ionisation by ions is relevant also at energies up to the MeV, thus this is the most relevant reaction also in the case of high-injection energy. The dependence with temperature is hidden because usually bulk ions are considered at rest due to their inertia.

MSI These three reactions are not sufficient for a full description of the ionisation of the beam. In fact, also the multi-step ionisation (MSI) must be considered: in these processes an ion is excited at first and then ionised. This effect can increase the cross-section by a factor of two when using high beam energies (>1 MeV u^{-1}). A full treatment of the MSI can be found in [17].

The beam attenuation equation can be described with equation 2.3:

$$\frac{\mathrm{dI}}{\mathrm{ds}} = -n\sigma \mathrm{I}_0 \qquad \Rightarrow \qquad \mathrm{I(s)} = \mathrm{I}_0 \exp\left(-n\sigma \mathrm{s}\right) \tag{2.3}$$

where s is the coordinate along the beam direction, I the beam intensity, I_0 the initial beam intensity, n the plasma density.

σ is the cross-section and must be computed by averaging over the distribution function f of the target particles in the following way

$$\sigma = \sum_{l=\text{ie, ii, ix}} \frac{\langle \sigma_l v \rangle}{v_{\text{beam}}} \qquad \text{where} \qquad \langle \sigma_l v \rangle = \frac{\int \sigma_l(u) u f(u) du}{\int f(u) du} \tag{2.4}$$

where u is the relative velocity $\|\mathbf{v}_{\text{beam}} - \mathbf{v}_{\text{target}}\|$

The quantity

$$\lambda = \frac{1}{n\sigma} \tag{2.5}$$

is usually called *mean free path*, and in this case represents the distance where the beam intensity is 1/e its initial value. This distance must be carefully addressed in order to avoid high beam losses through *shine-through* , i.e. the fraction of the beam not ionised in the plasma. A too high fraction of shine-through results in a high power flux to the wall, that could cause its melting. In some tokamaks (e.g. TCV) this issue is so important that the beam stops if the plasma density is too low.

shine-through

The fast ion birth profile (FIBP) represents the amount of particles born in a certain volume during a certain time. It is particularly interesting because the position where the fast ions are born characterises their orbit inside the plasma.

2.3.2 Orbit drifts

The newly born fast ions get confined in the plasma magnetic field and follow the orbit defined by the Lorentz force (with m the mass, q the electric charge and **B** the magnetic field)

$$m\frac{d\mathbf{v}}{dt} = q\mathbf{v} \times \mathbf{B} \tag{2.6}$$

and this force makes the ion to gyrate around the magnetic field line with the following radius and frequency:

$$\rho_L = \frac{mv_\perp}{q|B|} \qquad \omega_L = \frac{q|B|}{m} \tag{2.7}$$

the subscript $\perp$ refers to the magnetic field direction.

This motion is split for convenience when described: in fact the axis of the helix is the trajectory of the guiding-centre of the orbit, whose dynamics is mostly influenced by the parallel component of the velocity (this is not true in the case of e.g. trapped particles). The gyro-motion given by Lorentz force must then be added, and this last one is determined by the perpendicular component of the velocity.

The orbit is modified if there are some forces that add up to the Lorentz force.

E field drift

With an electric field **E**, equation 2.6 changes as follows:

$$m\frac{d\mathbf{v}}{dt} = q(\mathbf{E} + \mathbf{v} \times \mathbf{B}) \tag{2.8}$$

In the plane parallel to the magnetic field, the particle is accelerated by the electric field. In the perpendicular direction, we have

$$m\frac{d\mathbf{v}_\perp}{dt} = q(\mathbf{E}_\perp + \mathbf{v}_\perp \times \mathbf{B}) \tag{2.9}$$

In steady state conditions (i.e. if the time derivative is 0 or averaging over a gyration period), the following relation applies

$$\mathbf{E}_\perp = -\mathbf{v}_\perp \times \mathbf{B} \tag{2.10}$$

Doing a right cross-product with the vector **B** and using a property of the double cross-product [1] we get

$$\mathbf{v}_\perp = \frac{\mathbf{E}_\perp \times \mathbf{B}}{|B|^2} \tag{2.11}$$

This modifies the helical motion given by equation 2.6 into a cycloid, giving it a velocity component perpendicular to both the electric and magnetic field and independent of the particle charge.

Substituting the electrical force $q\mathbf{E}$ with a generic force **F** the following expression can be obtained:

$$\mathbf{v}_\perp = \frac{\mathbf{F}_\perp \times \mathbf{B}}{q|\mathbf{B}|^2} \tag{2.12}$$

$\nabla\mathbf{B}$ drift

In a tokamak, the external toroidal magnetic field is not constant along the major radius: in fact, following Ampere's law, we can deduce that:

$$B_\phi(R) = B_\phi(R_0)\frac{R_0}{R} \quad \Rightarrow \quad \frac{\nabla B}{B} = -\frac{\mathbf{R}}{R^2} \tag{2.13}$$

This implies that the magnetic field changes over a Larmor orbit. If we assume the magnetic field changes slightly only perpendicularly the guiding-centre motion (in the xy plane, let's say in the y-direction) $\left(\rho_L \frac{1}{B}\frac{\partial B}{\partial y} \ll 1\right)$, the expression for the Lorentz force becomes

$$F_y(y) = -qv_x(B_0 - \frac{\partial B}{\partial y}y) \tag{2.14}$$

By averaging over a gyration period an expression for the external force acting on the particle can be found. We can then calculate the drift velocity using equation 2.12

$$\mathbf{F} = -\frac{1}{2}q\omega_c\rho_l^2\nabla B \quad \Rightarrow \quad \mathbf{v}_{\nabla B} = \frac{1}{2}v_\perp\rho_L\frac{\mathbf{B}\times\nabla B}{B^2} = \frac{1}{2}\frac{m}{q}v_\perp^2\frac{\mathbf{R}\times\mathbf{B}}{R^2B^2} \tag{2.15}$$

As can be noted, this drift depends as well on the charge of the particle.

---

[1] $a \times (b \times c) = b(a \cdot c) - c(a \cdot b)$

Curvature drift

The tokamak has the shape of a torus, thus a centripetal force is acting on the particles.

$$\mathbf{F_C} = m\frac{v_\parallel^2}{R^2}\frac{\mathbf{R}}{R} \quad \Rightarrow \quad \mathbf{v}_{\text{curv}} = \frac{mv_\parallel^2}{qR^2}\frac{\mathbf{R}\times\mathbf{B}}{B^2} \tag{2.16}$$

with R the major radius of the torus. This force adds a drift to the ∇B drift and the resulting drift velocity is

$$\mathbf{v}_D = \mathbf{v}_{\text{curv}} + \mathbf{v}_{\nabla B} = \frac{m}{q}\left(v_\parallel^2 + \frac{1}{2}v_\perp^2\right)\frac{\mathbf{R}\times\mathbf{B}}{R^2B^2} \tag{2.17}$$

As the formula suggests, this drift velocity is opposite for ions and electrons, because of its dependence with the electrical charge.

If the magnetic field is only toroidal, this leads to charge separation and an electric field arises. Another drift caused by this electric field then appears, and this drift is radial (i.e. perpendicular to the toroidal magnetic field): the particles get lost to the chamber wall, leading to huge losses. Adding a poloidal component of the magnetic field, this effect sums out and the losses are reduced.

2.3.3 Trapped and passing orbits

The dynamics of a charged particle in a tokamak is dominated by the Lorentz force and the drifts aforementioned, but one term is missing. The magnetic field can vary also along the trajectory of the guiding center.

Let's consider a cylindrical system (r, θ, z), with an axial-symmetric magnetic field, directed along the z-direction and varying with z. Since the field is divergence-free, we can link the radial and axial components of the field by assuming $\partial B_z/\partial z$ does not vary with r:

$$\nabla\cdot\mathbf{B} = 0 \quad \Rightarrow \quad B_r = -\frac{1}{2}r\left[\frac{\partial B_z}{\partial z}\right]_0 \tag{2.18}$$

Having both the components of the magnetic field, it is straightforward computing the z-component of the Lorentz force:

$$F_z = -qv_\theta B_r = \frac{qrv_\theta}{2}\left[\frac{\partial B_z}{\partial z}\right]_0 \tag{2.19}$$

Averaging over the gyration motion, putting $r = \rho_L$ and $v_\theta = \mp v_\perp$ (due to the different charges) we obtain

$$\mathbf{F}_z = \mp\frac{q\rho_L v_\perp}{2}\frac{\partial B_z}{\partial z} = \mp\frac{qv_\perp}{2}\frac{mv_\perp}{qB}\frac{\partial B_z}{\partial z} = -\frac{mv_\perp^2}{2B}\frac{\partial B_z}{\partial z} = -\mu\frac{\partial B_z}{\partial z} \tag{2.20}$$

Being μ the **adiabatic invariant** (or magnetic momentum):

$$\mu = \frac{mv_\perp^2}{2B} \tag{2.21}$$

In a 3D configuration, being s the line element along **B**:

$$\mathbf{F}_{\parallel} = -\mu \frac{d\mathbf{B}}{ds} = -\mu \nabla_{\parallel} B \tag{2.22}$$

There are some conditions where this force can be so strong that the particle bounces back along its trajectory. This effect is called magnetic mirror and this is the principle the magnetic bottle is based on. The particle gets reflected ($v_{\parallel} = 0$) when the magnetic field reaches the value

$$B_{\max} = B \cdot \left[\left(\frac{v_{\parallel}}{v_{\perp}} \right)^2 + 1 \right] \tag{2.23}$$

In a tokamak, the condition where the magnetic mirror appears can be found thanks to the dependency of the toroidal magnetic field with the major radius. If we consider a particle born at position $R_1 = R_0 + r$, this particle will reach the position $R_2 = R_0 - r$ (where $B_2 = B_0 \frac{R_0}{R_0 - r}$) only if $B_2 > B_{\max}$. This consideration brings the following conditions for trapped particles:

$$\frac{v_{\parallel}}{v_{\perp}} > \sqrt{\frac{2r}{R_0 - r}} \quad \text{Passing orbits} \quad \frac{\xi}{\sqrt{1-\xi^2}} > \sqrt{\frac{2r}{R_0 - r}} \tag{2.24a}$$

$$\frac{v_{\parallel}}{v_{\perp}} < \sqrt{\frac{2r}{R_0 - r}} \quad \text{Trapped orbits} \quad \frac{\xi}{\sqrt{1-\xi^2}} < \sqrt{\frac{2r}{R_0 - r}} \tag{2.24b}$$

Being ξ the *pitch*, i.e. the projection of the particle velocity over the magnetic field direction ($v_{\parallel}$/v). Applying this condition to injection geometries, if the beam is injected near-perpendicularly ($\xi \sim 0$) the boundary radius (i.e. r such that 2.24 is an equality) will move closer to the plasma axis ($r = 0$), otherwise for tangential injection the boundary radius will be closer to the edge.

In figure 2.6 a sketch of the trajectory of trapping and passed particles is shown. Integrating equation 2.22, it can be seen that the drifted orbits of the particles have the shape of a banana (on the poloidal plane), lying around a magnetic surface with a half-width (usually called banana width) equals to

$$\Delta r = \frac{v_{\parallel,0}}{\omega_{c\theta}} = \frac{m v_{\parallel,0}}{q B_{\theta}} \tag{2.25}$$

with $v_{\parallel,0}$ the initial parallel velocity and $\omega_{c\theta}$ the Larmor frequency for a particle with velocity $v_{\parallel,0}$ calculated using only the poloidal magnetic field B_{θ}.

All these considerations work on a 2D projection (figure 2.6a), because when we consider the 3D projection of the particle, it moves also along ϕ, as shown in figure 2.6.

The orange-shaped orbits (green in the figure) are typical for passing particles.

First orbit losses

The importance of trapped and passing particles for neutral beam injection is strictly related to injection geometry (see figure 2.7). Particles with

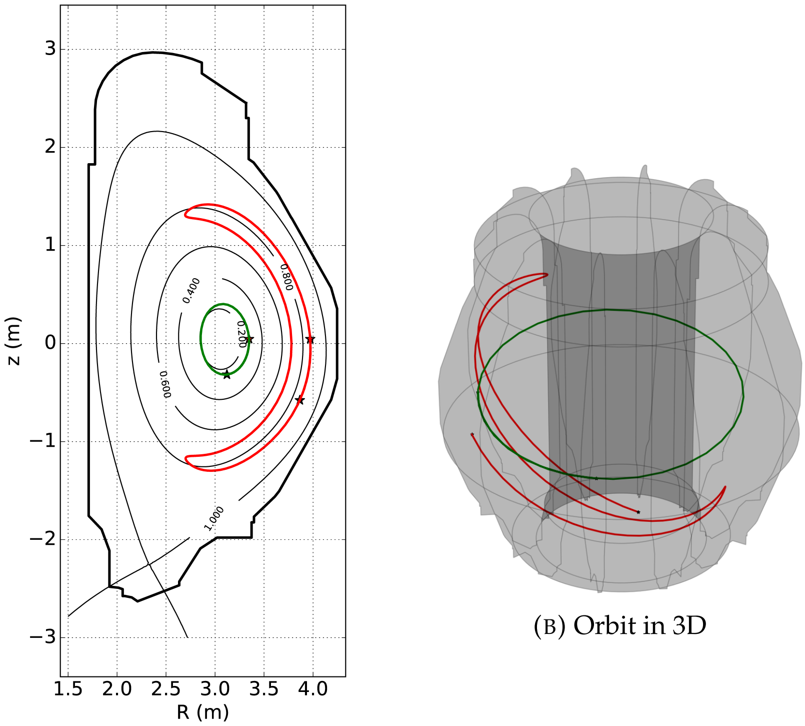

(A) Projection on poloidal and toroidal field.

(B) Orbit in 3D

FIGURE 2.6: Trapped (red) and passing (green) orbits.

born in the inner leg of the banana will follow large orbits which might collide with the wall in a short time, increasing the so-called *first orbit losses*. In fact, if we integrate the particle orbit [18] in order to link the minor radius of the particle with its parallel velocity, we obtain

$$r - r_0 = -\frac{m}{qB_p} v_{\parallel} \tag{2.26}$$

being r_0 the borning minor radius of the particle. All these solutions have been taken by considering the direction of the plasma current (and the poloidal magnetic field) as "positive". If the parallel velocity is negative, r will increase. If this happens at the beginning of the orbit (counter-current injection), the particle collides with the wall as the green orbits in figure 2.7b shows.

2.4 Energetic particles slowing down

2.4.1 Coulomb collisions

The forces slowing down particles in a tokamak plasma are due to the electric charges of the species, and this phenomena is addressed as Coulomb collisions. A detailed description of the Coulomb collisions can be found in [4],

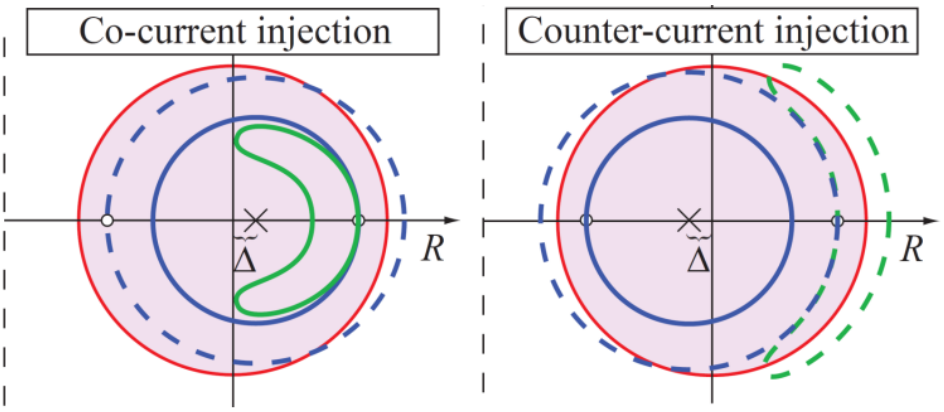

(A) Co-current injection

(B) Counter-current injection

FIGURE 2.7: Orbits of neutral-beam injected particles. The white dots are the born position. Δ is the Shafranov shift. The dotted lines represent orbits colliding with the walls.

[18].

In this section, we will refer only to collisions between energetic particles and bulk plasma particles. One of the main things to take into account is the difference in collisions with ions and electrons, due to the difference in their mass. This can be clearly seen computing the average rate of energy loss and momentum loss given by these collisions. In the following part, the label b will represent a beam ion which collides with a target particle labeled with T.

The collision frequency for energy loss by the beam particle can be computed and it results:

$$\nu^{E_k} = n_T \frac{8\pi}{m_b m_T} \frac{q_b^2 q_T^2}{(4\pi\epsilon_0)^2} \frac{1}{v_b^3} \tag{2.27}$$

while the collision frequency for momentum loss is:

$$\nu^{p} = n_T 4\pi \frac{q_b^2 q_T^2}{(4\pi\epsilon_0)^2} \frac{m_b + m_T}{m_T m_b^2 v_b^3} \ln\Lambda \tag{2.28}$$

being ϵ_0 the vacuum permittivity and $\ln\lambda$ is the Coulomb logarithm. This factor identifies the ratio between small-angle and large-angle collisions effectiveness.

If we compare the two frequencies, we obtain the following result:

$$\frac{\nu^{E_k}}{\nu^{p}} = \frac{2m_b}{m_b + m_T} \quad \Rightarrow \quad \begin{cases} 2, & \text{if } m_b >> m_T \text{ EP on electrons} \\ 1, & \text{if } m_b \sim m_T \text{ EP on ions} \end{cases} \tag{2.29}$$

If the beam particle collides with an electron, the loss of energy will be higher than the loss of momentum, while if it collides with an ion the rate of loss will be the same.

The point is now understanding when the collision happens preferentially with ions or electrons. This issue has already been addressed in [19] and is presented here. Assuming that $v_{th,e} >> v_B >> v_{th,i}$, the average loss of energy E along the beam path (x) of a beam particle by Coulomb collisions can be written in the following way:

$$\frac{dE}{dx} = -\frac{\alpha}{E} - \beta E^{1/2} \tag{2.30}$$

where α and β are two coefficients related respectively to ions and electrons

$$\text{Ions} \qquad \alpha = 1.30 \times 10^{-13} \mathrm{A} \mathrm{Z}^2 \log \Lambda \sum_i \frac{n_i Z_i^2}{A_i} \tag{2.31a}$$

$$\text{Electrons} \qquad \beta = 2.28 \times 10^{-15} \frac{\mathrm{Z}^2}{\mathrm{A}^{1/2}} \frac{n_e \log \Lambda}{(kT_e)^{3/2}} \tag{2.31b}$$

in the above expressions, A and Z are the ones for the beam particles, the index i labels the ion species in the plasma. α contains only values referring to ion species while β has only electron-related quantities. So the two terms in equation 2.30 distinguish the energy deposition to ions and electrons respectively.

Equation 2.30 makes possible to calculate the critical energy, i.e. the energy where the deposition to ions and electrons is equal:

$$\frac{\alpha}{E_c} = \beta E_c^{1/2} \quad \leftrightarrow \quad E_c = \left(\frac{\alpha}{\beta}\right)^{2/3} = 14.8 kT_e \left[\frac{A^{3/2}}{n_e} \sum_i \frac{n_i Z_i^2}{A_i}\right]^{2/3} \tag{2.32}$$

For a pure H plasma, $E_{\text{crit}} \sim 15\mathrm{T}_e$, while for a pure D plasma, $E_{\text{crit}} \sim 20\mathrm{T}_e$. Above the critical energy the collisions happen mostly with the electrons, thus we have a variation on the particle energy, as obtained with relation 2.29. Below the critical energy, the impact on the momentum of the particles is such that its orbit changes.

It is possible furthermore to calculate the slowing-down time of the particles, in this case the time they spend to release all its energy[2]

$$\frac{dE}{dt} = v \times \frac{dE}{dx} = \sqrt{\frac{2E}{m}} \times \frac{dE}{dx} \overset{[E]=\mathrm{eV}}{=} 1.39 \times 10^6 \left(\frac{E}{A}\right)^{1/2} \times \frac{dE}{dx} \tag{2.33}$$

---

[2] This is a limit-case, in fact for modelling purposes the particles are considered thermalised (i.e. no more fast) when their energy is around 2 times the local T_e, depending on the model used (e.g. some codes use $1.5T_e$)

$$\begin{aligned}\tau(\mathrm{s}) &= -\int_0^{E_0} \frac{dE}{dE/dt} = \\ &= 3.13\times 10^{14}\frac{A(kT_e)^{3/2}}{Z^2 n_e \log\Lambda}\int_0^{E_0}\frac{\sqrt{E}}{E_c^{3/2}+E^{3/2}}dE = \\ &= \frac{t_s}{2}\frac{2}{3}\log\left[E_c^{3/2}+E^{3/2}\right]_0^{E_0} \\ &= \frac{t_s}{3}\log\left[1+\left(\frac{E_0}{E_c}\right)^{3/2}\right]\end{aligned} \tag{2.34}$$

with t_s the Spitzer slowing-down time [9]. The slowing-down time up to $2\mathrm{T_e}$ gives difference (with respect to the slowing down time up to 0) around $\sim$ 2%, so limiting to $2\mathrm{T_e}$ is a good approximation for the full slowing-down. These times are around 10 - 100 ms for the devices currently in operation.

Lastly, the amount of power deposited to the ions or to the electrons for a given beam energy can be computed, and an answer to the beginning question of this section can be found. This is important while designing a neutral beam system for a tokamak, since knowing the energy of the beam (and its relation to the critical energy), the energy coupled with ions or electrons can be computed.

$$G_i = \frac{E_i}{E} = \frac{1}{E}\cdot -\int_0^{\tau}\left(\frac{dE}{dt}\right)_i dt = \cdots = \frac{E_c}{E}\int_0^{E/E_c}\frac{dx}{1+x^{3/2}} \tag{2.35a}$$

$$G_e = 1 - G_i \tag{2.35b}$$

The fraction of power delivered to the ions decreases when increasing the E_0/E_c ratio, as figure 2.8 shows. In the majority of the present devices the heating is dominant to ions, while for future devices we will get to higher E_0/E_c values, thus higher electron heating.

2.4.2 Fokker Plank equation

The dynamics of fast particles in a tokamak is ruled by the equation of motion in an EM field and the Coulomb collisions with the plasma itself. The usual approach to this problem is studying the distribution function of the fast particles. A distribution function f($\mathbf{r}$, $\mathbf{v}$) represents the probability density of finding a particle in a given state: in other words, its integral represents the probability of finding a particle in the integration domain. When a collisional process modifies the dynamic of the particles, the evolution of the distribution function is ruled by the Fokker-Planck equation:

$$\frac{\partial f}{\partial t} + \dot{\mathbf{z}}\cdot\frac{\partial f}{\partial \mathbf{z}} = \left(\frac{\partial f}{\partial t}\right)_{coll} \qquad \mathbf{z} = (\mathbf{r},\mathbf{v}) \tag{2.36}$$

In most of the cases the collisional term (right-hand side) is modeled with diffusion and friction, thus this equation becomes a six-dimensional partial

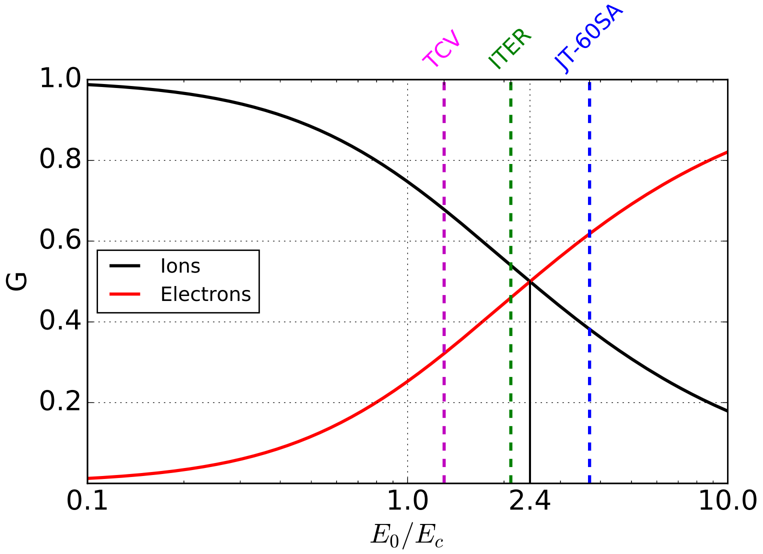

FIGURE 2.8: Fraction of power to the different plasma species. The vertical dotted lines (from left to right) represent the tokamak TCV, ITER and JT-60SA.

differential equation. For this reason, its solution is exact only for some particular cases.

A solution can be made neglecting three physics aspects:

- no energy diffusion: only the slowing-down given by equation 2.33 is considered;
- no trapping effects: the particles are considered only confined in passing orbits;
- no pitch angle scattering: i.e. the velocity vector doesn't change its direction;

and in this way equation 2.36 becomes

$$\frac{\partial f}{\partial t} = \frac{1}{v^2}\frac{\partial}{\partial v}\left(\frac{v^3 + v_c^3}{\tau_s} f\right) + \frac{S_0}{4\pi v_0^2}\delta(v - v_0) \tag{2.37}$$

which has the following solution:

$$f = \frac{S_0 \tau_s}{4\pi}\frac{\Theta(v_0 - v)}{v^3 + v_c^3} \tag{2.38}$$

where v_c is the velocity related to the critical energy (eq. 2.32), τ_s is the slowing-down time (eq. 2.34), S_0 the fast ion source, δ the Dirac delta and Θ the step function (zero for $v > v_0$). More accurate results can be obtained using the average change in velocity and pitch (given by the Fokker-Planck equation) or Monte Carlo collision operators, as will be described in section 2.8.

2.5 Losses of fast ions

During slowing-down, fast ions can be lost mainly due to three processes: orbit losses, radial redistribution due to interaction with plasma instability or waves and charge-exchange.

Orbit losses

The orbit losses are the particles lost due to their orbit, i.e. when they collide with the wall during their motion. This can be due both to trapped banana orbits (explained in section 2.3.3) or to the change in velocity of the particle due to collision, which can put the particle in an unconfined orbit and make it collide with the wall. The particles ionised in the scrape-off layer (SOL) (where the magnetic field lines collide with the wall) are usually lost due to the unconfined orbit (and low collision rate) they are trapped in.

Anomalous diffusion

Some MHD activity (such as sawteeth) or electro-magnetic waves (such as Alfvén Eigenmodes (AEs)) can induce EP radial transport. This happens because the structure of the electro-magnetic field is modified, thus the particle orbits. The former is a kind of instability which appears when the safety factor profile (the number of poloidal turns a magnetic field line accomplish within one toroidal turn) gets below unity. In this cases, reconnection events redistribute the fast ions because of the electromagnetic field which are induced during the reconnection. The latter is a kind of wave which is driven by particles having velocity greater than the so-called "Alfvén speed". This kind of waves interacts with the energetic particles gaining energy from them and modifying their orbits [20].

Charge exchange

The charge-exchange losses are due to collisions between a fast ion and a neutral. In this case the particle is lost because it becomes a neutral after the collision, becoming unconfined in the magnetic field and then colliding with the wall (if not previously re-ionized). This loss channel is strictly related to the presence of neutrals in the plasma. The atomic reaction ruling this process is the following:

$$\mathrm{H}^+_{\mathrm{fast}} + \mathrm{H}_{\mathrm{fast,slow}} \rightarrow \mathrm{H}_{\mathrm{fast}} + \mathrm{H}^+_{\mathrm{fast,slow}} \tag{2.39}$$

The fast ions can collide both with a fast or slow neutral. In a tokamak plasma, there are usually four populations of neutrals:

- neutrals coming from the wall or the valves feeding the plasma, usually lying only in the SOL and being soon ionised;
- neutrals generated in the plasma by recombination or charge-exchange reactions;
- fast neutrals injected using the neutral beams;
- slow neutrals generated by the charge-exchange reactions that ionise the beam neutrals (also called *halo* neutrals).

This issue can be relevant for nowadays tokamak, but for tokamak with higher temperatures the population of neutrals in the plasma will be negligible.

2.6 Current drive

NB injection does not provide only a source of heating but also a current can be driven by the fast ions tangentially injected in the plasma [21] [22].

With a non-inductive current it is possible to reduce the stress on the magnetic components due to the reduced flux variation needed. In this way the content of energy needed for a plasma pulse is reduced or, alternatively, the pulse duration can be increased, up to the condition where the ohmic transformer is no more needed.

Furthermore, with localised current drive the shape of the plasma current profile can be modified. A profile different from the inductive profile (bell-shaped with peak on the plasma center) allows to access different transport regimes (e.g. improved H mode with a flat current profile in the core or internal transport barriers with a local maximum in the current profile) and stabilise some magneto-hydrodynamics instabilities such as the neoclassical tearing modes. Among the different heating systems, NB has the broader current profile because the absorption (ionisation) of the particles doesn't have a resonance which allows the particles to remain focused in a specific area; in the case of ECRH, the resonance condition allows to have a narrow current density profile. Nevertheless, the current drive efficiency from the neutral beam is greater than ECRH.

At first, neutral beam current drive (NBCD) can be approximated as the injected current multiplied by the number of turns the fast ions accomplish in the tokamak plasma, which yields:

$$I_{circ} = I_0 \frac{\langle v_\parallel \rangle \tau_s}{2\pi R_0} \tag{2.40}$$

where I_0 is the injected current, $\langle v_\parallel \rangle$ is the average parallel velocity, τ_s the slowing-down time, $2\pi R_0$ the length of the plasma magnetic axis. This calculation can become more complex by considering the correct average of the slowing-down process and the pitch angle scattering included in the Fokker-Planck equation.

Furthermore, this model doesn't take into account the effect of the bulk electrons. In fact, when the fast ions circulate, the electrons are dragged with them and generate a "back electron current" which has the opposite sign of the fast ions current. The correction adding the back-stream lectron current is

$$I_{CD} = I_{circ} \left(1 - \frac{Z_{beam}}{Z_{eff}}\right) \tag{2.41}$$

being Z_{beam} the number of protons in the injected atoms. These two currents are the same if $Z_{beam} = Z_{eff}$. In a neoclassical framework (considering 3D effects and in particular trapped electrons) a current is driven also if $Z_{beam} = Z_{eff}$ because trapped electrons do not contribute to the cancellation of the ion current:

$$I_{CD} = I_{circ} \left[1 - \frac{Z_{beam}}{Z_{eff}} \left(1 - G(Z_{eff}, \epsilon)\right)\right] \tag{2.42}$$

being G the factor taking into account the trapped electrons (and $\epsilon = r/R_0$ the inverse aspect ratio)

$$G(Z_{eff}, \epsilon) = \left(1.55 + \frac{0.85}{Z_{eff}}\right)\sqrt{\epsilon} - \left(0.22 + \frac{1.55}{Z_{eff}}\right)\epsilon \tag{2.43}$$

The factor between the circulating current and the shielded current (i.e. the one considering the electrons) is shown in figure 2.9.

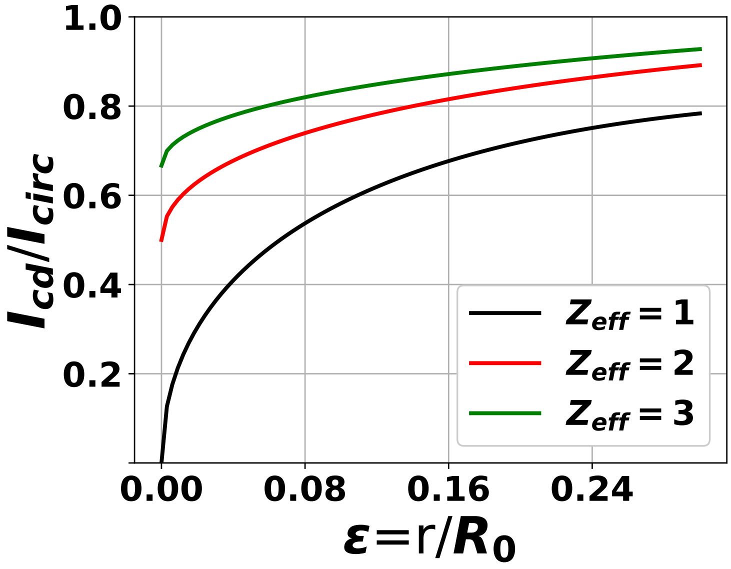

FIGURE 2.9: Shielding factor for different Z_{eff} at different ϵ. Z_{beam} has been set to 1.

A parameter interesting under an engineering point of view is the efficiency of the current drive system, i.e. the amount of driven current per power coupled to the plasma:

$$\epsilon_{CD} = \frac{I_{CD}}{P} \tag{2.44}$$

Given that for all the current drive systems

$$I_{CD} \propto P \cdot \frac{1}{n_e}\frac{1}{R_0} \tag{2.45}$$

the current drive efficiency to compare different systems is

$$\eta_{CD} = R_0 n_e \frac{I_{CD}}{P} \left[\frac{10^{20} A}{W m^2}\right] \tag{2.46}$$

2.7 Additional effects

NBs do not only contribute to plasma with power deposition and current drive: some additional effects can be used.

The energetic particles (EP) injected with the beam can be used as fueling to compensate the plasma particles lost. This effect is relevant for small and low-density tokamaks, but for reactor-size experiments it would be negligible. *Fueling-EP*

The injection of particles in tangential direction results in an increased bulk ion toroidal velocity, thus a toroidal torque is applied to the plasma [23] [24]. This is interesting, for example, for stabilisation of magneto-hydrodynamics instabilities. The toroidal torque can be expressed as: *Toroidal rotation*

$$\mathbf{M} = \frac{I_0}{e} A_{beam} m_p v_0 R_t \mathbf{e}_\phi \propto P_{NBI} \sqrt{\frac{A_{beam}}{E_0}} \tag{2.47}$$

with A_{beam} the atomic mass of the injected neutrals. The last relation is true since $I_0 = P_{NBI}/E_0$ and $v_0 \propto \sqrt{E_0/A_{beam}}$, being E_0 the fast particles energy. For reactor-size tokamak the injected momentum density will be low: E_0 will be much higher than present-day experiments (to increase the penetration of the beam in the plasma core) and, even though the confinement time will be higher, the volume will be higher as well, reducing the momentum density.

Lastly, the beam ions can be used as diagnostic for example by charge-exchange spectroscopy (Fast Ions D-Alpha spectroscopy) [25], beam emission spectroscopy [26] and neutron emission. *Diagnostic*

2.8 Modelling

Modelling of fast ions orbits and collisions in a tokamak (i.e. solving the Fokker-Planck equation) requires some computational effort, depending on the degree of quality required. Here below three codes will be presented: METIS [27], NUBEAM [28] [29], ASCOT [30] [31] [32].

METIS (Minute Embedded Tokamak Integrated Simulator) is a fast analytical solver of a full tokamak discharge and includes a module to compute the NBI ionisation and slowing-down while the other codes use Monte Carlo models for this purpose.

2.8.1 Codes input

A certain degree of complexity in the input to these class of codes is given by the neutral beam injector. There are mainly three models for a beam injector:

- **Pencil-like** the beam is considered as a single line entering the plasma, without any description of the grid shape nor any divergence. This is the model METIS uses and in this code the spread of the beam is simulated replicating each injection line 3 times vertically and 3 times horizontally;

- **Narrow beam** the beam has a single line of propagation but its width changes according to its divergence and focus. Here as well the beam grid is not included. This is the model included in NUBEAM;

- **Beamlet-by-beamlet** the beam is modeled as a sum of narrow beamlets, each one with its trajectory and divergence. This gives the highest accurancy in the beam trajectory and sizes, but can be quite complex to implement. ASCOT uses this model.

The other essential input for the codes are the plasma properties: for these codes the electron density and temperature, the ion density and temperature, the plasma composition and the magnetic fields are needed. The vacuum vessel geometry is also necessary to compute the wall losses.

Not all the codes compute charge-exchange reactions. NUBEAM includes all the possible collisions (ionisation and CX) with bulk plasma, high Z impurities and the fast ions already in the plasma. ASCOT, on the other hand, does not include charge-exchange yet.

According to equation 2.3, the attenuation of the beam requires calculation of the beam trajectory, the plasma density and the cross-sections which depend on the plasma temperature and composition. In the case of METIS, the beam attenuation is computed with the relation expressed in 2.3.

METIS doesn't compute the full orbit of the markers but it accounts for first orbit losses in a simplified way. Given the ionisation position, the width of the orbit is computed using equation 2.48 [33]. If the ionisation position from the wall is smaller than δ_p, the particle (and its relative power) is considered lost.

$$\delta_p = \left(\frac{2 q_0 v_{\perp 0}}{\omega_0 R_0} \right)^{2/3} R_0 \tag{2.48}$$

In this equation, q_0 is the safety factor at the plasma axis, $v_{\perp 0}$ is the initial perpendicular velocity of the particle, ω_0 is the initial cyclotron frequency of the fast ion, R_0 is the major radius.

The steady-state distribution function of the particles used in METIS is 2.38. Starting from the distribution function, the EP pressure, the power deposited to the plasma and the current-drive can be computed. In this code, the charge-exchange losses are not included as loss channel.

2.8.2 Monte Carlo solvers of the Fokker-Planck equation for EP physics - ASCOT and NUBEAM

Monte Carlo codes (BBNBI[3] / ASCOT and NUBEAM) solve the ionisation equation 2.3 considering the trajectory of each neutral marker and calculating the probability of the ionizing collision using Monte Carlo methods. The ionization equation solution is usually fast and runs in some minutes, depending on the number of markers. The advantage of having a high number of markers (N) is the reduction of the statistical error $\sigma \sim 1/\sqrt{N}$. This effect is shown in figure 2.10.

The marker simulated has an assigned *weight*, which represents the amount of particles each marker carries (around 10^{16} particles): each marker represents a flux of particles. Computationally this marker is a single particle (i.e. the equations are solved as if it is a single particle), the difference is in the power it carries, used to compute the quantities deposited on the plasma.

---

[3] BBNBI is the code computing beam deposition for ASCOT

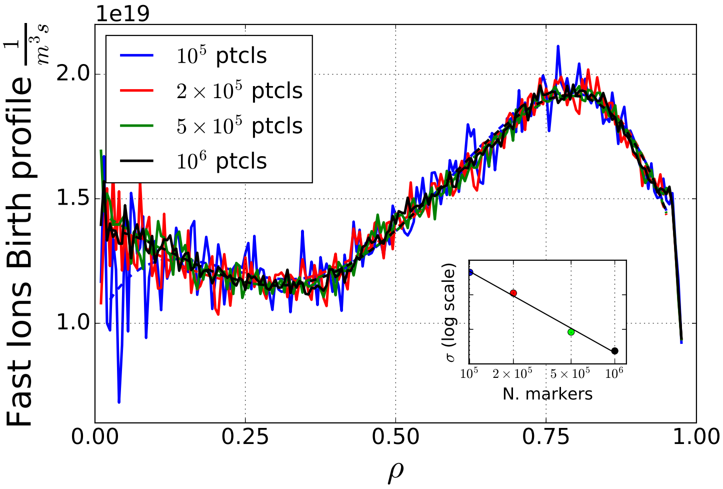

FIGURE 2.10: BBNBI fast ion birth profile for different amount of markers. In the small plot, the variance of the curves is shown against the number of markers in log scale.

The Monte Carlo solvers of the Fokker-Planck equation solve the orbits of the marker and fill a N-dimensional histogram to compute the distribution function of the particles (accounting for the weights). This method is much slower but can take into account effects which are not included in equation 2.38.

For each timestep, at first the particle orbit is evolved according to the Lorentz force, then the collisions are computed, modifying the velocity of the marker. Lastly a N-dimensional histogram is filled according to the weight of the marker. This histogram is made of N-dimensional boxes where the dimensions can be R, z, energy, pitch, etc. In this way, both the orbits and the steady-state distribution function can be computed. The difference in the codes are in the orbit calculations (full gyro-motion or guiding center), the dimensionality of the tokamak and magnetic field (i.e. 2D or 3D), the treatment of the Coulomb/atomic collisions.

NUBEAM is the code used within the TRANSP code [34]. The fast ion orbits are modelled accounting only for the gyro-motion, and the finite Larmor radius effects are computed with a statystical method (i.e. the marker is shifted of a gyro-radius in a random poloidal direction). The Fokker-Planck equation is approximated using only small-angle binary collisions, considering $v_i < v_b < v_e$ and neglecting terms in order of $\left(\frac{T_e}{E_0}\right)^2$ and $\exp -E_0/T_i$. In these conditions, the average changes $\langle \Delta v^2 \rangle$ and $\langle \Delta \xi^2 \rangle$ can be computed

$$\langle \Delta v^2 \rangle = \frac{2\delta_t}{\tau_s} \left(\frac{T_e}{m_b} + \frac{v_c^3}{v^3} \frac{T_i}{m_b} \right) \tag{2.49a}$$

$$\langle \Delta \xi^2 \rangle = \delta_t \nu_{ii} (1 - \xi_0^2) \tag{2.49b}$$

and these values are used as the width of the gaussian for the Monte Carlo calculations of the change in energy and pitch. NUBEAM is a 2D solver, thus 3D effects cannot be computed with this code.

ASCOT solves both the gyro-centre motion and the full gyro-orbit. It can shift between the two methods (i.e. the two hamiltonians) when approaching the wall, to compute the orbit losses. Being ASCOT a 3D code, it can model also the fast-ion losses given by magnetic ripple (the variation of the magnetic field given by the discrete number of coils). The Coulomb collisions are computed using operators acting in the velocity space. The collisional component of the Fokker-Plank equation is written as:

$$\left(\frac{\partial f}{\partial t}\right)_{coll} = -\frac{\partial}{\partial \mathbf{v}} \cdot \left[\mathbf{A} f - \frac{1}{2}\frac{\partial}{\partial \mathbf{v}} \cdot (\mathbf{D} f)\right] \tag{2.50}$$

where **A** can be considered as a friction term and **D** as a velocity diffusion term. The drag term is included in the deterministic part of the motion, the diffusive terms are computed with the stochastic Euler method. The guiding centre transformation should be applied also to this collisional term, not only the equations of motion. This diffusion in space is computed only up to the zeroth order in magnetic field non-uniformity.

2.9 Improved confinement: H-mode and advanced tokamak

2.9.1 H-mode

High-confinement mode (H-mode) is a tokamak regime where the particle (and energy) confinement time almost doubles [35] [36]. H-mode was at first discovered in ASDEX tokamak [37]: when sufficient additional power was applied to the tokamak plasma, the transport at the edge decreased, making the profiles there steeper (and creating a so-called pedestal, see figure 2.11). An Edge Transport Barrier (ETB) there created, increasing the plasma pressure in all the plasma.

Nowadays many theories interplay to explain the H-mode transition, but no one satisfy all the observation at the same time [38]. Under an experimental point of view, the main parameter which seems to play a role in the transition to H-mode is the additional power injected in the plasma, which must overcome a certain threshold. This threshold has been evaluated experimentally and some scalings have been extrapolated. The one used in this work is presented in 2.51 [39]:

$$P_{LH}^{Threshold} = 2.15 \cdot e^{0.107} \cdot n_{20}^{0.782} \cdot B_T^{0.772} \cdot a^{0.975} \cdot R_0^{0.999} \tag{2.51}$$

where e is the euler number, n_{20} the plasma line-averaged density (in $1 \times 10^{20}\,\mathrm{m}^{-3}$), B_T the toroidal field, a the minor radius and R_0 the major radius.

The H-mode scenario is the scenario under which ITER has been designed. Achieving H-mode in a device is important because of the confinement increase and the higher pressure values which can be achieved.

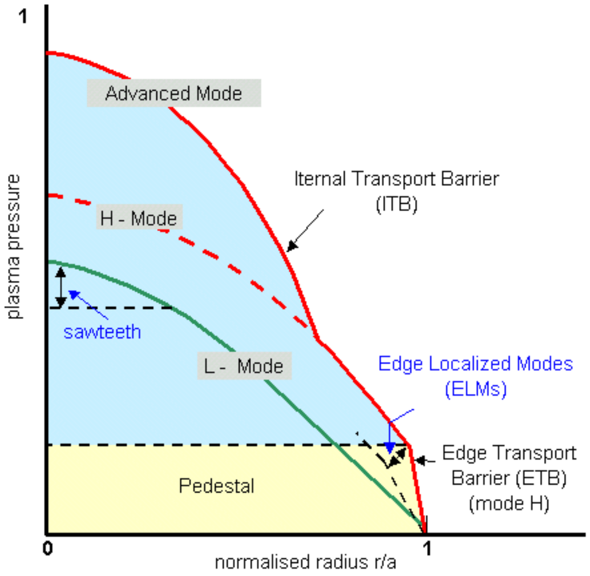

FIGURE 2.11: Plasma pressure cartoon for different transport barriers. Green line is the mode without any transport barriers (L-mode), dotted red is the H-mode, where only the ETB is present, solid red is the case where an internal transport barrier is created.

2.9.2 Advanced tokamak scenarios

Advanced tokamak (AT) scenarios [40] [41] [42] foresee to strongly limit the use of the central solenoid to drive plasma current, achieving long-pulse and even steady-state operation.

The current must then be driven using other ways. One is the current-drive effect given by auxiliary heating systems (such as NBI and EC). The other non-inductive current in a tokamak is the bootstrap current [43], which is produced by the population of different trapped particles: adjacent trapped particle orbits provide a momentum imbalance that can be transferred to passing particles by collisions. This current is parallel to the magnetic field and requires the presence of a trapped population and a pressure gradient. Increasing the normalised pressure a large fraction of bootstrap current can be achieved. In the case of JT60-SA tokamak, this current should reach 50% of the total current.

The bootstrap current density in a tokamak goes roughly like

$$j_{BS} \sim \left(\frac{r}{R}\right)^{1/2} \frac{\nabla p}{B_{pol}} \tag{2.52}$$

which means that at lower current (i.e. lower poloidal magnetic field) the current is maximized.

High pressure gradients maximize the bootstrap current as well and this can be done with internal transport barriers (ITBs)[44]: with ITBs the internal transport is reduced, increasing the pressure gradients. This condition can be achieved by reversal of the q-profile, i.e. by making the radial derivative of the q-profile to change sign. Inductive currents (centered on the axis) make the q-profile to be monotonically increasing with radius, but if off-axis current is driven (using e.g. NBI) then the profile gets reversed. In figure 2.12 the typical q-profiles for different tokamak scenarios are shown.

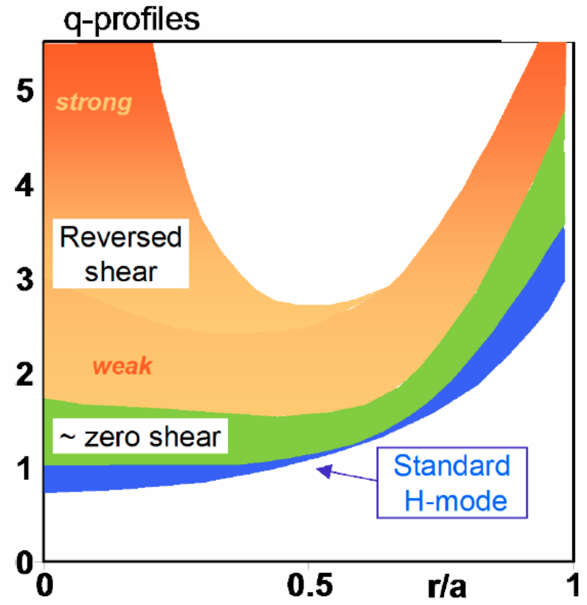

FIGURE 2.12: Safety factor profile for conventional and advanced tokamak scenarios.

In this thesis two kind of advanced scenarios will be presented:

- 'hybrid' scenario: in this case, the total current should be driven 50% non inductively, in order to guarantee a long pulse operation. This scenario is also called 'improved H-mode' because it has and higher confinement with respect to L-mode so it is promising (for ITER) for a high neutron fluency. For this regime, the q value would be in the range 1.0-1.5 with shear close to 0.0. This slightly raised value of q in the core would avoid the sawtooth activity, which could trigger neoclassical tearing modes in standard H-mode plasmas.
- steady-state scenario: the current in this case will be fully generated non-inductively. This requires a high β_N (>4)and the q-profile in this case will be strongly reversed

Chapter 3

Predictive studies on RFX-mod discharges

In this chapter, simulations of NBI on RFX-mod tokamak device will be presented. The motivations of this work lie in the upgrade of the machine, which could include also the implementation of a heating neutral beam injector, aside with the diagnostic beam already installed. The results here presented show the heating efficiency of the beam and the possibility of the transition to the H-mode in this device with the additional NB power injected. The model for neutral beam power loss from METIS is compared to NUBEAM Montecarlo Fokker-Planck solver, showing the limitations of the first model applied to NBI in low-field tokamak plasmas.

3.1 RFX-mod and its upgrade

RFX-mod [45] is a medium-size device ($R_0 = 2\,\mathrm{m}$, $a = 0.5\,\mathrm{m}$) designed to operate as a reversed-field pinch (RFP) or a low-field tokamak($B_\phi \sim 0.6\,\mathrm{T}$). It is the biggest operating RFP and, in this configuration, it reached the record current of 2 MA [46] and the quasi-single helicity mode has been observed in this device for the first time [47]. Under the structural point of view, this machine has a thick copper shell (between the vacuum vessel and the mechanical support structure) to increase the current diffusion time.

In addition, this machine is fully covered with a system of 192 active saddle coils which objective is to reduce the amplitude of the MHD external kink instability inherently living within the RFP configuration. These coils have been also used in tokamak configuration to control the disruptive behaviour arising when $q(a) < 2$ is reached; in RFX-mod, stationary tokamak plasmas below the disruptive q limit have been obtained.

The device is currently under upgrade. Some work involves repairing some of the saddle coils but the major challenge is to reduce a layer in the tokamak structure: the vacuum vessel is to be removed from the tokamak and the mechanical structure will be its substitute. This means that the mechanical structure must guarantee good vacuum conditions and the graphite tiles composing the first wall must be installed in the copper shell. This modification will increase the plasma volume and make the saddle coils closer to the plasma, increasing their effectiveness [48].

Another planned upgrade for RFX-mod2 is the implementation of a neutral beam injector. Using NBI on a RFP has some benefits for studying fast particle population in this particular magnetic configuration, but it is not so meaningful in power deposition: due to the high resistivity of RFP configuration, the ohmic power in a RFP (∼20 MW) is higher than the one in a comparable tokamak, this means that high-power neutral beams would be needed to be meaningful for power deposition.

Comparison between fast particles behaviour in tokamak and RFPs [49] shows that NTM in the former configuration increase the fast ion losses, while in RFP the fast ion confinement time is larger than that of the thermal ions despite the presence of a large number of saturated tearing modes.

NBI in RFP plasmas has been already studied on different devices such as MST1 in Wisconsin (USA) [50] and TPE-RX experiment at AIST institute (Tsukuba, Japan) [51].

The available tools for NBI modelling need a magnetic equilibrium with a toroidal flux which doesn't change sign. This is not the case in RFPs, so modelling can be done limiting the plasma to the $B_\phi = 0$ surface, as work [52] shows.

Modelling of NBI in RFX-mod used as a RFP is not the topic of this thesis: in this chapter the feasibility study of NBI in RFX-mod tokamak is presented. In RFX-mod tokamak the additional heating power given by the neutral beam (summing up to the 200 kW ohmic power) could widen the space parameter explored in low-q configuration and lead to the transition to the H-mode, allowing to study the physics of Edge Localised Modes (ELM) in presence of the powerful active control system RFX-mod is equipped with.

3.1.1 AIST neutral beam injector & the implementation in RFX-mod

Thanks to a collaboration between AIST and Consorzio RFX, the same neutral beam injector used on TPE-RX is available for RFX-mod2.

This injector was designed to work at a nominal power of 1.25 MW, accelerating up to 60 A of 25 keV H^+ for 30 ms [53] [54]. D ions can be used but at reduced power (∼0.8 MW) [1]. If necessary, the injection time can be increased to 60 ms, reducing the energy to 15 keV.

The accelerator design is common to the majority of positive-sourced NB injector, with three multi-aperture electrostatic grids. The focal length is 1860 mm and the effective diameter measured is 345 mm at the extraction plate, 36 mm at the focal point. The estimated beam divergence is $\theta \sim 0.8°$.

The implementation of AIST beam in RFX-mod has been already studied in [55] [56]. Attention must be given to the strong magnetic field outside the vacuum vessel, which could deteriorate the beam optics before entering the plasma. The actual integration design ensures an efficiency between the power supplied to the injector and the power to the plasma $\eta > 25\%$. The only possible injection is along a radial chord on the equatorial plane due to mechanical constraints mainly linked to toroidal field coils configuration. The NB system integration design can be seen in figure 3.1.

---

[1] Assuming the same injection voltage, we get a dependency of the power with the mass. $P = I \cdot E = (q \cdot v) \cdot (q \cdot \Delta V) = q^2 \Delta V \sqrt{\frac{2E}{m}} = K \cdot \frac{1}{m^{0.5}}$. With this relation, the power in the case of D ions can be found

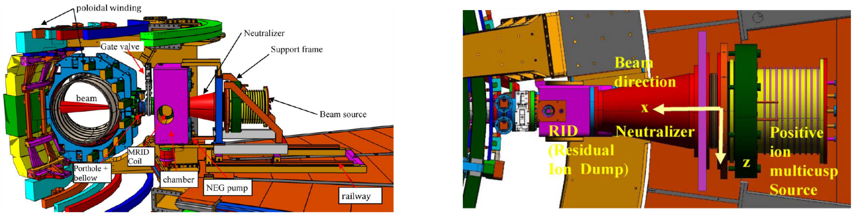

(A) (B)

FIGURE 3.1: Design of integration of NB system into RFX-mod. (a) overall design, (b) beam detail

3.2 METIS design of RFX-mod tokamak discharges

The tool chosen for this feasibility study is METIS, thanks to its speed in simulating a plasma discharge and its accuracy, which is satisfying for this study. The results of this study are presented in [57].

For each simulated discharge, METIS needs as input the time dependence of plasma current and density, the geometry of the plasma (last closed flux surface shape, major and minor radius), the plasma composition and the additional heating (NBI or waves). The other parameters, such as the plasma composition, the impurities, the transport coefficients, the MHD instabilities parameters, the profiles shape, neoclassical effects and L–H transition coefficients are evaluated with calculations and validation with experimental data. METIS has an internal solver for the plasma magnetic equilibrium.

Although METIS has been widely used to simulate different tokamaks, a RFX-mod discharge has never been simulated with METIS so far. We therefore performed METIS simulation of some reference RFX shots and we compared with the experimental data showing a good agreement (in figure 3.2 an example is shown). In these simulations careful attention has been given to the flattop phase.

Having a good dataset capable of simulating RFX-mod circular tokamak discharges with METIS, a set of densities has been chosen (see table 3.1) . The values of the line-averaged densities are representative of RFX-mod plasmas. This database of simulations has been used in this work to study the effect of the implementation of a NB system. As it can be noted, the plasma current (thus the Greenwald density) is kept fixed all over the shots (during the flattop, I_p =120 kA, q_a =2.3). The plasma composition is unvaried (main gas D, with C and Li as impurities) while the density profile peaking factor (n_0/n) has been estimated by the measurements for each shot. It varies between 1.1 for the UH shot and 1.3 for the UL shot.

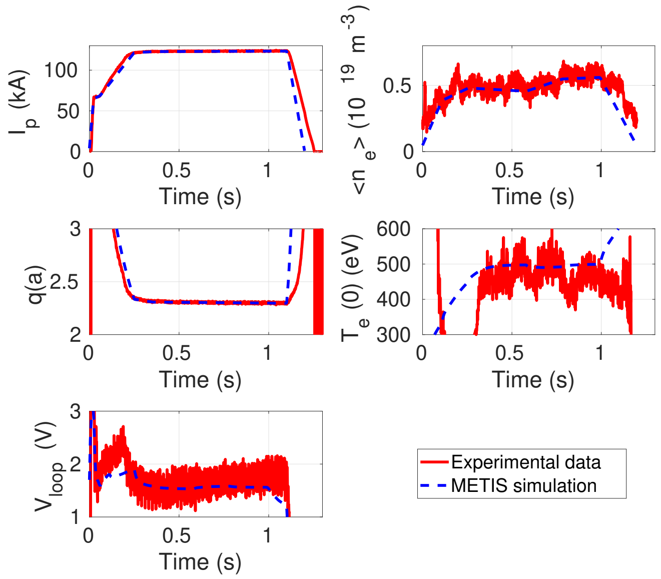

FIGURE 3.2: Comparison between experimental data and METIS simulation.

Shot	Label	Name	$\langle n_e \rangle (10^{18}\,\mathrm{m}^{-3})$	$\langle n_e \rangle / n_G$ (%)	$P_{LH}[kW]$
38706	UL	Ultra-Low	2.5	13	110
38688	L	Low	6	32	208
38691	M	Medium	10	53	303
38722	H	High	14	75	387
38717	UH	Ultra-High	18.7	100	478

TABLE 3.1: Density for reference shots. $\langle n_e \rangle$ is the line-averaged density. The last column list the power required for L-H transition, computed with scaling in [39].

It is important to notice some limitations of METIS code. We were aware of these limitations, but the purpose of the study could stand them. The limitations listed in section 2.8 must be kept in mind (in particular the analytical solutions of the equation ruling fast-ions physics) and, furthermore, METIS approach cannot stand strong variation of parameters such as beam turning on and off. This can be seen in the figures presented in the study. The beam population simulated is composed only by H^+ (D^+), while in positive-based beam sources the accelerated ions are also ${H_2}^+$(${D_2}^+$) and ${H_3}^+$(${D_3}^+$). Lastly, the beam injection geometry is not as precise as other modelling tools allow it to be.

3.3 METIS predictive simulations of NBI on RFX-mod

The reference scenario for beam injection in RFX-mod is injecting D atoms at 25 keV for a total power of 0.8 MW for 30 ms. In this study, this has been addressed as the first case of study but also the backup reference has been analysed: in this latter case, the energy is limited to 15 keV and the time to 60 ms.

One of the main issues when designing a NBI heating system is the shine-through, i.e. the beam fraction which does not get ionised. This becomes power deposited to the wall. In the case of RFX-mod, the power deposited to the wall is not mechanically harmful for the graphite tiles. The problem is the outgassing of heavy impurities which can pollute the plasma and eventually drive a shutdown.

In figure 3.3 the total beam losses computed by METIS (i.e. shine-through fraction and first orbit losses) are shown as function of the densities. As expected, the losses reduce when increasing the density and get below 75 % above the M shot. This happens mainly because the higher density allows a higher absorption of the beam, reducing the shine-through. This forced us to avoid further analysis of shots L and UL, since NBI would be impossible in such kind of plasmas.

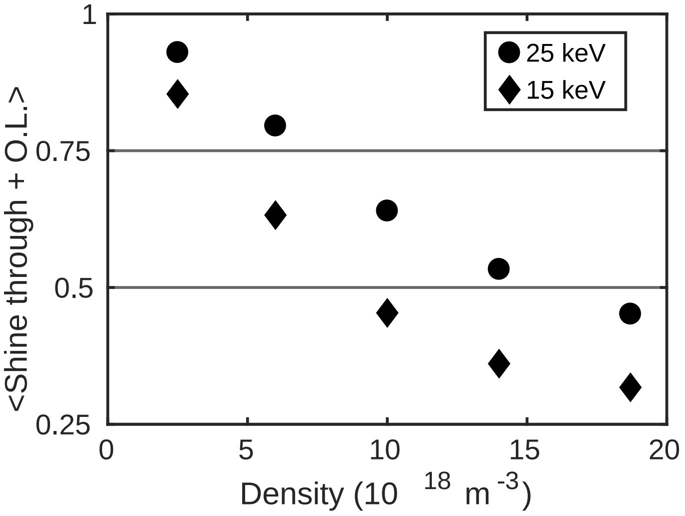

FIGURE 3.3: Shine-through and first orbit losses as function of the densities.

3.3.1 Reference energy and power

The reference power is both the most useful to deposit power to the plasma but also the most harmful in terms of shine-through, as figure 3.4 shows. The power is deposited mostly on plasma core (sub-figure (a)) and increases with increasing density, i.e. increasing power absorbed by the plasma. This is perfectly compatible with the radial injection geometry, which aims at the plasma central column. Sub-figure (b) illustrates that central plasma temperature increases around 50 % compared to the case without NBI. In image (c) the ratio of ion temperature over electron temperature is shown: NBI can modify the ratio of these two values thus allowing to explore different transport regime, in particular if ions become hotter than electrons. In this case, the ratio remains below one because at this energy the beam deposit mostly power to the electrons. At lower densities the ratio has a stronger increase, indicating that beam ions couple mostly with bulk ions. Figure (d) shows that the slowing-down time of the EP is well below the plasma duration, so the EP have time to deposit the power they have to the plasma. Note that the slowing-down time is comparable to the injection time.

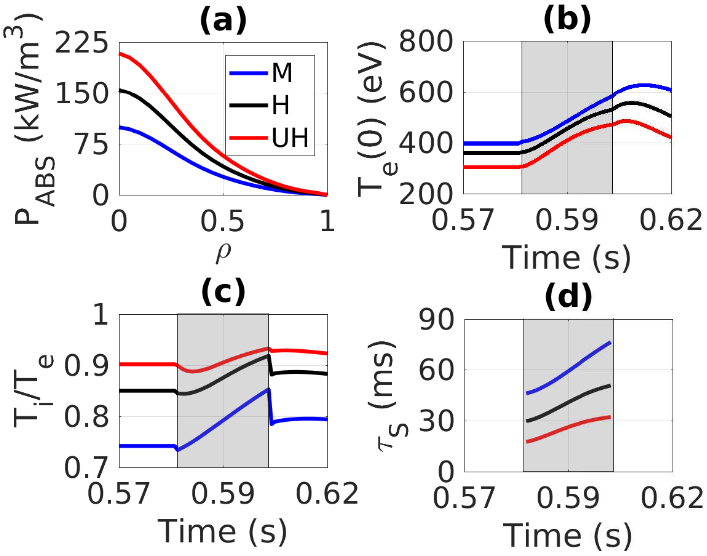

FIGURE 3.4: NBI for injection energy of 25 keV. The colors label the different shots considered (blue-53% n/n_G, black-75% n/n_G, red-100% n/n_G). The grey area represents the injection window.

3.3.2 Reduced energy and power

Energy of AIST beam can be modified to 15 keV. The power injected has been modified accordingly to the relation between energy and power given by equation 2.1.

In this case, it seems that the most significant effect is the increase of the injection window length (figure 3.5). The deposited power in a single timeslice (subfigure (a)) is slightly lower than the case at 25 keV and this is due to the smaller amount of power injected and thus absorbed by the plasma, which has also lower energy to penetrate into the plasma core. Temperatures and slowing-down time reach a saturation value. Also the ratio T_i/T_e (subfigure (c)) seems to reach a saturation, and this effect is more evident at higher densities: this ration is higher in this case since, at lower injection energy, the power is preferably transferred to ions. In fact the value of 1 is exceeded for all the three shots analysed, allowing different transport regimes.

3.3.3 Power redistribution

NBI in RFX-mod would result mostly in heating the electrons, as figure 3.6 shows. In the plot, the three lines represent the M, H and UH discharges. The range they cover (which can be read both in the bottom and top axis, giving complementary information) indicates the fraction of power they give to the different species all over the beam injection. The fraction of power

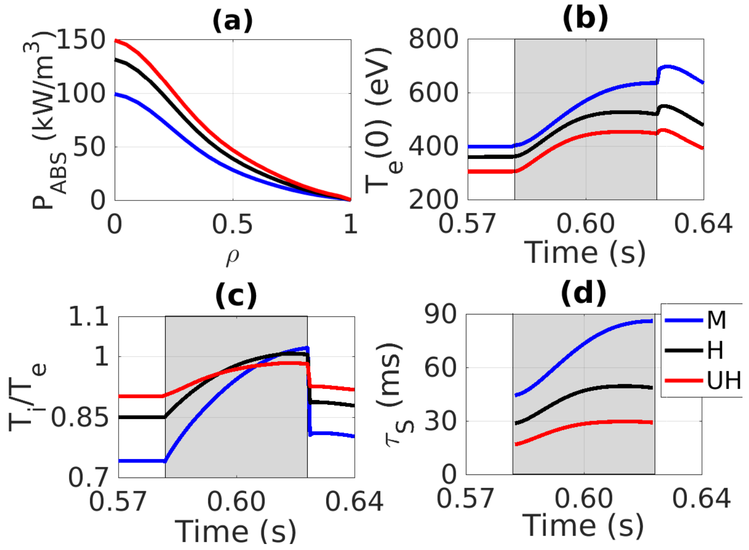

FIGURE 3.5: NBI for injection energy of 15 keV. The colors label the different shots considered (blue-53% n/n_G, black-75% n/n_G, red-100% n/n_G). The grey area represents the injection window.

given to electrons is higher than 55 % at 25 keV and reaches 40 % for 15 keV. In the latter case, the range of redistribution spanned is wider, and this is due mostly to the strong change in plasma temperature.

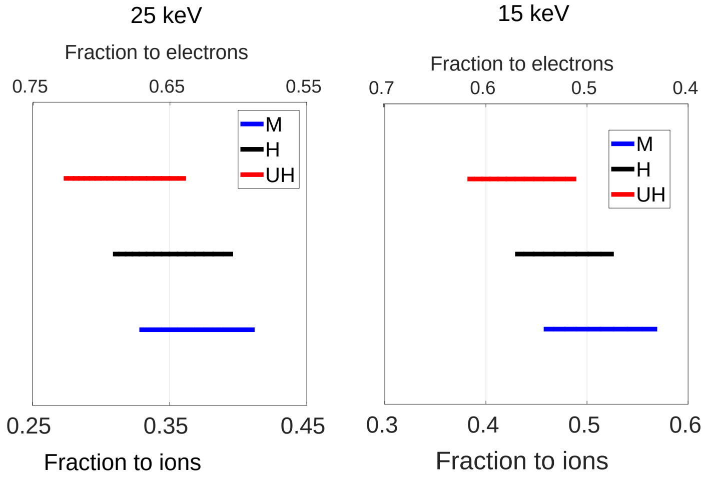

FIGURE 3.6: Redistribution between ions and electrons

3.3.4 H-mode transition

The addition of NB power can lead to a L-H transition: in usual RFX-mod tokamak ohmic discharges, the power flowing through the separatrix is close to the threshold to reach the H mode [58]. The scaling law for the threshold power used is "Martin scaling" and it's taken from [39]

$$P_{LH}^{Threshold} = 2.15 \cdot e^{0.107} \cdot n_{20}^{0.782} \cdot B_T^{0.772} \cdot a^{0.975} \cdot R_0^{0.999} \tag{3.1}$$

where e is the Euler number , n_{20} the plasma line-averaged density (in $1 \times 10^{20}\,\mathrm{m}^{-3}$), B_T the toroidal field (0.6 T in the shots here explored), a the minor radius ($\sim$0.5 m) and R_0 the major radius (2 m for RFX-mod).

In figure 3.7 it is shown that during the beam injection at 25 keV the power becomes higher than the threshold power needed and thus the H-mode can be reached. At 15 keV the power is too low to induce the L-H transition.

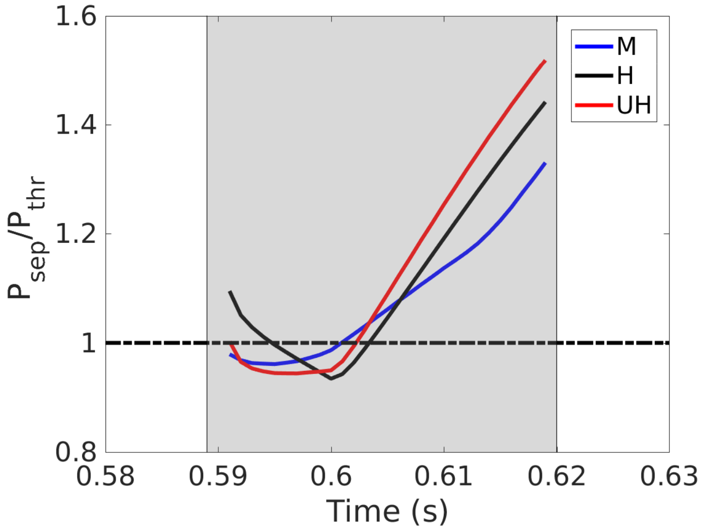

FIGURE 3.7: L-H transition power threshold at 25 keV

3.3.5 Comparisons of fast ion orbit losses between METIS and NUBEAM

RFX-mod device is a low-magnetic field tokamak ($B_T \sim 0.6$ T). This feature is harmful for fast ion confinement because the low magnetic fields cause big orbit drifts, which can make the particles collide with the wall.

The model accounting for fast ion orbit losses in METIS has been described in section 2.8, where the orbit width is computed using an analytical formula which considers the initial position, velocity and magnetic field where a particle is ionized. This model is applied to tokamak plasmas with high toroidal magnetic field (compared to pressure), and the approximations made to compute the orbit width can no more be applicable for RFX-mod.

In order to test if METIS model correctly applies to RFX-mod tokamak discharges, a comparison with NUBEAM module has been made. The UH case with injection energy of 25 keV has been chosen, because of its high beam absorption, compared to the other cases. In this case, the plasma profiles are taken from METIS evaluation, while NUBEAM has been applied to the target plasma. No charge-exchange losses from NUBEAM have been considered in this case, because the purpose of this simulation is to study the applicability of the orbit-loss model from METIS.

The comparison between the two different power balances for a single time slice (t=0.6 s) are presented in figure 3.8. It can be easily noted that a strong difference arise between the two models applied to the same plasma and injection geometry. NUBEAM model results in a high fraction of power lost because of unconfined orbit (orbit losses - O.L.). A difference arises also in the shine-through fraction, which is caused as well in the difference of the models applied: NUBEAM computes the amount of markers which get to the wall and, given the weight and energy of the markers, the power lost by shine-through is computed. METIS computes the shine-through by subtraction: the beam damping is solved analytically, then power fraction lost by orbits is subtracted from the power deposited. In this way, an error in the power lost by orbit reflects in an incorrect evaluation of the shine-through.

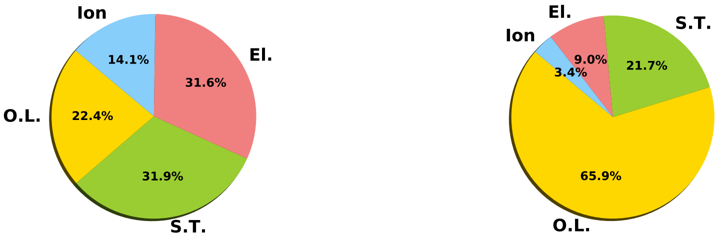

(A) (B)

FIGURE 3.8: Power balance for UH density case ($n_e \sim n_G$) computed from METIS (left) and NUBEAM (right). The numbers refer to the total injected power (800 kW in this case). Yellow is the power lost by unconfined orbits, green is the shine-through fraction, red is the power deposited to electrons and blue is the power deposited to ions.

3.4 Conclusions

In this work, METIS program has been used to simulate the integration of a NB system in RFX-mod and the limitations of its neutral beam model have been compared to NUBEAM for the case of low-field plasmas, such as RFX-mod.

Since a NB injector is already available, the simulations have been carried on with NB energy of 25 keV and 15 keV (the energies the injector can work with) and with a fixed geometry due to mechanical constraints. The injected species chosen has been D, which is the same as the target plasma main species.

Results show that the NBI with $E = 25$ keV will have a high shine-through value but the power deposited to the plasma allows to explore different scenarios with higher T_e and $T_i/T_e \sim 0.9$. Similar results are achieved with $E = 15$ keV, having the T_i/T_e value greater than unity and a lower shine-through.

The additional power deposited to the plasma by neutral beam injection can analytically lead to a transition to H-mode, according to the scaling law used in METIS. This consideration must take into account the limited model that METIS uses for the neutral beam deposition.

For the most promising case (highest density and injection energy of 25 keV), a comparison between METIS beam model and NUBEAM beam model has been carried out. A single time slice of neutral-beam injection shows that the difference in the power lost by particles in unconfined orbits is non-negligible: in NUBEAM it is almost the double than METIS. This shows a limitation in METIS model for the computation of NB losses. This happens because the analytical model used in METIS has been developed for high-field plasmas, which is not the case of RFX-mod. The full calculation of the EP orbits performed by NUBEAM shows the limitations of METIS. This poses a further complication in reaching H-mode in RFX-mod device, and the simulations carried out here could be

METIS is a powerful tool to study a tokamak discharge. It implements a NBI model which has limitations for the case of RFX-mod, because of the low magnetic field. It is still an interpretative plasma simulator which allows to explore tokamak physics in a fast and complete way, although the limitations must be known. Full solvers of the EP orbits should be applied for RFX-mod predictive discharges for an appropriate NBI model, keeping in mind the complexity of a code like NUBEAM, for example the neutral density profile which should be carefully modelled for charge-exchange losses.

Further studies involve considering neutral deuterium as a loss channel through charge exchange. This could be harmful in the cases with lower density. Given METIS limitation, a more complete analysis of the L-H transition using a more accurate model (accounting also for charge-exchange losses and orbit losses for low field tokamak plasmas) should be taken into account. Lastly different plasma shapes (like an X-point plasma), could be studied in order to asses the impact of NBI on such kind of plasmas.

Chapter 4

Predictive NBI studies on JT-60 SA

4.1 Introduction

The superconducting tokamak JT-60SA, under construction in Naka (Japan), is a device which will study advanced plasma conditions, such as steady state scenarios and break-even equivalent plasmas [59] [60] [61] [62]. The additional heating system relies on a flexible combination of electron cyclotron wave injection and neutral beams (NBs). The beam injection system is composed of 12 neutral beam units with positive ion sources (P-NB) and two beams with negative ion sources (N-NB) for a total power of 34 MW. P-NBs have a wide variety of injection geometries (perpendicular, tangential co- and counter-current) and, due to their energy (85 keV), these beams deposit most of the power on ions. The N-NBs are both tangential and co-current: this helps to control the current profiles since at the energy of 500 keV, particles couple mostly with electrons. Studying the impact of NBI EP on JT-60SA reference scenarios with Monte Carlo tools is a crucial topic for this machine because of the importance given to this actuators for plasma performance: this problem is studied in this chapter.

4.2 JT-60SA

JT-60SA [63] [64] is a superconducting tokamak under construction in Naka (J). This device is built both under the euro-japanese agreement called "Broader Approach", coherently with the Satellite Tokamak Program, and the Japanese national program. EUROfusion, as european party of the contract, contributes to the construction and exploitation of the device with economical support, design support and scientific projects. In table 4.1 the main parameters of this device are presented.

R_0[m]	2.96
a[m]	1.18
I_p [MA]	5.5
$B_{tor}(0)$ [T]	2.25
Volume [m^3]	132
Pulse length [s]	100

TABLE 4.1: Parameters of JT-60SA tokamak

The mission of JT-60SA is to support the exploitation of ITER and to research towards DEMO by addressing key physics and engineering issues. In order to obtain economically attractive steady-state DEMO reactors, the nuclear fusion research should establish reliable control schemes for high-β_N, high bootstrap fraction burning plasmas, possibly fully non-inductive.

Starting from the experimental results obtained by the tokamak devices in the world concerning highly integrated plasma performance, long pulse operation, high-density physics and plasma shaping physics, JT-60SA device and its research project have been designed. In figure 4.1 the target of the JT-60SA machine is presented. The normalized beta of the machine should be close to a DEMO-like device and the sustainment time is foreseen to get close to ITER one. This is a big improvement with respect to existing devices.

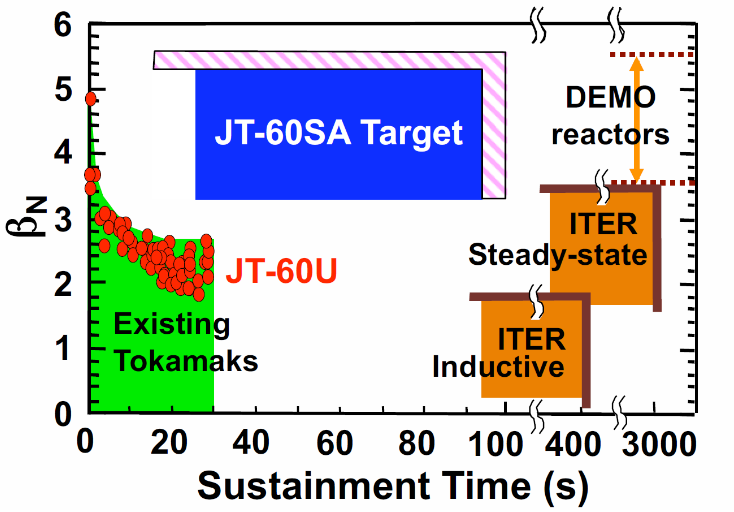

FIGURE 4.1: Target performance of JT-60SA device [59].

The presence of a population of 500 keV neutral-beam injected particles in tokamak plasmas has never been explored. These particles will be injected by a negative-sourced beam. This beam will inject the particles tangentially, but the injection elevation is shifted 0.6 m below the midplane. The main purpose of this beam is current-drive and the induced current will be off-axis peaked, allowing to reach fruitful conditions for AT scenarios. Furthermore, the EP velocity will be greater than Alfvén speed for the target scenarios, exciting Alfvén eigenmodes and allowing to study the properties of these kind of waves in such conditions.

4.3 JT-60 SA NBI system

Neutral beam heating is the most powerful auxiliary heating system JT-60SA is equipped with: it can deliver at maximum 34 MW split among 14 beam units. The injection geometry of those beams are shown in figure 4.2.

In table 4.2, the main parameters of the beams are shown

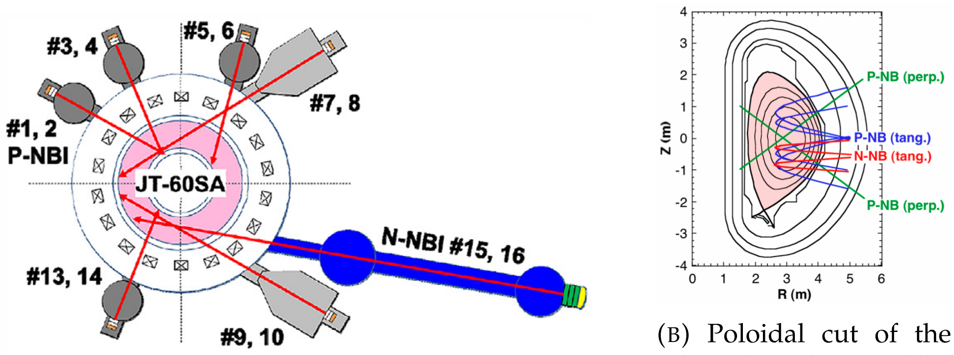

(A) Top view. The blue beam is the NNBs, all the rest are positive beams.

(B) Poloidal cut of the tokamak. To be noted the strongly off-axis injection geometry of the NNBs.

FIGURE 4.2: JT-60SA NB injection geometry

Label	Beam	Units	E [keV]	$\frac{P}{unit}$ [MW]	P_{TOT} [MW]	t [s]
P-NBs						
PP	Perpendicular-upper	4	85	2	8	100
	Perpendicular-lower	4			8	
PT	Co-tangential upper	1			2	
	Co-tangential lower	1			2	
	Ctr-tangential upper	1			2	
	Ctr-tangential lower	1			2	
N-NBs						
NNB	Co-tangential upper	1	500	5	10	100
	Co-tangential lower	1				

TABLE 4.2: Parameters of JT-60SA neutral beams

4.3.1 Positive sourced beams

The 2 MW 85 keV 27.5 A D^+ NBs [65] provide dominant ion heating and are useful for momentum injection and some current drive. The injected species can be changed to H by decreasing the power to 1.6 MW.

The maximum injected power (24 MW) is split onto 12 beams. Each beam has two independent sources (with maximum available power of 1 MW). There are 8 beams near-perpendicular (injected symmetrically from above and below the midplane), with a poloidal angle of $\sim$ 35 deg.

The layout of the beam is the same of JT-60U. The upgrade of the beamline for JT-60SA is presented in [65]. The major improvement made was the increase of the pulse length from 30 s to 100 s.

4.3.2 Negative sourced beams

The negative beams used in JT60-SA will be the most energetic beams used and its source will be the largest ion source in practical use for a nuclear fusion device. They should inject a total of 10 MW using a 22 A 500 keV D^- ion acceleration system for 100 s [66] [67] [68] [69] [70].

The negative beam is the same used for JT-60U but some improvement must be accomplished. The previous beam reached at maximum a duration of 30 s with 13 A. This upper limit was due to the change of the work function of the plasma grid: the plasma grid was inertially cooled and after a while the negative ion production (mostly given by the Cs deposited on the plasma grid) changed significantly, degrading the beam optics. This issue has been solved with active control of the plasma grid temperature.

Another issue was the beam non-uniformity. This has been solved both by changing the magnetic field configuration in the source and modifying the grid gaps.

These upgrades allowed JT-60 SA NNB to reach the reference design.

Apart from its advanced design in terms of power and energy, the beam z-position is at -0.6 m, thus this beam is injected only off-axis.

4.3.3 Modelling of JT-60 SA beams

The modelling tool chosen for NBI EP on JT60-SA is ASCOT. This code needs the output from BBNBI, which is the module calculating the ionisation of beam particles. BBNBI requires a high degree of detail concerning the beamlet configuration, and this configuration has been implemented. In figure 4.3 the grid holes design through which the particles are accelerated is shown.

Figure 4.3a shows the grid for the positive beams, which consists of 1020 holes (ø4.4 mm at the grounded grid). The grid size is 12 cm × 27 cm. Each of the positive beam is composed of two ion sources, each one having one of these grids at the end.

In figure 4.3b one of the five grids composing a single unit of the NNB is shown (rotated 90° with respect to its physical orientation). It consists of 216 apertures (ø16 mm at the grounded grid) spanned in an area of 17 cm × 44 cm. Each one of these segments is mounted as the beam grid profile in figure 4.3c shows. The grids are plane and the focus is given by the inclination shown in the figure. Each of the two beams (NNB upper and lower) is composed this way, so in the end 10 of these units will deliver the desired power.

The grids design, position and beamlet direction have been implemented for BBNBI, and the grids and direction are shown in fig 4.4 and 4.6 respectively for PNBs and NNBs. The divergence for the positive beam has been set to 1 mrad [65], while the divergence for the negative beams has been set to 5 mrad [67].

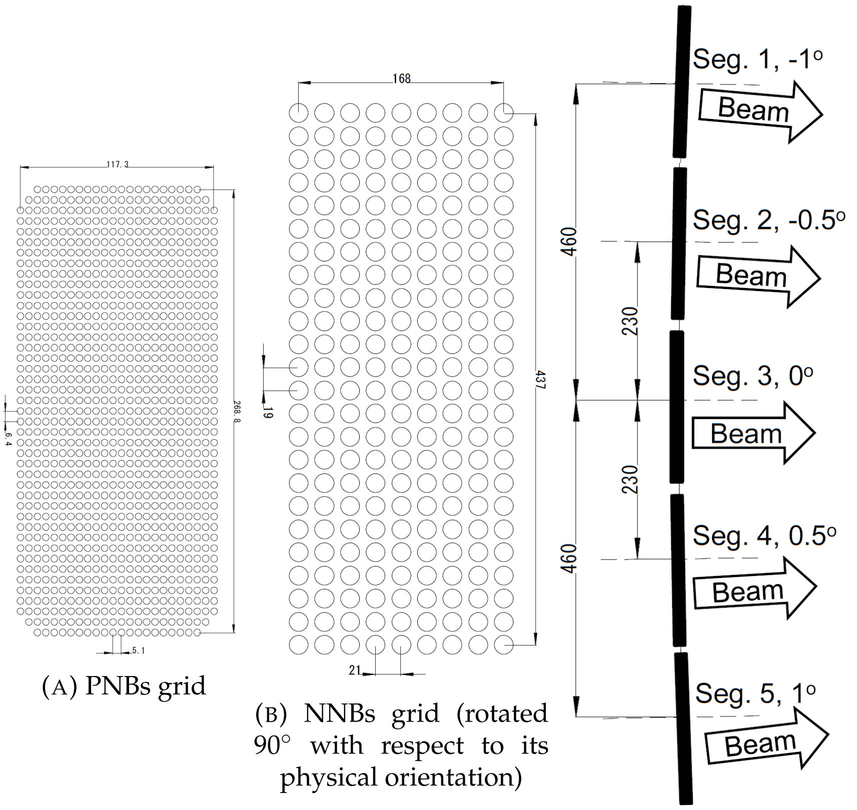
117.3
268.8
6.4
5.1
168
437
19
21
460
230
230
460
Seg. 1, -1°
Beam
Seg. 2, -0.5°
Beam
Seg. 3, 0°
Beam
Seg. 4, 0.5°
Beam
Seg. 5, 1°
Beam

(A) PNBs grid

(B) NNBs grid (rotated 90° with respect to its physical orientation)

(C) NNB grid orientation

FIGURE 4.3: Grids of JT-60SA PNBs and NNBs

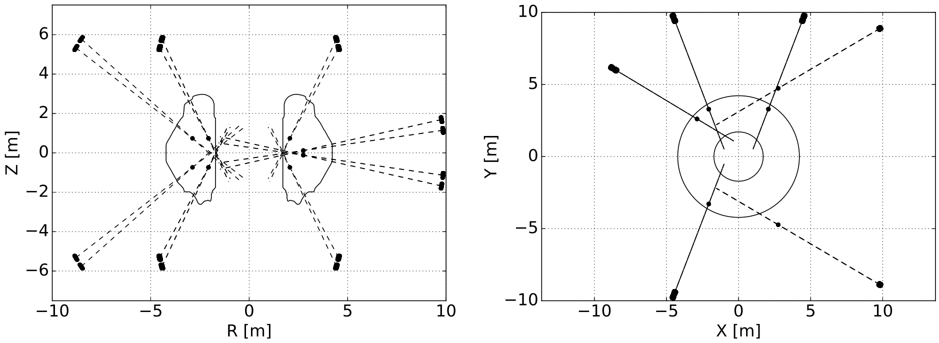

(A) Poloidal projection

(B) Top view

FIGURE 4.4: PNBs modelling grids

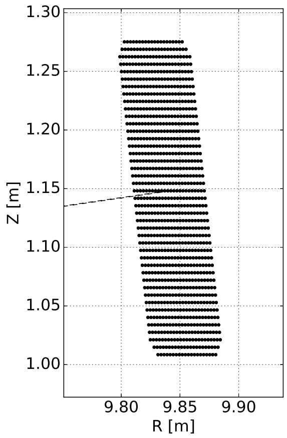

FIGURE 4.5: Zoom on a grid

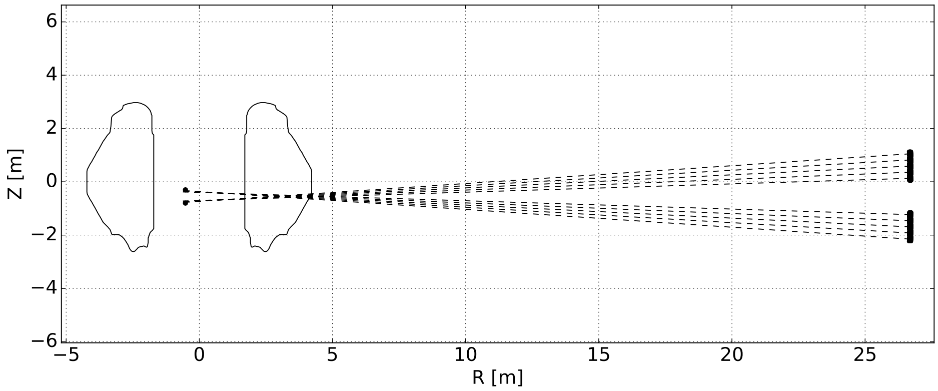

(A) Poloidal projection

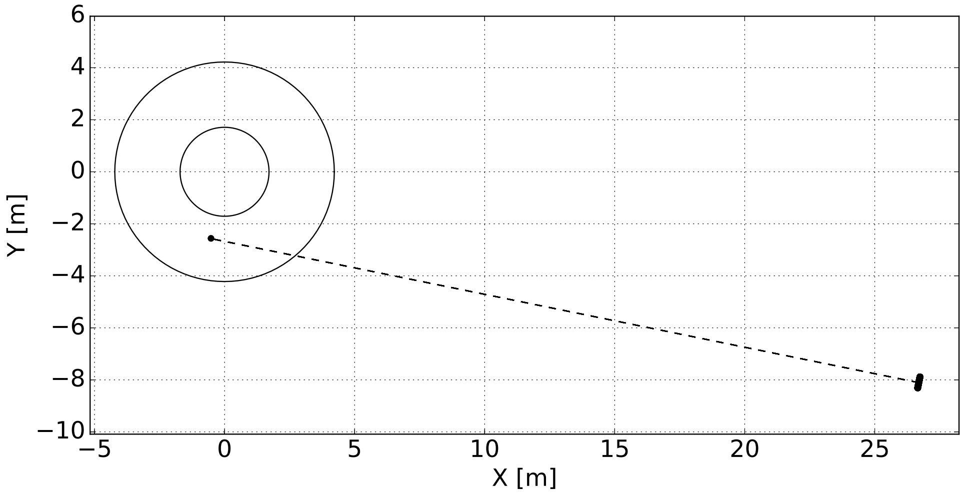

(B) Top view

FIGURE 4.6: NNBs modelling grids

4.3.4 Benchmark with integrated modelling

Integrated modelling on JT-60SA has been carried out using CRONOS suite of codes[71]. CRONOS module computing NBI EP slowing down is composed by NEMO [72] (computing ionization in an analitical way) and SPOT [73] (computing slowing down in a Monte Carlo way). The details of the codes are not given here since in this thesis only the results have been used for comparison with beam implementation in JT60-SA.

These codes have been chosen as comparison because the scenarios developed using CRONOS are the reference scenario for the european scientific community, so the narrow beam geometry implemented in these codes is validated and can be used as a benchmark. The results shown in this section should not be compared to the results shown later using ASCOT (from section 4.4 on), because the equilibrium changed in between. The validity of this comparison is given by the fruitful benchmark between the beam designs.

In order to better understand the comparison in the slowing-down quantities which will be shown, a comparison in the two different beam attenuation has been done. The comparison, shown in figure 4.7, allows to show the difference between NEMO, which computes the attenuation analytically using a narrow beam model, and BBNBI, which computes the attenuation in a Monte Carlo way using a beamlet-by-beamlet model. The beams have been shot in the same target plasma. The shape of the two fast ion birth profiles (in both cases) is really similar even if NEMO overestimates the attenuation giving a lower fast ion birth in the core. The difference is quite small for the positive beam, while it gets higher in the case of the negative beam. This difference is due partly to the different beam models, partly by the different beam attenuation models. Anyway the comparison between the two should not give strong differences in the plasma performance: the core volume is small, so the difference in integrated quantities is small as well.

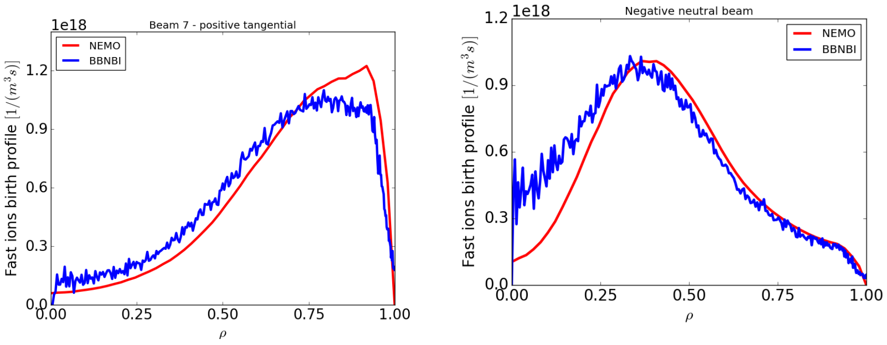

(A) Fast ion birth profile for a positive tangential co-current beam

(B) Fast ion birth profile for one negative beam

FIGURE 4.7: Comparison of beam attenuation computed by NEMO (red) and BBNBI (blue)

Availability of data allowed us to compare the induced current by the beams and the power deposited on the plasma after the full slowing-down simulation. In this case, the two simulations have the same profiles but a slight difference: the effective charge is different in magnitude, but in both cases constant over radius. This difference affects marginally the shape of the profiles.

The current (unshielded) induced by the beams is shown in figure 4.8a. It is mostly dominated by negative neutral beams (as will be shown in next sections), so this comparison can give a benchmark on the negative beams geometry implementation. It can be seen that the two profiles differ slightly in magnitude (reaching a maximum difference in the plasma core) but the shape is quite similar. The differences can be given by the difference in the beam attenuation model (shown previously in figure 4.7) and it is interesting to see that ASCOT features two separated peaks, corresponding to the two different negative beams. This effect is not visible in SPOT simulation.

The power deposited to ions and electrons in the two cases is shown in figure 4.8b. Considering the power deposited to ions (red lines), SPOT features a higher power deposited for $\rho < 0.9$. This difference can be explained by the different effective charge. In the core the difference is even more enhanced (reaching 40%). In the case of the power deposited to the electrons similar conclusions can be given.

The differences are anyway tolerable and could be more mitigated if using the same effective charge in the two different cases.

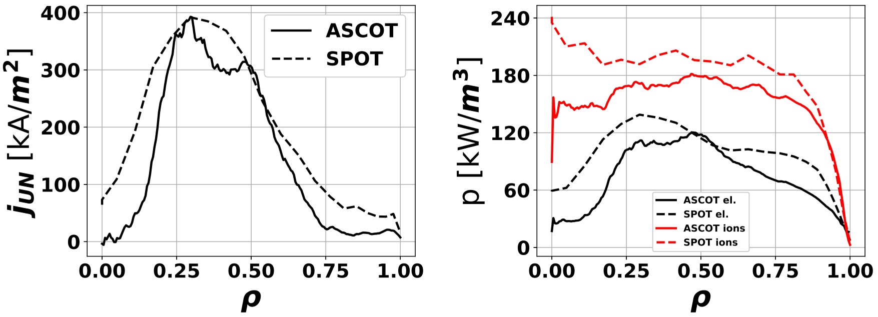

(A) Unshielded current in the two different cases

(B) Power deposited to electrons (black) and ions (red)

FIGURE 4.8: Comparison of slowing-down quantity computed by ASCOT (solid lines) and SPOT (dotted lines).

These benchmarks in both the beam attenuation and the slowed-down profiles are satisfying in terms of beam geometries and the difference in the beam geometries implemented in the two different codes should not impact on the plasma performance.

4.4 Reference scenarios

JT-60SA has a wide parameter space to analyze and to study, and wide objectives to pursue. The device operation is foreseen to be subdivided in different phases:

- **Initial research phase-I**: in this phase the commissioning of the device will be accomplished using H plasmas. The objective of operation scenario development in this phase is mainly on the definition of operation domain in various parameter spaces. This period will allow to assess the reliability of the diagnostic, to assess the stability of the control and real-time system, to study the wall conditioning using ECRF and boronisation. This phase will be ITER-relevant to assess the L-H transition and the H-mode with H plasma.

- **Initial research phase-II**: in this phase the base scenario for D operation will be assessed. This will prepare also the ground for controlled long-pulse operation. In this phase mainly three lines of research will be pursued: high-β_N scenario (advanced tokamak), high-β_P scenario (high current) and high-density operation. During this period the dominant electron-heating scenarios will be used, the advanced real-time control and the plasma response to actuators will be analysed.

- **Integrated research phase**: in this phase plasmas with 37 MW auxiliary power and long pulses will be achieved. Furthermore it will be useful to put the basis for the DEMO operational scenarios.

- **Extended research phase**: this period will be devoted to DEMO operational scenarios and to establish fully integrated operation in support to DEMO design.

The scenarios under case of study nowadays are related to initial research phase II and are listed in table 4.3. Density and temperature are volume-averaged.

	Full I_p, Inductive		Advanced tokamak	
	low density	high density	hybrid	full CD
Parameter	Scenario 2	Scenario 3	Scenario 4	Scenario 5
I_p (MA)	5.5	5.5	3.5	2.3
B_{tor} (T)	2.25	2.25	2.28	1.72
$\bar{n}_e$ ($10^{20}\,1/\mathrm{m}^3$)	0.56	0.9	0.62	0.46
n/n_G (%)	50	80	80	77
$\bar{T}_e$ (keV)	6.3	3.7	3.7	3.6
P_{PNB}, P_{NNB} (MW)	24,10	20,10	20 ,10	20,10
β_N (%)	3.1	2.6	3.0	3.6
f_{NI}(%)	0.5	0.36	0.58	1.0

TABLE 4.3: Parameters of JT-60SA reference scenarios

In this work, the impact of NBI EP on the reference scenarios listed above will be presented. The magnetic background of the simulation will be 2D. Profiles and magnetic equilibrium will be presented in the section devoted to each scenario.

4.5 Inductive scenarios

This scenario is the standard scenario that would directly contribute to ITER standard operation scenario, from ramp-up to ramp-down. The high confinement at high current will also provide an appropriate workhorse scenario for the operation at low collisionality and investigate plasmas close to the ITER collisionality. Also, He exhaust can be experimentally simulated using helium NB injection. Integrated modelling on this scenario has been studied in [71].

The magnetic field configuration is the same for both scenarios and it is shown in figure 4.9. In figure 4.10a the radial profiles of ion and electron density (and temperature) are shown. The plasma ion species are D and C.

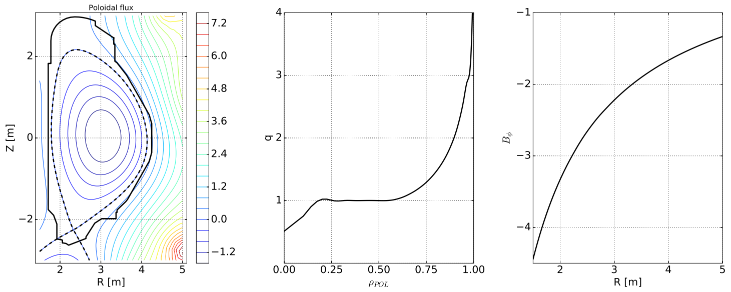

FIGURE 4.9: Magnetic configuration for full I_p reference scenario. Left: poloidal flux map, centre: safety factor profile, right: toroidal magnetic field profile

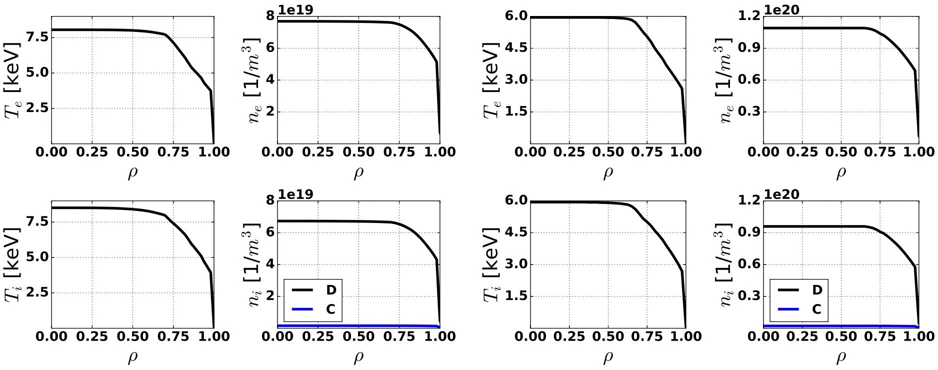

(A) Kinetic profiles for low density case (B) Kinetic profiles for high density case

FIGURE 4.10: Kinetic profiles for the two cases with full I_p

4.5.1 Low density - scenario 2

Ionisation

In this part the ionisation results for the low-density case ($n \sim 0.5\,n_G$) are shown. Figure 4.11 shows the fast ion ionisation profile (FIBP) split into the different NBs available for JT-60SA. It can be noted that the ions tend to be born mostly on the outer side of the plasma, and this is due to the contribution of P-NBs: blue curve represents the ionisation profile from tangential positive beams and, due to their trajectory, they cross the plasma mostly for higher values of ρ, thus they contribute strongly to the edge region of the FIBP. Perpendicular beams (green) contribute as well to this effect, but their trajectory allows a deeper penetration in the plasma, populating also regions with $\rho < 0.25$: in this region the contribution to the total FIBP is mostly given by PP-NBs.

The contribution of N-NBs (red) is smaller (with respect to positive beams) because of the difference in the injected beam current. In fact, the total injected current from the P-NBs is 385 A, while the total injected current from the N-NBs is 22 A. This justifies the difference in magnitude between the green curve and the rest. Due to its trajectory (figure 4.12), the contribution to the FIBP is peaked around $\rho \sim 0.3 - 0.6$.

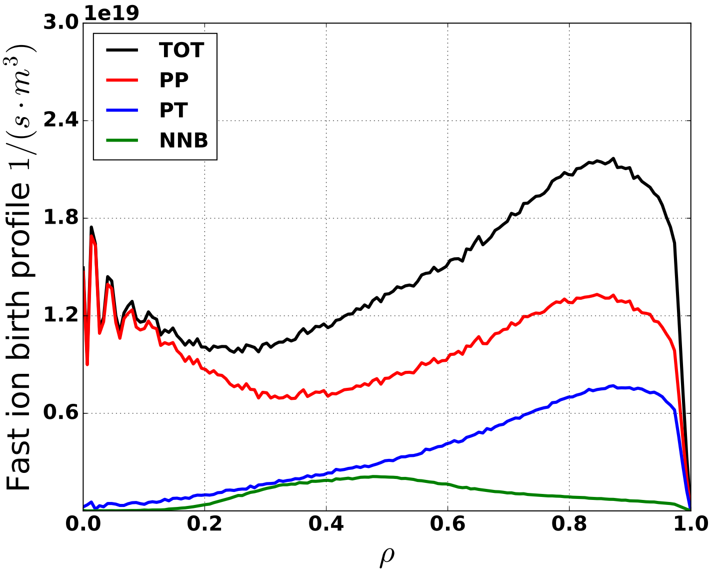

FIGURE 4.11: Fast ion birth profile for full I_p reference scenario, low density.

The un-ionised fraction of the beam (shine-through) is negligible for all the beams: it is below 0.2 % for each single beam. It reaches the maximum value (~12 kW) for the upper N-NBs. This is given by the high energy of the particles and the low-density area of the plasma the beam crosses. In figure 4.13 the collective ionisation map is shown (in absolute number of markers ionised) and the blue dots represent the markers hitting the wall. As can be noted, the contribution comes from the perpendicular P-NBs and the N-NBs. In any case, the total power deposited for shine-trough is negligible.

Particles first orbit

In this part, the focus will be given to the initial orbit of the particles: their topology (trapped orbits or passing orbits) and the losses, in fact the initial

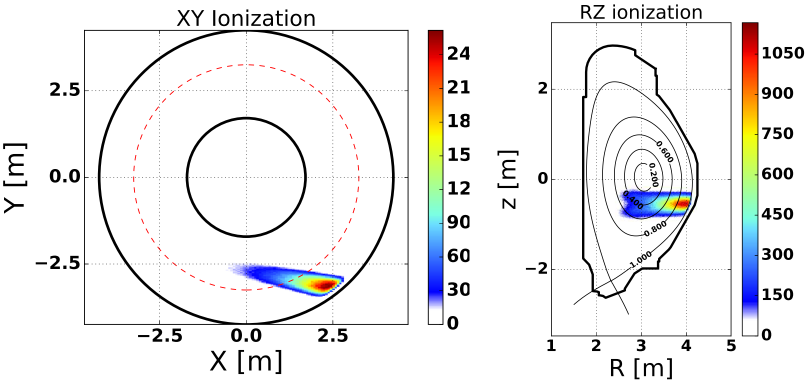

(A) Toroidal top view of NNB particle ionisation (red line is the magnetic axis)

(B) Poloidal projection of NNB particle ionisation

FIGURE 4.12: Ionisation of NNBs for low-density full I_p scenario. Colormap represents the number of markers

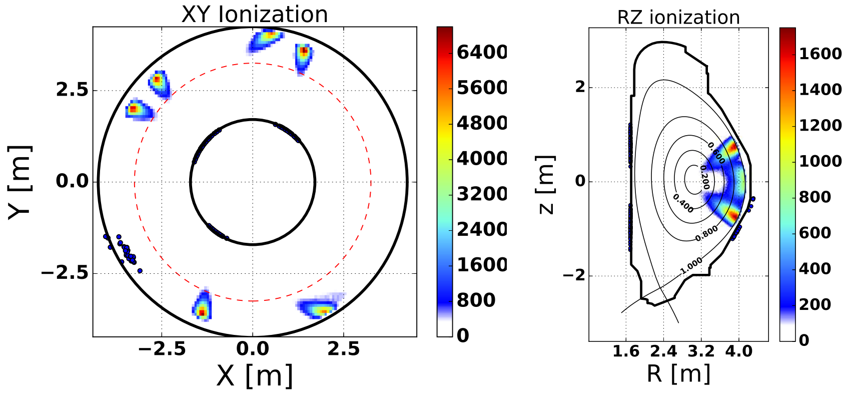

(A) Toroidal top view of particle ionisation (red line is the magnetic axis)

(B) Poloidal projection of particle ionisation

FIGURE 4.13: Ionisation of all the beams for low-density full I_p scenario. Colormap represents the number of markers

position and velocity (state) of the particles will induce prompt losses due to the unconfined trajectory the particles will follow.

In the case here analyzed, the losses come only from the counter-current P-NBs. The total amount of losses is around 450 kW, which is around 10 % of the power injected from the counter-current P-NBs, but only 1 % of the total injected power. The losses are shown in the unwrapped ϕ (toroidal angle) and θ (poloidal angle) on the wall, as shown in figure 4.14a. The actual losses for this case are shown in figure 4.14b. The colorbar represents the amount of markers in the bin. No wall load in kW/m^2 could be shown because there is no mesh with dimensions defined on the wall. Anyway, some different families of orbits can be recognised in the plot, and these are enhanced by the different color boxes.

In fact the different orbits depend on the initial state of the particles, which

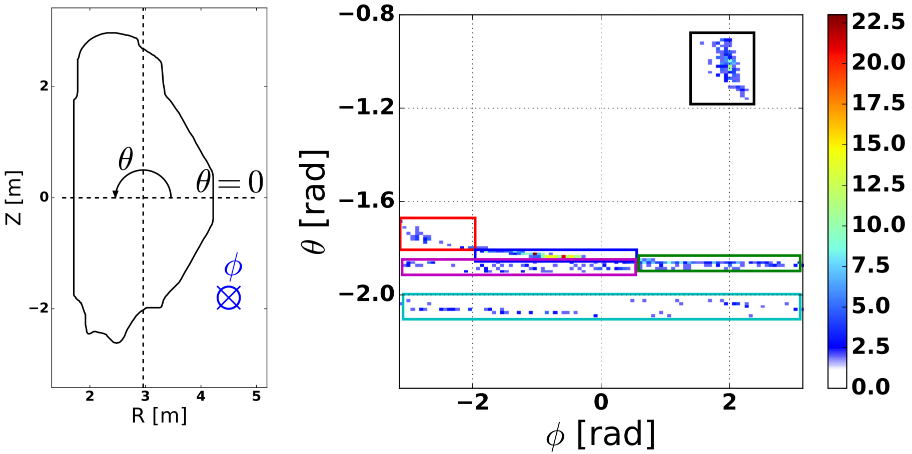

(A) Unwrapping of JT60-SA wall

(B) First-orbit losses on the wall.

FIGURE 4.14: JT60-SA losses to the wall

are shown in figure 4.15. The (ρ,ξ) image shows that the inner the particles go (i.e. the lower is the value of ρ), the lower is the value of initial pitch they assume because of the change in the magnetic field configuration with ρ.

The black markers are the ones whose trajectory is quite far from the X-point, but still the banana orbit makes them collide with the wall at relatively high values of θ ($> -1.2\,\mathrm{rad}$). The other particles are influences by the presence of the x-point and they follow the field lines up to the strike points.

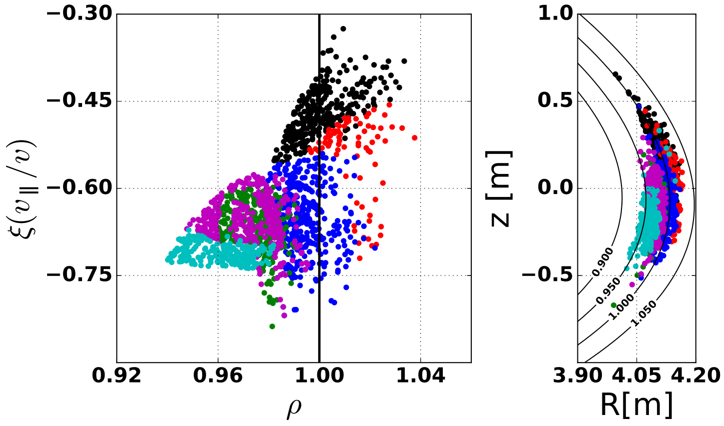

FIGURE 4.15: Initial position of the lost particles in (ρ,ξ) and (R, Z) spaces

Lastly, in figure 4.16 the fraction of trapped and passing initial orbits is shown. As can be noted, the amount of trapped orbits decreases with energy, because at higher energy corresponds higher penetration of the particles, thus making the initial orbit to be passing. Considering the N-NB, the amount of trapped initial orbits is close to 40% but none of them are in orbits colliding with the wall

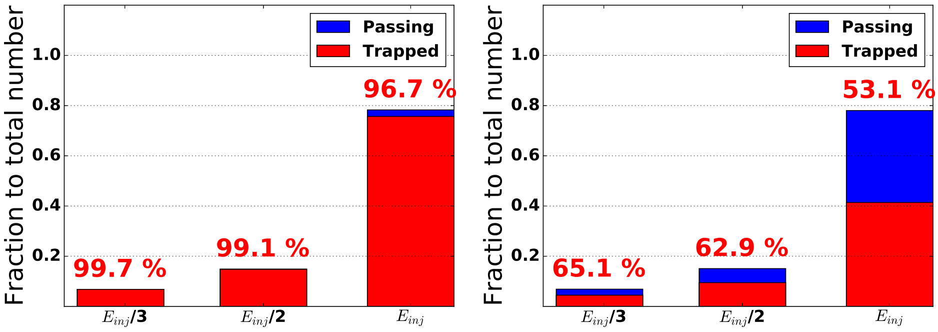

(A) Perpendicular positive beams (B) Tangential positive beams

FIGURE 4.16: Trapped fraction for positive beams

Deposition of particles, current and power

The radial profiles describing how the beam power is deposited in the plasma are shown in figure 4.17. Power deposition to the electrons (figure 4.17a) comes mostly from the negative beams, due to the high energy those particles have. Around $\rho = 0.4$ the beam particles are mostly ionised, and this justifies the high power density peak shown. Around $\rho = 0.8$ the N-NB power deposition shows a plateau which is given by the trapped particles, which born mostly around that position. Deposition on the edge ($\rho > 0.9$) is dominated by positive beams, where they deposit most of their particles (but N-NBs do not). A totally different trend is shown in figure 4.17b, where P-NBs dominate the power deposition to ion, because of their energy. The power deposition given by low-energy particles is mostly at the edge (location where tangential P-NBs EP live) and the perpendicular beam contribution is clear in the core, location where they manage to penetrate. Nevertheless, the contribution to ion heating by N-NBs only is comparable to the one given to electrons.

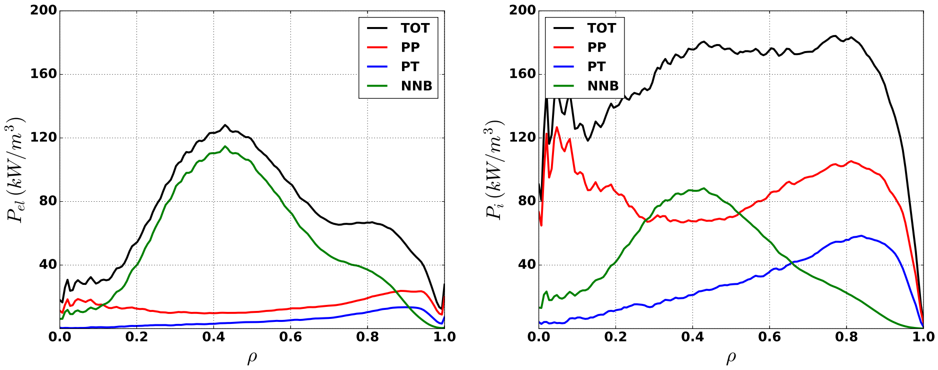

(A) Power density profile deposited to electrons (B) Power density profile deposited to bulk ions

FIGURE 4.17: Power density coming from NBI

The EP contribution to pressure is given, as expected, mostly by N-NBs particles (figure 4.18a). Lastly, the contribution to current is given in practice only by the N-NBs (figure 4.18b). The contribution of the tangential positive beams sums out because of their co- and counter- current injection geometry.

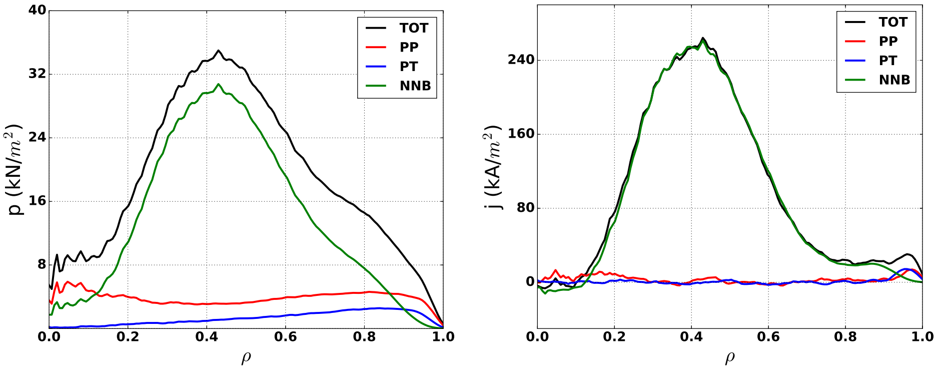

(A) Pressure profile (B) Current density profile

FIGURE 4.18: Pressure and current density profile from EP.

In table 4.4 the integrated quantities are shown. The induced current reaches 8% of the total current and the power lost is around 2%. The total power in the table includes also the thermalised component. In square brackets the fraction of total power to the single components is given. The majority of the power is given to bulk ions and some 10% gets deposited to C impurity. The efficiency of the system is $\eta = 0.1 \times 10^{20}$ A/Wm^2.

I_p (kA)	P_e (MW) [%]	P_i^D (MW) [%]	P_i^C (MW) [%]	P_{tot} (MW)
470 [8%]	8.23 [24%]	19.2 [58%]	2.92 [9%]	33.2

TABLE 4.4: Integrated quantities for Full-I_p scenario, low density

The potentiality of the codes in use allows to study the 2D distribution of the particles. The most interesting are the particles injected by the N-NBs, which are shown here. In figure 4.19a the density of the fast particles is shown in the RZ space. It can be noted the concentration of the particles around the injection location ($\rho \sim 0.4$).

The distribution of the fast particles in the (ξ, E) space is shown in figure 4.19b. The injection energy is 500 keV, which is where the particles born but not the most populated region. This can be explained by the fact that the pitch angle scattering (i.e. collisions with ions) bring the particles up to the 'border' ($\xi = 1$): in this place, the only thing that can happen is that the particle bounces back in the x-axis (so ξ starts decreasing). Multiplying this effect for all the particles, the region which becomes more populated is around $\xi > 0.9$ and 150 keV< E < 350 keV.

The critical energy is around 160 keV for this case. Below this point the pitch-scattering collisions dominate, making the distribution more uniform in the x-direction, reducing the 'border' effect.

The slowing-down time of the P-NBs (N-NBs) EP is 80 ms (300 ms).

Nonetheless, the population with negative ξ at the injection energy confirms the initial orbits of the particles, which split among the trapped and passing configuration.

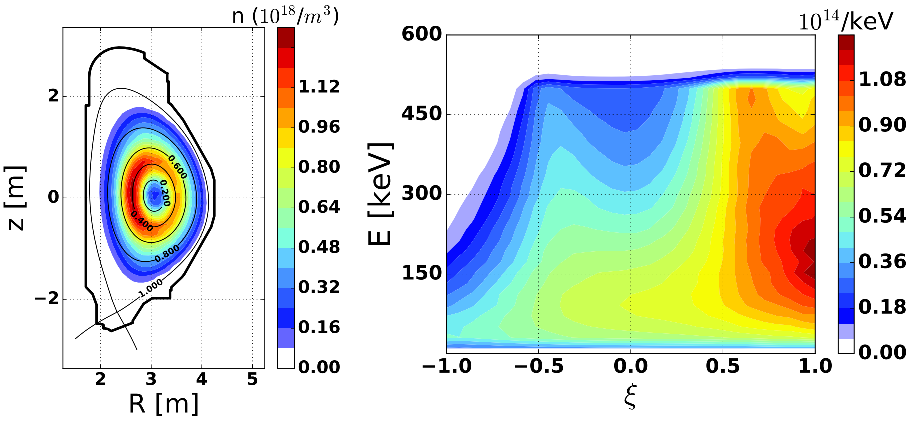

(A) Configuration space (R,Z)

(B) Configuration space (ξ,E)

FIGURE 4.19: 2D steady-state distribution function for scenario 2

4.5.2 High density - scenario 3

Ionisation

Increasing the density ($n \sim 0.9\, n_G$), the penetration of EP decreases significantly. In fact, the FIBP in figure 4.20 shows a strong decrease in the quantity of ions borning in the inner part of the plasma: for the low-density case (figure 4.11), the perpendicular beams had a stronger penetration in the plasma core. The lower contribution on the tangential P-NBs is given by the lower power injected in this scenario, which foresees the counter-injected P-NBs to be shut down.

The shine-through fraction is even lower than low-density case. Furthermore, the first orbit losses are negligible in this case because the counter-injected particles are not present.

A higher particle deposition in the outer side of the plasma results also in a higher fraction of trapped particles. For instance, the third-energy component of the perpendicular P-NBs reaches the 100% of the ionisation in the banana-orbit regime. The N-NBs the trapped fraction increases to >50%, and this happens because particles initial position is closer to the edge, as figure 4.21 shows for the trapped particles for NNB. In the plot, the ρ initial state of the particles in trapped orbits is shown. It can be noted that the particles in trapped orbits born only for $\rho \gtrsim 0.55$ and for scenario 3 there are more particles ionized there with respect to scenario 2, resulting in a higher amount of trapped particles at the starting energy (500 keV).

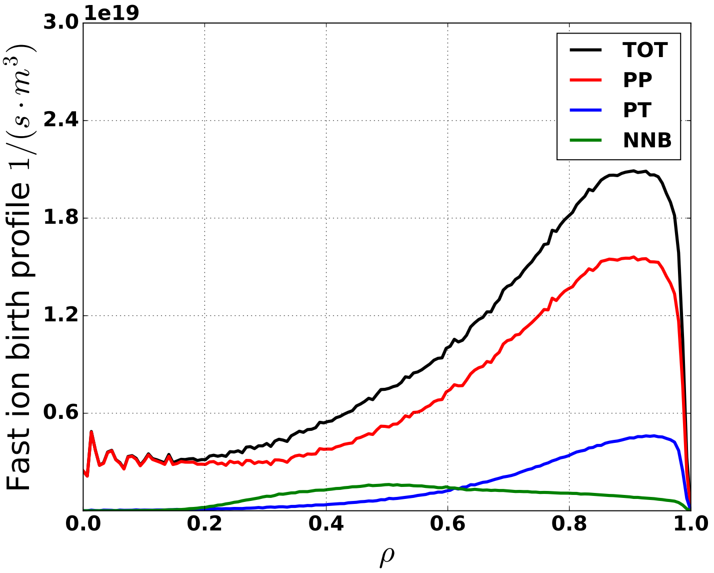

FIGURE 4.20: Fast ion birth profile for full I_p reference scenario, high density.

Deposition of particles, current and power

The results shown in this section confirms the impact of the density and temperature profiles on the power and current deposition. The deposited power is still high, with low amount of losses, but the relative amount of power to electrons is slightly higher with respect to low density case (see table 4.5) and this is given by the decrease in temperature, which makes the critical energy lower.

With respect to low-density case, the deposited power (figure 4.22) tends to be higher on the outer part of the plasma. The profiles shown in figure 4.23 are half of the same profiles for low-density case, and this is given mostly by the higher rate of collisions the EP have: this implies that their slowing-down time is lower so they lose their energy faster. In this case, the slowing-down time of the P-NBs (N-NBs) EP is 50 ms (200 ms), which is 30% less than the previous case. The current efficiency is lower in this case $\eta = 0.05 \times 10^{20}$ A/Wm^2.

I_p (kA)	P_e (MW) [%]	P_i^D (MW) [%]	P_i^C (MW) [%]	P_{tot} (MW)
204 [3%]	9.94 [33%]	15.8 [53%]	2.36 [8%]	29.8

TABLE 4.5: Integrated quantities for Full-I_p scenario, high density

The difference in the slowing-down times and plasma critical energy is also evident in the space and (E,ξ) 2D functions. In fact, the RZ density (4.24a) is roughly half the previous case. The (E,ξ) distribution function shape (figure 4.24b) changes as well: the low-energy region is much more populated. The border effect is weaker and visible only at lower energies.

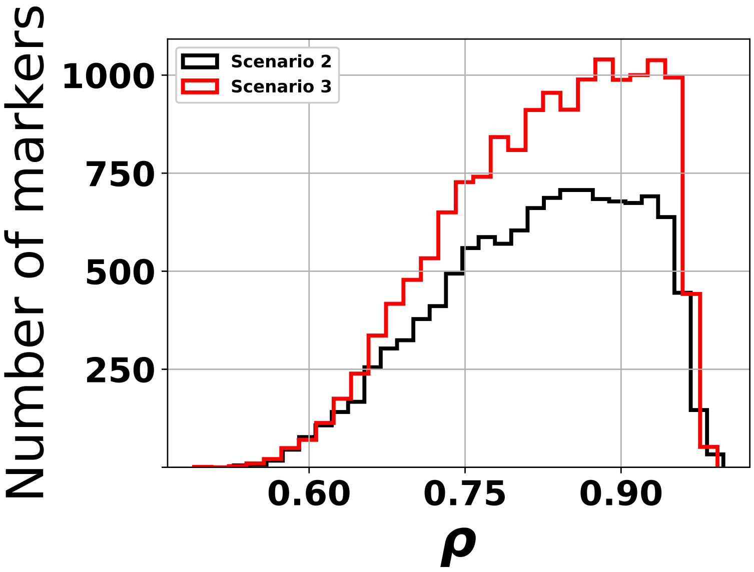

FIGURE 4.21: Initial ρ position for NNB-injected particles in trapped orbits in the case of scenario 2 (black) and scenario 3 (red)

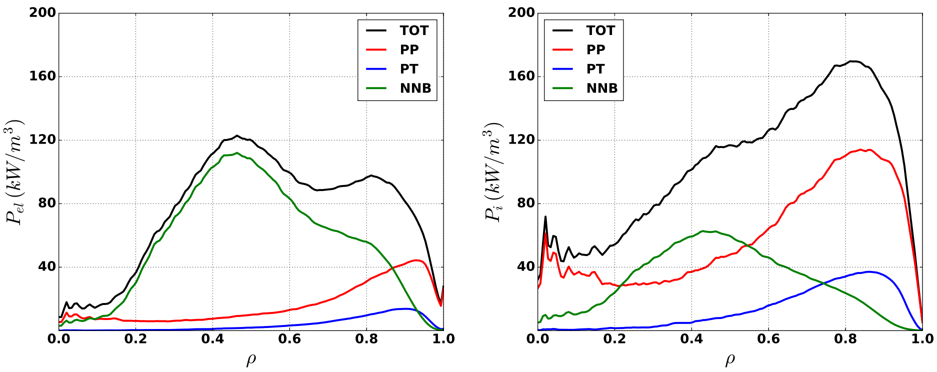

(A) Power density profile deposited to electrons

(B) Power density profile deposited to bulk ions

FIGURE 4.22: Power density coming from NBI

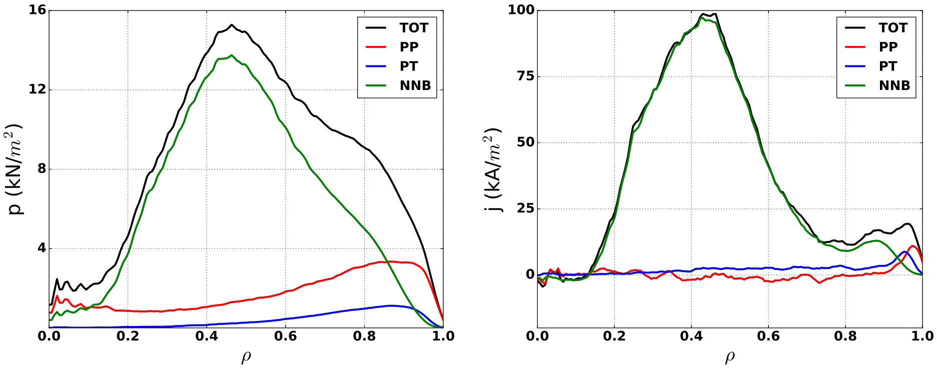

(A) Pressure profile

(B) Current density profile

FIGURE 4.23: Pressure and current density profile from EP.

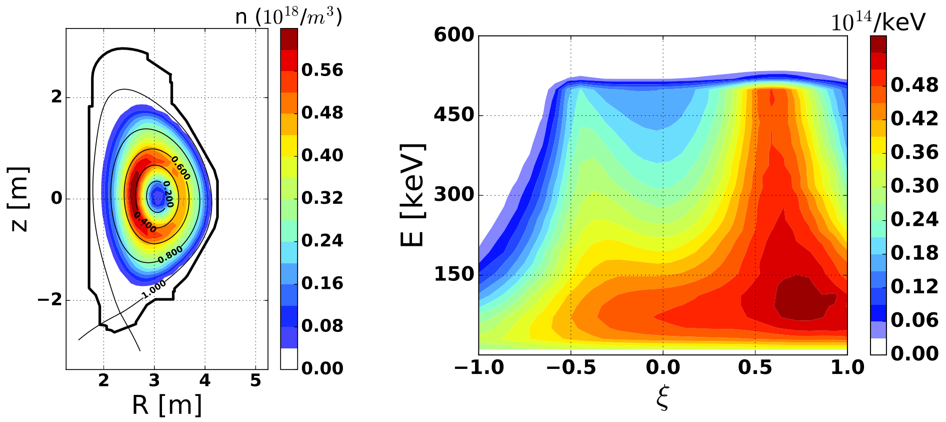

(A) Configuration space (R,z)

(B) Configuration space (ξ,E)

FIGURE 4.24: 2D steady-state distribution function for scenario 3

4.6 Advanced tokamak scenarios

JT-60SA will continue study advanced tokamak scenarios [41] during initial research phase as JT-60U was used to do [74]. This will be useful for ITER [75] [42] and DEMO [76] advanced tokamak operation.

In JT-60SA the off-axis driven current given by the N-NBs can enhance and sustain the reversal of the q-profile in addition to the bootstrap current. In the simulations carried out for these scenarios the couter-injected P-NBs are turned off.

In this section the two advanced scenarios foreseen for JT-60 SA are studied:

- 'hybrid' - scenario 4: in this case, the total current should be driven 50% non inductively, in order to guarantee a long pulse operation. This scenario is also called 'improved H-mode' because it has and H-factor greater than one so it is promising (for ITER) for a high neutron fluency. For this regime, the q value would be in the range 1.0-1.5 with shear close to 0.0. This slightly raised value of q in the core would avoid the sawtooth activity, which could trigger neoclassical tearing modes in standard H-mode plasmas.

- steady-state - scenario 5: the current in this case will be fully generated non-inductively (bootstrap contribution $\sim$ 50%). This requires a high β_N (>4) , which will destabilise MHD instabilities such as resistive wall modes. The q-profile in this case would be strongly reversed

4.6.1 Hybrid scenario

The input for hybrid scenario are shown in figure 4.25 and 4.26. The on-axis values are similar to full-inductive low density case (figure 4.10a), but the shape is quite different due to the presence of the ITB and a different pedestal height.

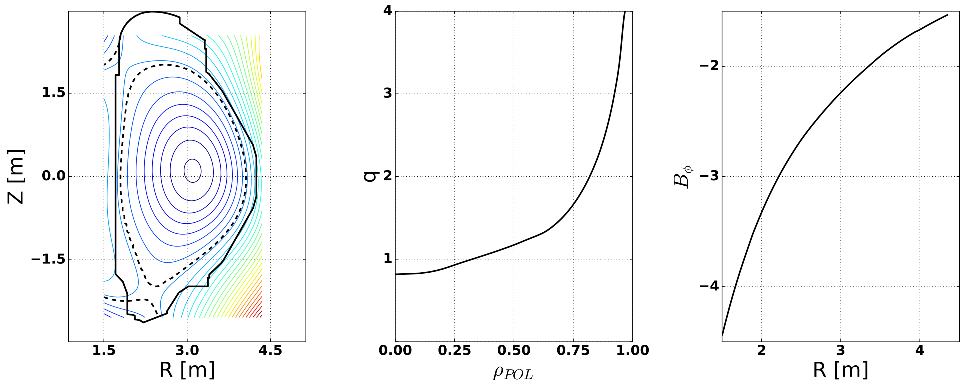

FIGURE 4.25: Magnetic field for hybrid scenario

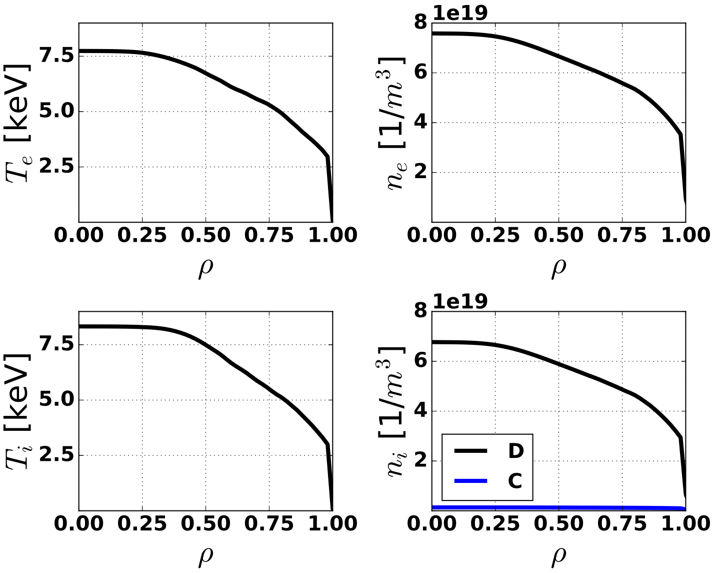

FIGURE 4.26: Kinetic profiles for hybrid scenario

Ionisation

The fast ion birth profile is shown in figure 4.27. The P-NBs EP have a good penetration in the plasma, up to the magnetic axis, providing a more uniform source of fast ions all over the plasma radius with respect to inductive cases. The shine-through remains still negligible. In this case, the fraction of EP NNBs population in passing regime is close to 80%, while the positive parallel beams produce around 35% of trapped particles. The perpendicular

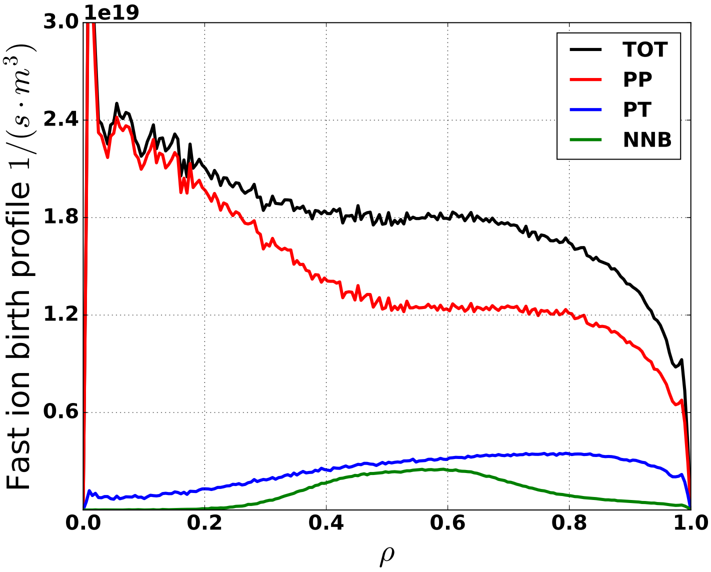

FIGURE 4.27: Fast ion birth profile for scenario 4

beams still maintain a high fraction of trapped particles, which in this case reaches 94%.

Deposition of power, current and particles

The power deposition to electrons (figure 4.28a) is still dominated by N-NBs but the edge increase given by trapped particles is not so evident as it was in previous cases. The different born position of the particles make the power deposition profiles to ion (figure 4.28b) much wider, having the higher deposition for $\rho < 0.6$. Around 30% of the power is deposited to electrons (table 4.6).

I_p (kA) [%]	P_e (MW) [%]	P_i^D (MW) [%]	P_i^C (MW) [%]	P_{tot} (MW)
740 [20%]	8.7 [29%]	16.5 [56%]	2.36 [8%]	29.55

TABLE 4.6: Integrated quantities for AT hybrid scenario

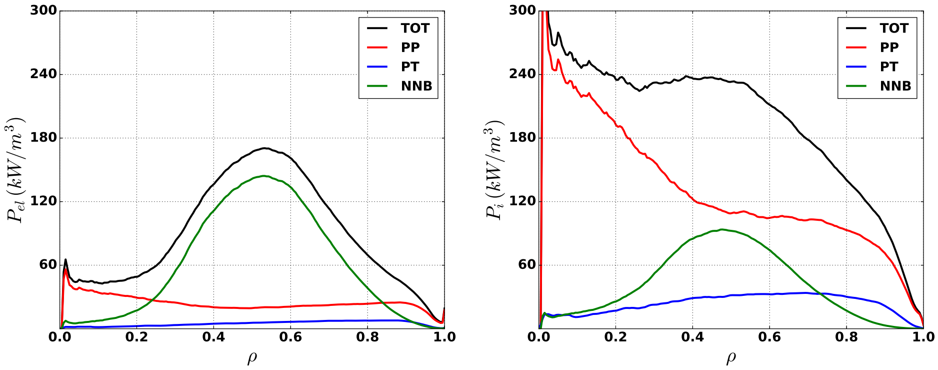

(A) Power density profile deposited to electrons

(B) Power density profile deposited to bulk ions

FIGURE 4.28: Power density coming from NBI

The EPs pressure and current (figure 4.29) are, as usual, dominated by the most energetic particles. Not that the EP pressure is higher than non-inductive cases. The total induced current by N-NBs is around 20% of the total current (740 kA), which is almost half of the requested non-inductive current.

Considering the 2D distribution function of the N-NBs EP, in figure 4.30a the hollow density profile is presented, as well as it was in the previous cases. The (ξ,E) distribution is highly populated for the highest value of pitch, denoting a low pitch diffusion: the critical energy is 90 keV, thus energy-scattering collisions dominate. In this case, the slowing-down time for 500 keV particles is 400 ms, higher than the full-I_p cases.

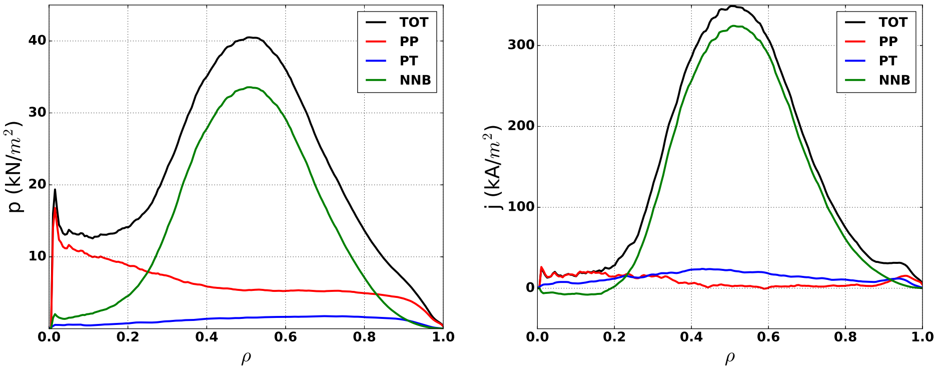

(A) Pressure profile

(B) Current density profile

FIGURE 4.29: Pressure and current density profile from EP.

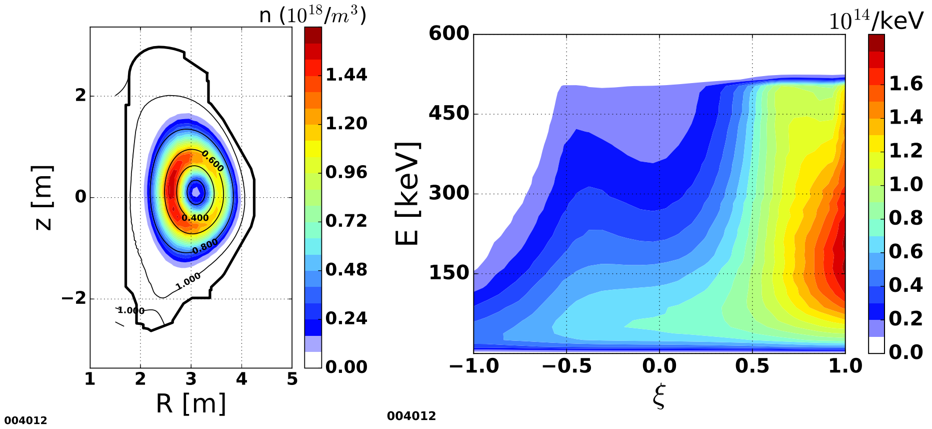

(A) Configuration space (R,z)

(B) Configuration space (ξ,E)

FIGURE 4.30: 2D steady-state distribution function for scenario 3

4.6.2 High-β_N, full CD - scenario 5

The last scenario studied in this work for JT-60SA is the advanced tokamak, high β_N full current-drive [77] [78]. In this case, the totality of the current is non-inductively driven, with 50% of bootstrap. In figure 4.31 the strong reverse shear of the configuration can be seen: the on-axis q profile is close to 4 while the minimum ($1 < q_{min} < 2$) lies around $\rho = 0.5$. This configuration relies strongly on the ITB, which lies close to the minimum of q, as figure 4.32 shows.

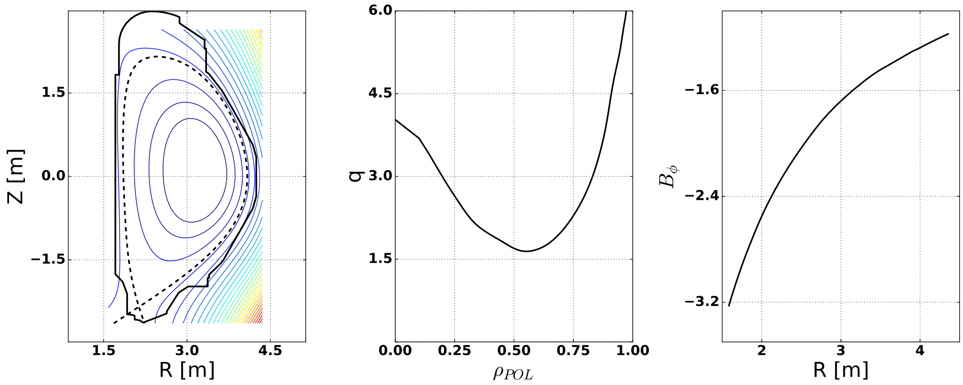

FIGURE 4.31: Magnetic field for full CD scenario

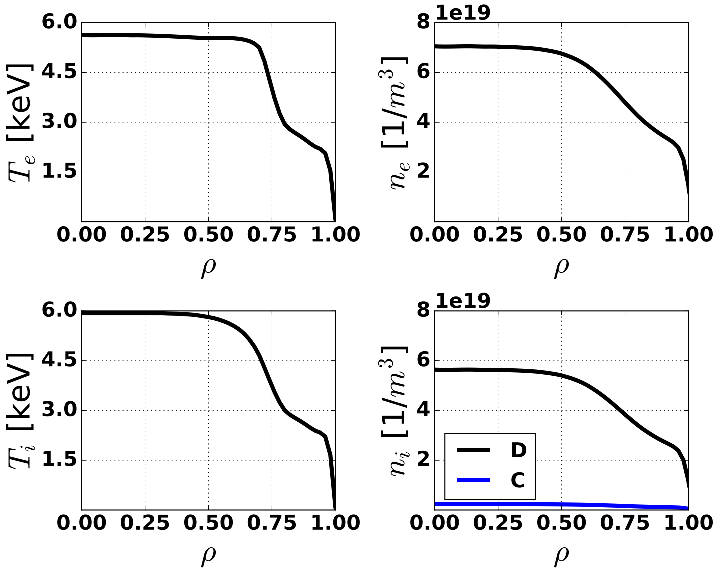

FIGURE 4.32: Kinetic profiles for full CD scenario

Ionisation

The fast ion birth profile (figure 4.33) generates most of the particles around the ITB. The NNBs ionisation is dominant at locations slightly inner than the minimum q. In this scenario, the majority of the N-NBs EP is generated in passing orbits (for the 90%). For the P-NBs the fraction of particles born on trapped orbits is reduced as well: it is 23% for tangential beams and 88% for the perpendicular beams.

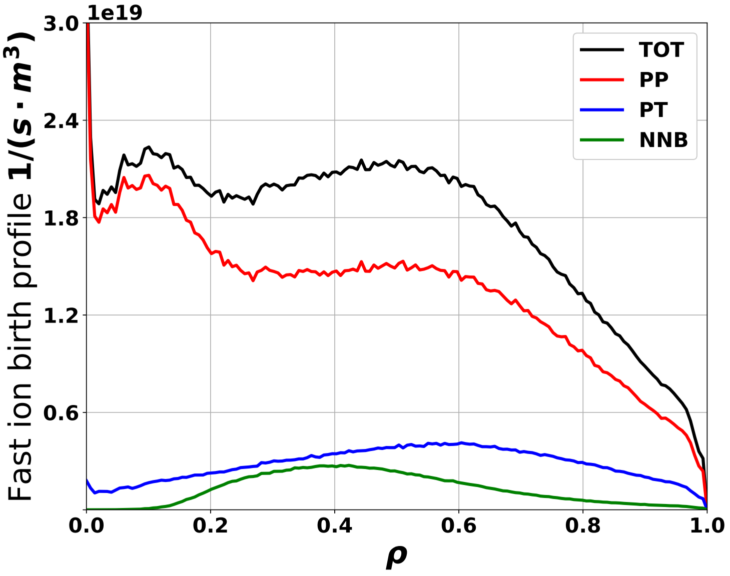

FIGURE 4.33: Fast ion birth profile for scenario 5

Deposition of power, current and particles

I_p (kA) [%]	P_e (MW) [%]	P_i^D (MW) [%]	P_i^C (MW) [%]	P_{tot} (MW)
758 [33%]	9.7 [33%]	14.6 [49%]	3.57 [12%]	29.8

TABLE 4.7: Integrated quantities for AT fully non-inductive scenario

In figure 4.34 the power deposition to bulk plasma is shown, confirming a deposition inside the ITB, providing mostly central heating. The power deposition coming from N-NBs is non-zero even in the plasma axis, due to the magnetic configuration of the plasma. The efficiency is lower in this case (0.03×10^{20} A/Wm^2) because of the lower plasma density.

The pressure profile (figure 4.35a) is peaked around $\rho = 0.4$ and the current profile (figure 4.35b) is peaked in the same position, confirming that the (N-NBs) particle live most of their time there, driving 30% of the current (750 kA) where the q-profile is desired to be reversed and increasing the pressure (i.e. the β) where the transport barrier is desired.

Looking more in detail at the N-NBs EP density (figure 4.36a), it is confirmed that the particles live around $\rho = 0.3 - 0.4$ but their profile seems to be broader with respect to hybrid scenario. In figure 4.36b the diffusion of the particles in (E, ξ) space is similar to the hybrid case, having a lower trapped fraction population at higher energies. In this case the critical energy is around 70 keV and the slowing-down time of the particles is 300 ms, which is lower than the hybrid case. A lower slowing-down time means that the

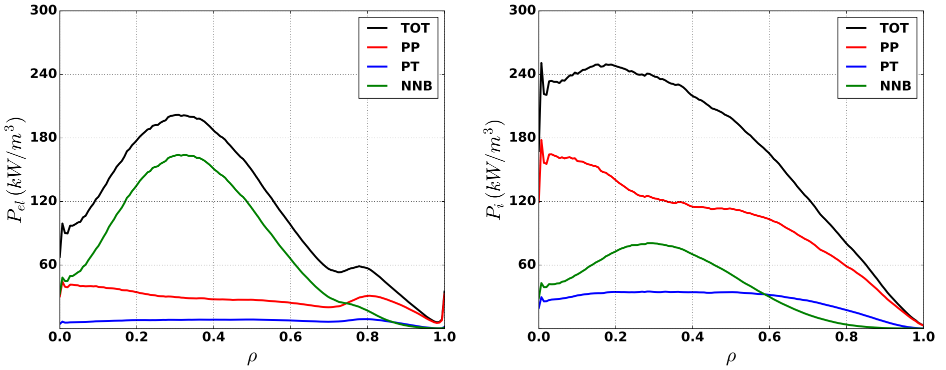

(A) Power density profile deposited to electrons (B) Power density profile deposited to bulk ions

FIGURE 4.34: Power density from NBI

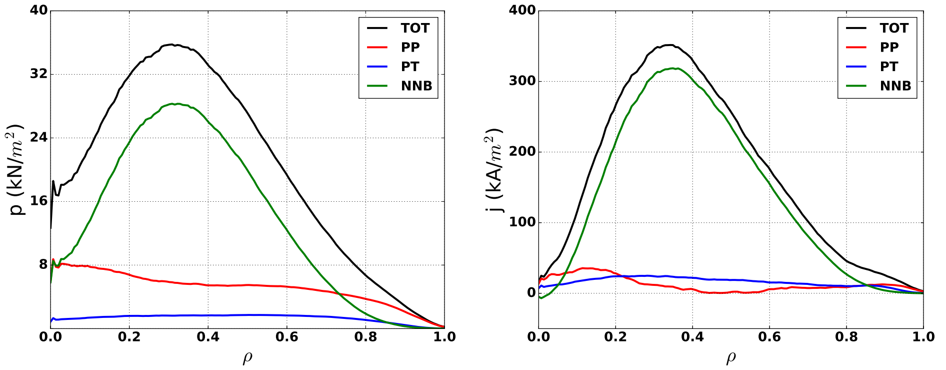

(A) Pressure profile (B) Current density profile

FIGURE 4.35: Pressure and current density profile from EP.

particles remain lower time in the plasma, thus the current drive (and the efficiency) are reduced with respect to previous case.

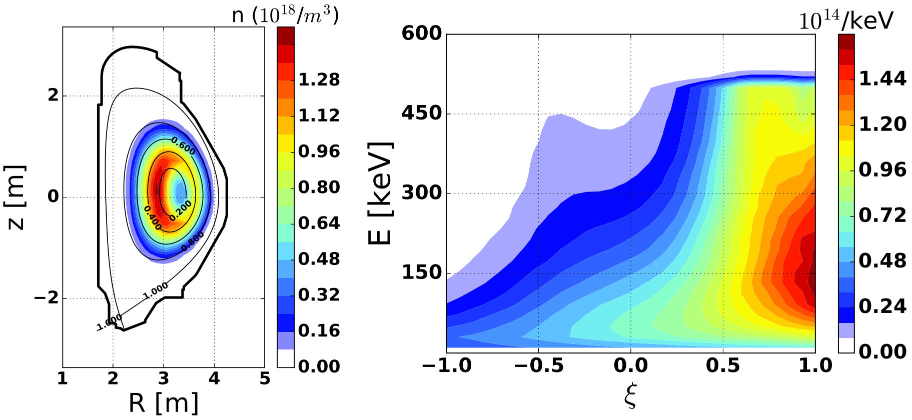

(A) Configuration space (R,z)

(B) Configuration space (ξ,E)

FIGURE 4.36: 2D steady-state distribution function for scenario 5

4.7 Banana width in the different scenarios

The width of the trapped orbit the particles are confined in can vary a lot among the different plasma configurations. In this case, the variations are induced both by the initial state of the particles and the different magnetic fields produced in the plasma. Exploring conventional scenarios and fully non-inductive scenarios means exploring different magnetic field, thus banana widths. These values are explored here for the different beams (positive tangential, positive perpendicular and negative beams).

The histograms showing the initial banana widths for the particles in trapped orbits are shown in figure 4.37 for the positive beams. It was necessary to split the two different configurations (perpendicular in figure 4.37a and tangential in figure 4.37b) because of the different ionization position of the markers (i.e. different magnetic field) and different parallel velocity. In the case of perpendicular beams, the orbits are usually smaller than 5 cm. This accumulation at low widths is given by the fact that the parallel velocity is close to zero. The difference for scenario 2 and 3 is small (they have the same magnetic field), while for advanced scenarios the trapped orbits tend to be larger (with respect to inductive cases) because of the lower value of the poloidal magnetic field.

In the case of the tangential beams, the orbits tend to be larger because of the larger parallel velocity. In this case it is even possible to distinguish three different peaks, corresponding to the three particle energies. In an analogue way to perpendicular beams, banana orbits tend to be wider for non-inductive cases and can get up to 9 cm, which is $\sim$ 10% of the minor radius.

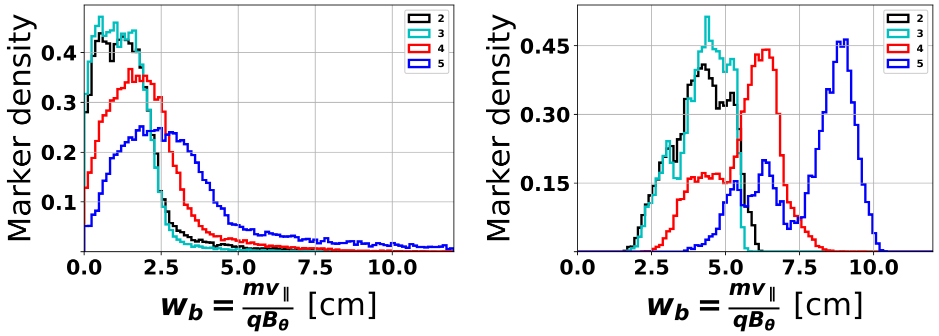

(A) Histogram for positive beams, perpendicular injection (B) Histogram for positive beams, tangential injection

FIGURE 4.37: Histograms with orbit width of the positive beam markers in the different scenarios: 2 (black), 3(light blue), 4 (red), 5(blue)

The picture is significantly different for negative neutral beams, which have $\sim$ 6 times the energy of the positive beams and they have most of the velocity in the parallel direction. The larger banana widths can be seen in figure 4.38, and the minimum of the orbits is 8 cm for the inductive cases. The average width increases by 50% for the hybrid scenario (with respect to hybrid cases) while it doubles for the fully non-inductive scenarios, reaching more than 20 cm (i.e. 20% of the minor radius). This effect is in agreement with the same trend seen for positive beam cases, and in the same order of magnitude even if the ionization position of the negative beams is close to $\rho \sim 0.4$.

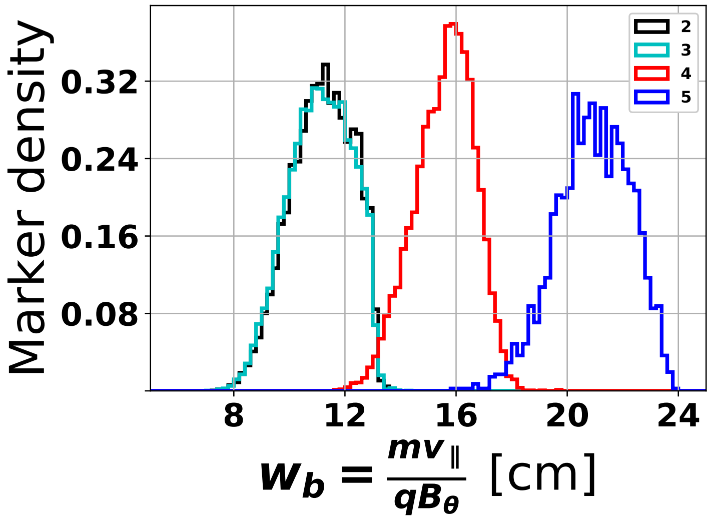

FIGURE 4.38: Histograms with orbit width of the negative beam markers in the different scenarios: 2 (black), 3(light blue), 4 (red), 5(blue)

4.8 Impact of Z_{eff} on NBI in JT-60SA

Plasma composition impacts on NBI because of the different collision cross-sections. In JT-60SA reference cases, we assumed the bulk ions in the plasma are D, with C considered as the main impurity.

With a D,C plasma, the value of Z_{eff} gives the value of the two ion densities assuming quasi-neutrality, as equation 4.1 resumes:

$$\begin{cases} Z_{eff} = \frac{\sum(n_i \cdot Z_i^2)}{\sum(n_i \cdot Z_i)} \\ n_e = n_D + 6 \times n_C \end{cases} \Rightarrow \begin{cases} n_D(\rho) = n_e(\rho)\frac{6-Z_{eff}(\rho)}{5} \\ n_C(\rho) = n_e(\rho)\frac{Z_{eff}(\rho)-1}{30} \end{cases} \tag{4.1}$$

In particular, for scenario 5 the Z_{eff} profile was assumed to be flat with a constant value of 2. In this section, some different Z_{eff} profiles will be assumed for this scenario, in order to infer the impact of different impurity content on NBI. These profiles are not self-consistent with the integrated modelling (changing the impurity content will change as well the resistivity of the plasma, for example) but this scan would give an idea of the importance of Z_{eff} for the NBI power and current deposition. The profiles of Z_{eff} and the resulting n_C for scenario 5 are shown in figure 4.39. The profiles have been chosen assuming two ideal opposite cases, but keeping the volume-averaged value of Z_{eff} constant to 2. The first case (accumulation) assumes that the impurity clusters in the plasma core. The second one (edge) assumes that the impurity confinement is so low that these particles remain confined to the edge.

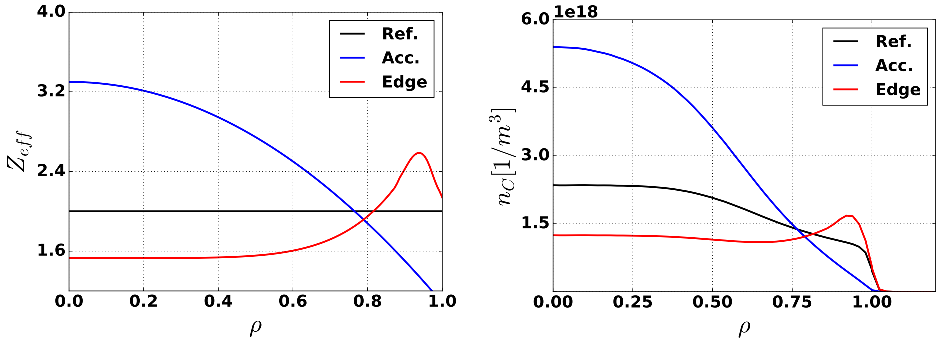

(A) Z_{eff} profiles (B) n_C profiles

FIGURE 4.39: Impurity content input for the scan. Black line is the reference case (constant Z_{EFF} over radius), blue line refers to the case considering impurity accumulation in the core, red line refers to the case considering edge accumulation of the impurities.

The fast ion birth profile is shown in figure 4.40. The profiles are not so different between each other, even if with a non-flat profile the ions seem to born preferentially outwards instead of borning in the core.

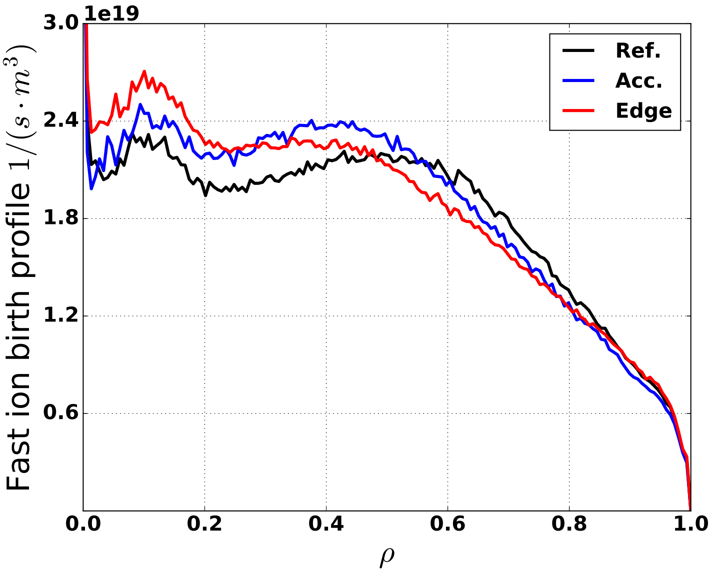

FIGURE 4.40: Fast ion birth profile at different Z_{eff}

Much stronger differences can be seen with the slowing-down quantities, in particular the power density deposition profiles (figure 4.41). Only the deposition to ions are shown since the power deposition to electrons showed no significant difference. The power deposited to ions get split in a different way, because of the different densities. The higher is the C density, the higher fraction of power it gets.

In the case with core accumulation of impurities, C can absorb up to 21% of the injected power (reducing the power absorbed by D), while with edge accumulation the power deposited to D ions is increased.

	P_D (MW)	P_C (MW)	P_C/P_{tot} (%)	I_p (kA)
Reference	14.5	3.5	13	760
Accumulation	12.15	5.9	21	776
Edge	15.2	2.3	8.4	765

TABLE 4.8: Integrated NBI deposited quantities

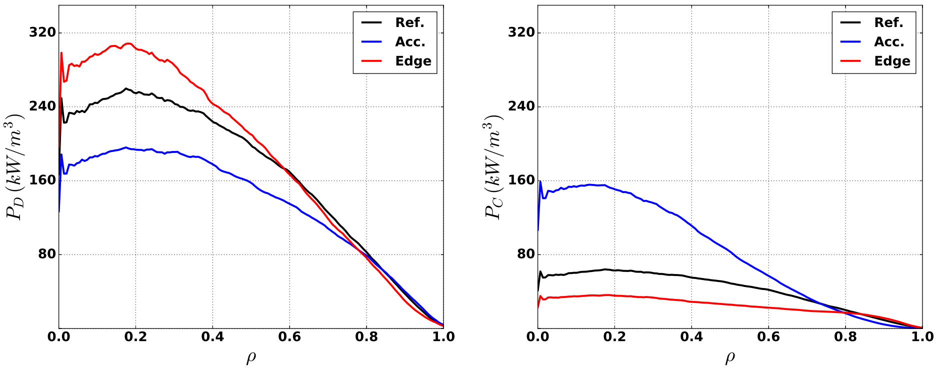

(A) Power density profile deposited to bulk ions (B) Power density profile deposited to main impurity

FIGURE 4.41: Power density from NBI to plasma ions

The different impurity content doesn't impact much on the fast ions in the plasma, as figure 4.42 shows. In fact, the EP density remains quite similar in the three different cases. The driven current has a different profile shape, which can be done to the different shielding given by the electron back-stream current, but the integrated value is quite similar to the reference case.

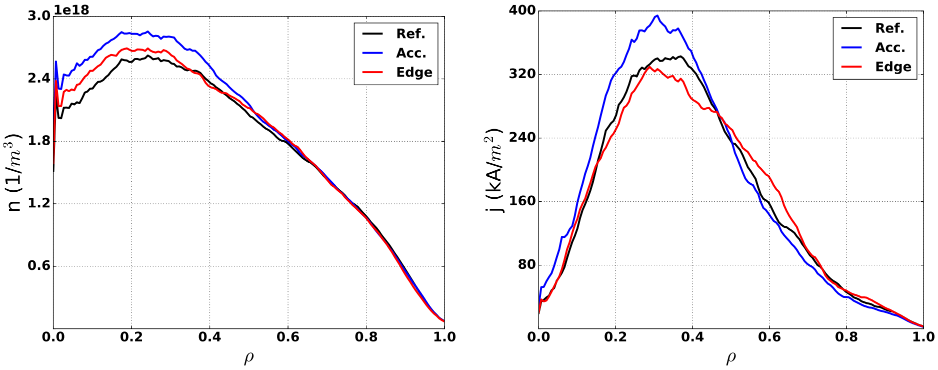

(A) Pressure profile (B) Current density profile

FIGURE 4.42: Pressure and current density profile from EP.

4.9 N-NBs energy scan on advanced fully-CD scenarios

In this chapter, the stress on the importance of neutral beams for JT-60SA has been given. The design reference scenario with full power and full energy will not be the first scenario to develop, but some other inter-step are needed for experimental reasons, both for technical prudence and scenario physics understanding. In this section, the limit on the N-NBs energy will be studied, in order to understand the capability driving current in the plasma also at lower energies. In the cases here studied, the power is limited accordingly to the perveance law expressed in equation2.1. This study will also provide the distribution functions to be fed to codes capable of studying the excitation of Alfvén waves.

Only the N-NBs energy will be varied and the three energies chosen for this study are 500 keV,350 keV and250 keV, which correspond respectively to 100%, 80% and 70% of the maximum achievable particle velocity.

At lower energies, the penetration depth decreases because of the increase in the cross-section $\sigma \sim 1/\sqrt{E}$. This is evident by looking at the FIBP for the three energies considered (figure 4.43a). In fact, the peak around $\rho \sim 0.4$ decreases strongly by reducing the energy. The total EP influx (i.e. the integral) decreases because of the power reduction.

In figure 4.43b the relevant scalars for NBI are shown. Reducing the EP energy, the power deposition becomes dominant to the ions (G_i increases from 0.35 to 0.55) thus we get further from the conditions of dominant electron heating. Most detrimental for the sustainement of the advanced scenario, the efficiency of the current drive decreases with decreasing power (figure 4.43b). This is given by a strong decrease in the confinement time of the EP, which reduces the circulating time of the particles. No significant changes in the shape of the profiles can be seen, only a reduction in their magnitude. This means that the spatial diffusion is not affected by different EP energy.

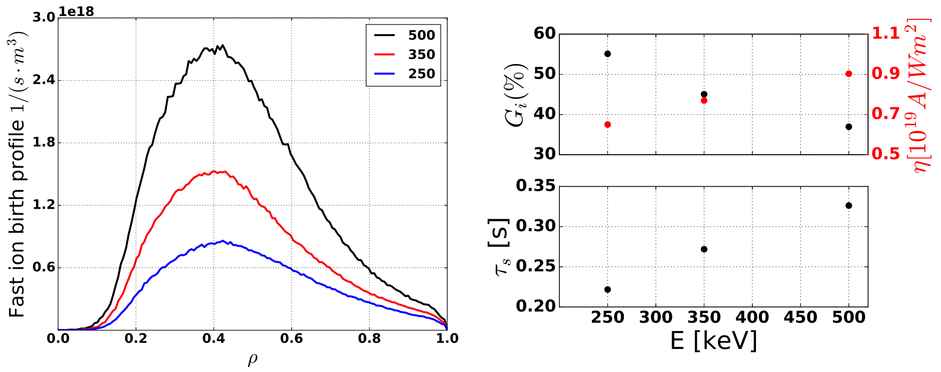

(A) FIBP profile at different energies.

(B) Scalars for the different energies

FIGURE 4.43: NBI deposition at different N-NB energies

4.10 Conclusion

In this chapter, predictive simulations on JT-60SA reference scenarios with ASCOT code have been presented. JT-60SA is a superconducting machine which relies on a wide set of neutral beams to reach reactor-relevant plasma conditions, such as dominant electron heating and fully current-driven advanced tokamak scenarios. These particular plasma features are important for burning plasma operation, which will have dominant electron heating given by the α-particles like ITER, and for steady-state operations, on top of which some DEMO devices are designed.

Main reference scenarios of JT-60SA are inductive scenarios (at high ($0.9 \times n_G$) and low density ($0.45 \times n_G$)) and advanced scenarios, among which one is hybrid and the other fully non-inductive at high β_N. These four different scenarios have been studied in this chapter.

The NB system of JT-60SA features 12 NBs with positive ion sources (PNBs) which provide 24 MW at 85 keV and 2 NBs with negative ion sources (NNBs) which provide 10 MW at 500 keV. The former system is split further in 4 tangential beams (2 co- and 2 counter-current) and 8 perpendicular beams. Due to the energy of these beams, the injected power couples mostly with bulk ions. The N-NBs are injected off-axis (the beam injection is around 0.6 m below the midplane) and they couple mostly with electrons. This system will give the power for non-inductively external driven current.

In order to simulate NBI using ASCOT tool, the beamlet design must be implemented, and this has been done in the framework of this thesis. The P-NBs and N-NBs beamlet geometry has been extracted from the grid design and tested for ASCOT. Benchmark has been carried out versus the reference JT-60SA scenarios developed up to now, showing a good agreement.

As an overall estimation of the NBI EP confinement, the shine-through is usually low in the four cases studied and the wall-losses are negligible. The scenario featuring the highest amount of wall losses is the low-density, full I_p inductive scenario. This happens because this one is the only one featuring the counter-injected positive beams, which give origin to particles trapped in banana orbits which move outwards in the plasma poloidal section. These particles create a hotspot in power deposition, but the power deposited by unconfined orbit or shine-through is not harmful for the device first wall.

Deposition from the beams is usually optimised and the shine-through values are well below 1%. The deposition from the tangential PNBs is peaked around the edge because of the beams attenuation. The perpendicular beams guarantee a deeper deposition, up to the plasma core, but in the case of full I_p (at high density) the beam deposition cannot reach the inner plasma.

In the different scenarios analyzed, the highest amount of trapped particles arise from the perpendicular PNBs (reaching up to the 100% for the third-energy component) and this can be explained by the dependence of the initial pitch on the EP orbits: in fact, the lower the pitch the inner is the radius labelling the passing-trapped boundary. Since for perpendicular PNBs the pitch is close to 0, the particles have an higher probability to born in trapped-orbit region, as it is in the cases here analyzed. For the tangential beams, the fraction of trapped particle orbits lies around 50%. In the case of NNBs, this fraction is quite dependent on the q-profile due to the particular injection geometry of this system. As an example, in the case of hybrid advanced tokamak this fraction is 80%, while for full-CD scenario it drops to 8%.

The deposition of power to electrons is dominated by N-NBs for all the scenarios. The integrated power is around 30% of the injected power in the majority of the cases, except for the low-density full I_p case, where it drops to 25%. N-NBs power is split equally between electrons and ions, but the deposition to bulk ions is dominated by P-NBs, thus more spread along the radial coordinate. Power to ions is much higher, due to the great quantity of power devoted to couple to this species. In the reference cases analyzed, around 10% of the power is deposited to main impurity (C).

The driven current is given, as expected, mostly by N-NBs, so it is driven off-axis. In the cases where it is not a strong requirement (i.e. inductive scenarios) the driven current fraction is below 10%, for an efficiency below $0.1 \times 10^{20}\,\mathrm{A\,W^{-1}\,m^{-2}}$. For advanced tokamak scenarios the efficiency is still quite low and this is due to the fact that the density is in these cases lower. Anyway, the induced current is much higher with respect to inductive cases, going from 20 % for hybrid scenario to 33 % of full-CD scenario. Furthermore, in the case of full-CD, the deposition of current is strongly concentrated where the q profile is expected to be reversed.

The 2D distribution function (solution of the Fokker-Planck equation) is as well analyzed for the N-NBs, due to their extreme features, new in fusion devices. The particle density (as well as the pressure) is always peaked around the injection magnetic surface, moving slightly to the high-field side due to particles orbit. The (ξ,E) 2D distributions show that the particles tend to be more concentrated in the area where the pitch is maximum and the energy is close to the critical energy: this is given by a 'boundary effect', in fact when the particles reach the maximum pitch they can only start decreasing it, making the distribution function more dense at the border. This effect is present in all the scenarios, exception made for high-density inductive scenario, where the critical energy is so low that this effect is visible only at lower energies.

Trapped orbits in plasmas experience a high radial displacement due to their shape. This radial displacement depends on the parallel velocity of the particle and on the poloidal magnetic field. JT60-SA EP have a high parallel velocity, in particular the negative beam particles, and in some cases the poloidal magnetic field can be quite low, in particular for advanced scenarios. In this work, the size of these orbits has been calculated from the simulations, ranging from 3 cm to 10 cm in the case of 85 keV particles, while the banana width can get to more than 20 cm in the case of 500 keV particles in AT scenarios. The radial excursion these particles will follow could induce high losses, in particular when perturbation to the 2D axialsymmetric magnetic field are added (e.g. the toroidal field ripple).

Measuring and modelling the impurity content is a tricky task to accomplish. In this thesis, some different impurity content profiles (i.e. Z_{eff} profiles) have been used to assess what is the impact of the impurity content on NBI for fully-CD scenario. Three profiles have been chosen: the reference flat profile, one assuming core accumulation and one assuming edge-accumulation of the C impurity. The main differences lie in the power deposited: C tends to absorb up to 20 % of the NB injected power when accumulating in the core, while the power absorbed drops below 10 % in the edge-accumulation case. The induced current is slightly affected by the different impurity content, even if the shielding is different for different impurity distribution. These results suggest that the current induced by the beam is expected to remain the same, so this would not impact strongly on the plasma performance; accurate studies on impurity transport would be needed to have a correct power deposition to the different species.

Lastly, a scoping study has been done by changing the N-NBs particle energy (and power, keeping a constant perveance) for full-CD scenario. This is interesting both for the non-target plasmas and the excitation of Alfvén eigenmodes. Decreasing the energy, the penetration of the particles is lower, as the reduction in the magnitude of the fast ion birth profile confirms and the power fraction to ions increases, according to slowing-down theory. The efficiency in current drive decreases as well, and this can be done due to the drop in slowing-down time, which decreases of 100 ms between the highest and the lowest energies studied. Using lower energy negative beams could be interesting for excitation of Alfvén waves, but it can be detrimental for plasma performance.

In conclusion, the reliability in the NBs as heating systems for JT-60SA is well posed: the EP are well confined and the N-NBs are a strong and reliable handle to obtain the desired driven current. P-NBs, on the other hand, provide high ion heating all over the plasma. Attention must be given to the impurity content in order to obtain the desired heating. Modulation of the N-NBs energy is a powerful tool which must be used carefully in order not to ruin the plasma configuration, such as the current distribution.

The analysis of the reference scenarios here presented is a starting point for advanced simulation of fast particles behaviour in JT60-SA. The results can be used as input for wave-particle interaction studies (e.g. excitation of Alfvén eigenmodes), and the accurate modelling given by the complex tools BBNBI/ASCOT can provide reliable deposition profiles useful for integrated modelling. Furthermore, an accurate description of the JT-60SA beam system in ASCOT could be used to model fast ion losses on the 3D wall and help in the design of a fast ion loss detector. Lastly, the 3D configuration of the external magnetic field could be implemented in ASCOT, assessing its impact on the particle losses.

Chapter 5

NBI modelling on TCV advanced tokamak scenarios

In this chapter, the results of modelling using intepretative tools on TCV advanced tokamak scenarios are shown.

After an introduction on the TCV device and its heating neutral beam, the activities done for a correct modelling on the device are shown, with comparisons between the different tools used. Interpretative analysis on energetic particle physics is then presented, analysing the impact ECRH has on the EP physics on TCV advanced tokamak scenarios.

5.1 TCV device

TCV (Tokamak à Configuration Variable) [79] is the medium-size tokamak at Lausanne Polytechnic Federal School (CH). It is one of the three devices in operation under the MST1 work package of the EUROfusion consortium [80]. The main parameters of the device are listed in table 5.1. The high number of poloidal field coils (i.e. 16 ex-vessel coils plus 2 in-vessel coils) allows this device to perform high shaping and for this reason a research line of the group is to look for alternative or unconventional configurations which could solve the issue of the power fluxes a DEMO-like device could face.

Among the other research fields the device is exploring, remarkable are the development of ITER-like scenarios, disruptions and runaway electrons physics, development of real-time control and wall cleaning experiments.

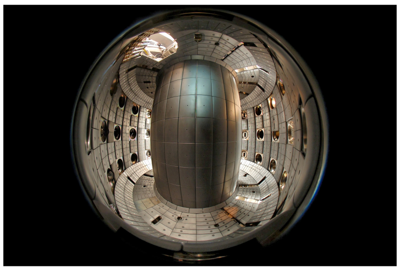

FIGURE 5.1: Photo of TCV device

R_0	0.88 m
a	0.25 m
B_0	<1.5 T
I_p	<1 MA
NB heating	<1 MW
ECRH heating (X2)	<0.6 MW
ECRH heating (X3)	<1.15 MW
N. of poloidal field coils	16(ext.)+2(int.)

TABLE 5.1: Parameters of TCV tokamak

The electron system resonant heating (ECRH) system incorporates two subsystems: X2 (second harmonic) used for electron heating up to cutoff density $4.2 \times 10^{19}\,\mathrm{m}^{-3}$ with efficient current drive; X3 extends the density range for EC heating up to higher density $11.2 \times 10^{19}\,\mathrm{m}^{-3}$ (cutoff limit) suitable for H-mode confinement regime.

In 2015 the device went onto a major upgrade [81]: the ECRH power will be increased by 2 MW and a neutral beam for plasma heating has been installed. The status and modelling of TCV neutral beam is the topic of this chapter.

5.2 TCV neutral beam

Starting from 2010, the installation of an NB system for ion heating was foreseen for TCV. The main heating system of TCV was ECRH, coupling mostly with electrons, but an NBI with low energy couples mostly with ions. Neutral Beam Heating (NBH) allows to widen the operational scenario of TCV (reaching $T_i/T_e > 1$ with record T_i of 3.7 keV in H-mode [82]), providing direct momentum input to the plasma and generating a high fast ion population fraction to study wave-particle interaction phenomena of interest for burning plasmas.

A 1 MW, 25 keV D^+ beam has been designed for TCV device [83], [84], [85] and successfully installed on TCV by enlarging one of the already-existing ports. The beam is injected tangentially co-current (clockwise from above) on the mid-plane position, as figure 5.2 shows. TCV plasma can be moved up or down and this would make the beam injected off-axis.

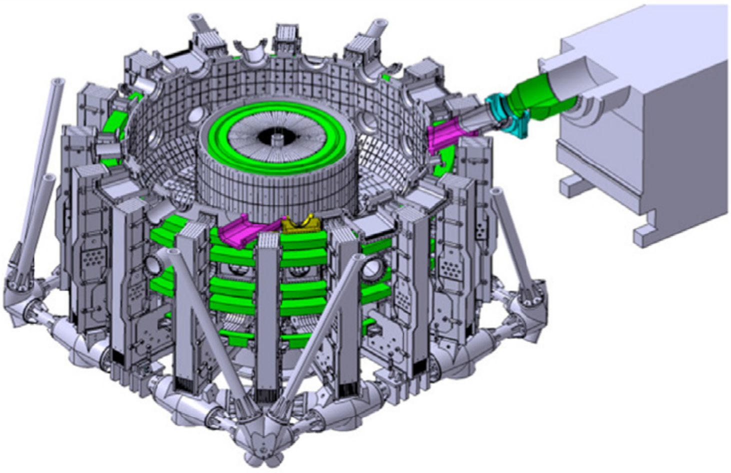

FIGURE 5.2: Design of heating beam injection on TCV.

5.2.1 NBI operation on TCV

The results here presented have been reported in [86]. The heating neutral beam was routinely used in TCV experiments: about 30% of TCV discharges (> 2000 shots) used NB injection into plasma since NBI installation. Figure 5.3

shows distributions of NBH shots in TCV, with different acceleration voltage (particle energy) and total injected energy (integral of power over time) for 3 years of operation.

The accurate and time consuming beam optimisation in September 2017 made it possible to reduce beam power losses in the beam duct and increase the safe duration of 1 MW beam from 0.5 to 0.8 s per shot, see maxima in figure 5.3a for 2016 (0.5 MJ) and 2017 (0.8 MJ) both at 25 keV (and 1 MW). A significant fraction of NBI shots at low energy/power has been dedicated to experimental studies of power dependences (e.g. L-H mode power threshold), plasma toroidal rotation vs external torque and correlations of fast ion turbulent transport and instabilities vs energy (fast ion velocity).

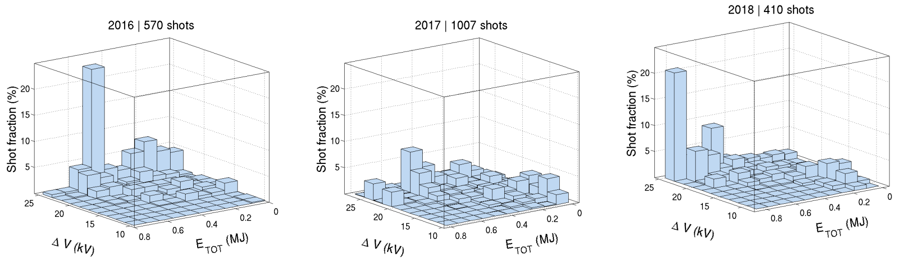

(A) Statistics for year 2016 (B) Statistics for year 2017 (C) Statistics for year 2018 (up to june)

FIGURE 5.3: NBH in TCV in the last 3 years: fraction of NB shots vs acceleration voltage ΔV (beam energy) and total injected energy E_{TOT} per shot

A neutral power variation in the range of 50 kW. . . 1.05 MW has been implemented on TCV by simultaneous variation of RF power (plasma density in the source) and extraction voltage keeping a minimal beam divergence (Figure 5.4). The optimisation procedure for the TCV NBI was periodically (1-2 times per year) performed at several (5-8) extraction energies; the optimal beam currents were experimentally adjusted by tuning the RF power to minimise the beam divergence (corresponding to a minimum of the beam width on the calorimeter). The voltage on the suppression (2nd) grid and the bending magnet current were also optimised at each power/energy level.

5.2.2 Beam profile measurement on W target

The NB ion optical system (IOS) was designed to extract the beam with divergence ≤ 20 mrad across and ≤ 12 mrad along slits with geometrical focusing at 3.6 m. The power losses in the beam duct between exit from injector tank and entering the TCV vacuum vessel were predicted to be 40 kW for which most of the internal surfaces of the port were expected to remain $< 100\,^{\circ}$C. The predicted power density profile is shown in figure 5.5a.

The commissioning of the NB showed high overheating of the duct. Thermocouples measurements showed that maximal temperature estimated on the inner surfaces of the duct was $\sim 500\,^{\circ}$C per 1 MW 2 s NB shot. Related to this observation, an in-house built device to assess the 3D power density distribution of the beam in the duct region has been installed. This device featured a 4 mm actively cooled tungsten (W) tile inclined 45° with respect to

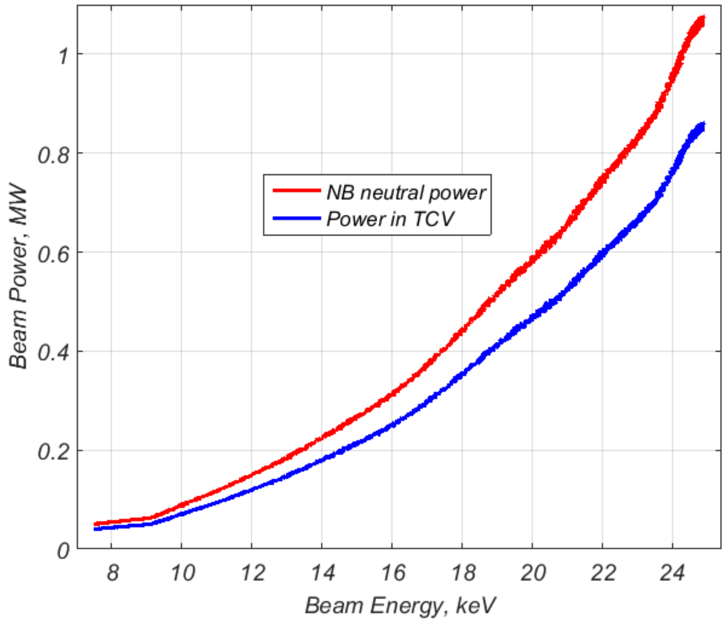

FIGURE 5.4: Neutral power (i.e. power of the neutralized ions extracted from the source) and power in TCV (accounting for beam duct losses) as function of energy. The maximum perveance is achieved at each different energy.

the beam to reduce the thermal impact of the power density. An IR camera records the surface temperature. The device could be moved along the beam axis (z) ranging all over the duct. Measurements on the duct entry are shown in figure 5.5b for different power levels. At maximum power (red line) the profile is perturbed by sputtering of the target. The simulated dimensions are represented by the vertical black lines. The beam profiles radii and aspect ratios are clearly different from the design values: the horizontal dimension of the beam is much greater than planned and this causes the unexpected power losses on the beam duct walls, thus the limitation for maximal beam duration. The measured power distribution corresponds to a beam divergence 36×8 mrad.

The high beam divergence in the horizontal direction is caused by two critical inaccuracies in machining of ion optical system (grids):

- machining inaccuracies of the plasma electrode emission slits;
- discrepancy between the accelerating gap and plasma density profile in the plasma box.

The re-fabrication of IOS is ongoing with the hope to install new grids this year, to allow extending the duration of 1 MW beam up to nominal 2 s (for a total energy of 2 MJ).

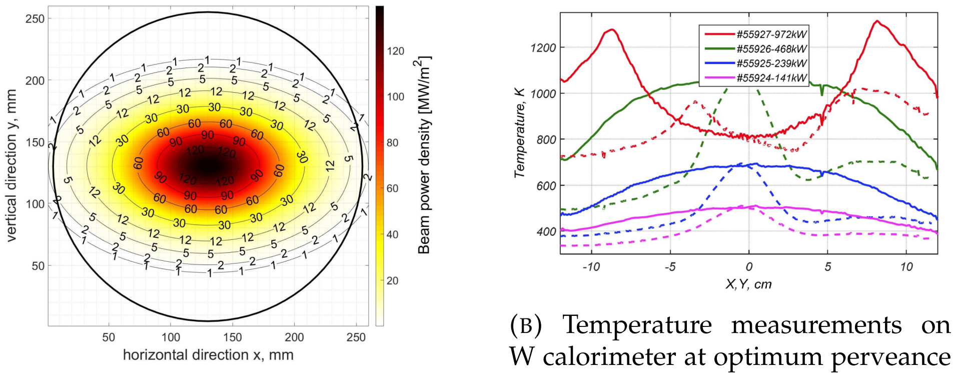

(A) Expected beam power density at duct entrance

(B) Temperature measurements on W calorimeter at optimum perveance along X (solid) and Y (dashed) direction.

FIGURE 5.5: Beam divergence modeled and measured

5.2.3 Scenarios with NBH: ELMy H-mode

The NB injection on TCV allows more flexibility in entering H mode plasmas and providing access to ITER-relevant scenarios. A specific TCV experimental mission was devoted to establishing a reliable H-mode with Edge Localised Modes (ELMs), high density, the maximum attainable Psep and possibly divertor detachment. H-mode plasmas with $\beta_N \approx 1.8$ were obtained in TCV (see figure 5.6). In the shot shown here, NBI results in the L-H transition without using ECRH and a back transition occurs only when the beam is turned off.

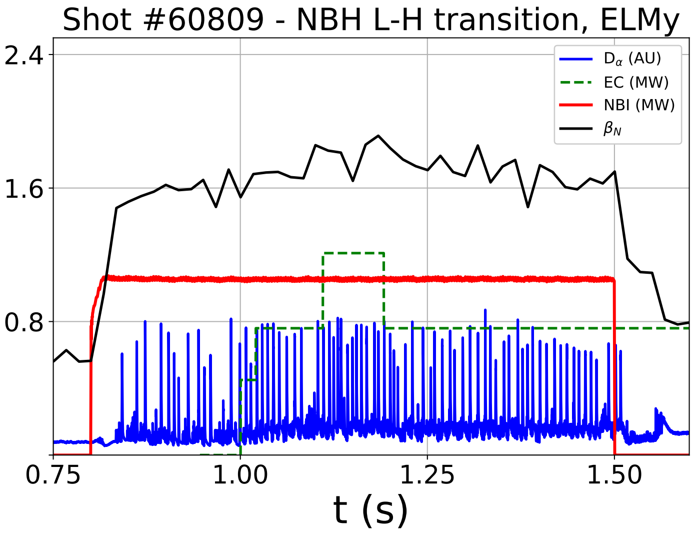

FIGURE 5.6: Example of ELMy H-mode obtained with the additional power of the beam.

NBI in TCV is also a relevant tool for AT scenarios in TCV. This kind of scenarios has been studied in the framework of this thesis and will be presented more in detail.

5.3 NBI modelling on TCV: NUBEAM and ASCOT

The importance of NBI modelling in TCV is even more significant because of the high fraction of EP NBI will create and the additional heating it will supply the plasma with. The beam drives also current in the plasma, which must be correctly calculated to develop AT scenarios.

The tool chosen for NBI interpretative modelling is NUBEAM:

- it is a reliable Monte Carlo modelling tool used world-wide (e.g. JET, DIII-D);
- it implements Charge-eXchange (CX) reactions, which can be significant in TCV;
- it couples with TRANSP, a suite to simulate a full tokamak discharge.

NUBEAM and TRANSP accepts as input the same data format. The interface between TCV data and NUBEAM has been done using OMFIT [87] (One Modeling Framework for Integrated Tasks) framework. This tool is under development at General Atomics (GA) (San Diego, California, USA) but allows external contributors to expand the code.

The best description of this tool is the following [88]:

> *OMFIT is an integrated modelling and experimental data analysis software for magnetically confined thermonuclear fusion experiments. The goal of OMFIT is to enhance existing scientific workflows and enable new integrated modelling capabilities. To achieve these goals OMFIT adopts a bottom-up collaborative development approach.*

OMFIT is developed using Python and it is structured as a set of nested python dictionaries (i.e. structures containing a mix of data types) and classes. OMFIT is designed to be a platform where create the input data for the different codes implemented; it then manages the connection to the servers where these codes are already installed and running routinely (e.g. TRANSP/NUBEAM at Princeton Plasma Physics Laboratory (PPPL)), sends the data and runs the code.

This approach is made even more comfortable for a user thanks to the Graphical User Interface (GUI)implemented in OMFIT, which makes the input preparation an easy task also for non-developers. Furthermore, in the case of TRANSP, each device has its own set of routines which are built specifically for gathering the data from the different MDS+ tree: once the data are retrieved, they are converted in the input for NUBEAM in a standard way.

The OMFIT setup has been implemented for TCV in the framework of this thesis. This time-consuming activity has been supported by TCV, PPPL and GA colleagues.

Results using TRANSP on TCV (outside the OMFIT framework) have already been presented in [89], where the fast ion transport has been studied in L-mode plasmas using fast ion D-α emission and TRANSP code. In this thesis, the same code and the results from that analysis will be applied to advanced tokamak plasmas.

5.3.1 ASCOT beamlet-by-beamlet implementation

ASCOT has been implemented as well for NBI modelling on TCV: this tool has been chosen because it implements a more detailed beam shape and it can compute the particles orbit in 3D configuration, useful for 3D wall losses estimation. In order to do so, the grounded grid of the ion optical system has been implemented in ASCOT. The design of this grid is shown in figure 5.7a, where the unusual shape of the beamlet can be seen. In fact they are elongated ellipsis, with a high divergence (20 mrad) across the slits and a low divergence (12 mrad) along the slits. Since ASCOT beamlet geometry allows only circular beamlets with one divergence, TCV beamlet divergence has been set to 17 mrad, which is an average between the two values of the overall beam divergence. Furthermore, no beam waist (i.e. beam width) at the focal point has been set.

The beamlet position has been set to be the centre of each slit of the designed grounded grid, and the result for the beamlet position can be seen in figure 5.7b.

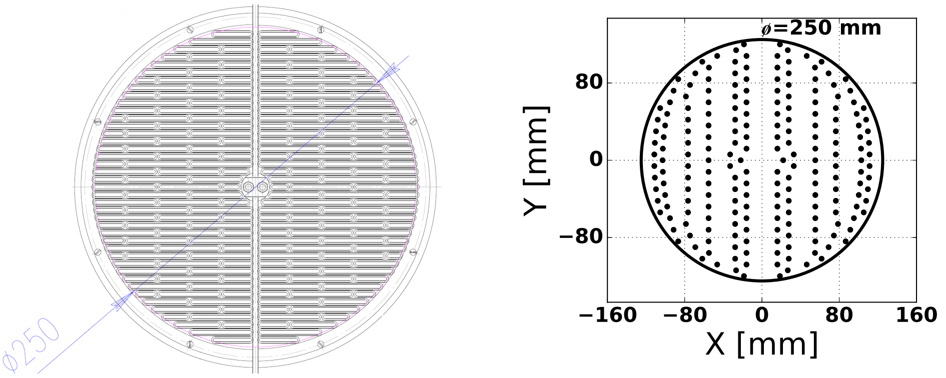

(A) Grounded grid of the ion optical system of TCV heating NB injector.

(B) Grounded grid implemented in ASCOT.

FIGURE 5.7: ASCOT implementation of TCV heating-NB grid geometry.

5.3.2 ASCOT-NUBEAM beam footprint benchmark

The design of TCV heating NB has already been implemented to carry out the results presented in [89]. NUBEAM beam implementation is a narrow-beam model and the two divergences have been set differently in the two dimensions. A comparison between the ionisation results with NUBEAM and ASCOT has been done. A reference plasma has been chosen and the marker ionisation positions have been compared. NUBEAM implementation has two different divergences in the R-z directions, which are 22.5 mrad and 5 mrad respectively.

Assuming NUBEAM as the benchmark case, three different divergences have been chosen for ASCOT: 8 mrad, 36 mrad and 22 mrad, which is the average value between the two. This scan in beamlet divergences has been carried out to see which of the beamlet divergences in ASCOT better approximates the divergence in NUBEAM.

In the z-histogram (5.8a) it can be noted that ASCOT 8 mrad divergence is not in agreement with NUBEAM results. Also the 36 mrad case tends to be quite different from the NUBEAM case, while 22 mrad is in agreement. This of course is due to the different shape assumed in the beams, in fact the narrow beam modelled by NUBEAM has also a fixed beam width at the focal point while ASCOT is assumed to focus totally at the point (without any width there). This difference is anyway smoothed by assuming 22 mrad divergence. This is also in good agreement in the case of the histogram in R direction (figure 5.8b), even if NUBEAM results in a higher rate of ionisation in the inner core of the plasma ($R \sim R_0$).

In any case, the differences between the two different implementation can be explained in the different way of beam implementation (i.e. narrow beam versus beamlet-by-beamlet) and by the different divergence, since in ASCOT the beamlet divergence is assumed to be an average between the two (horizontal and vertical) beam divergences and with zero beam width at the focal point.

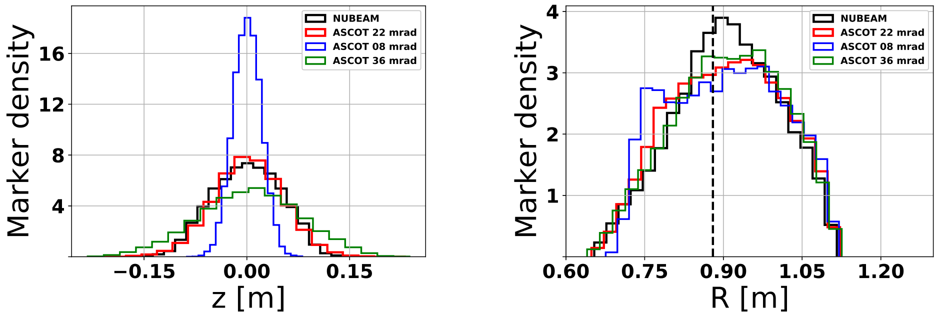

(A) Histogram on elevation of the marker borning positions.

(B) Histogram on major radius of the marker borning positions.

FIGURE 5.8: Histogram of the beam trajectory in the two different codes. Different beamlet divergences have been chosen for ASCOT: 22 mrad (red), 8 mrad (blue) and 36 mrad(green)

In figures 5.9 the sections are shown between NUBEAM and ASCOT with 22 mrad: the RZ (5.9a) section seems not to differ much between the two codes. The XY (5.9b) section shows that NUBEAM has a larger cross section inside the plasma.

Figure 5.10 shows the marker position in 3D real space, and the same injection geometry and trajectory can be seen.

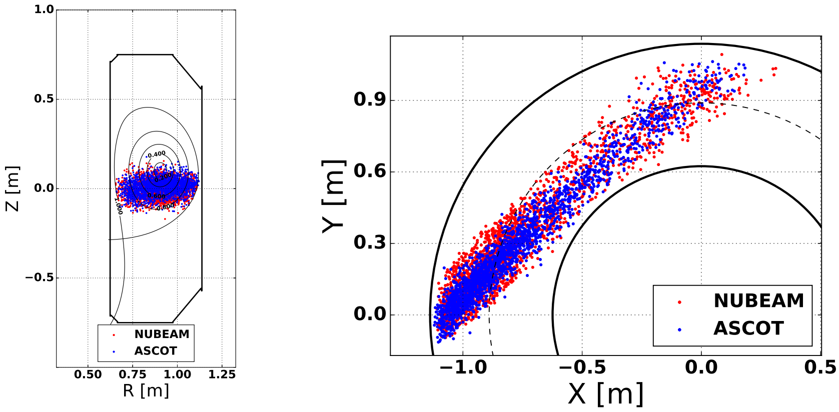

(A) Poloidal projection

(B) Top view

FIGURE 5.9: Sections of the beam trajectory in the two different codes.

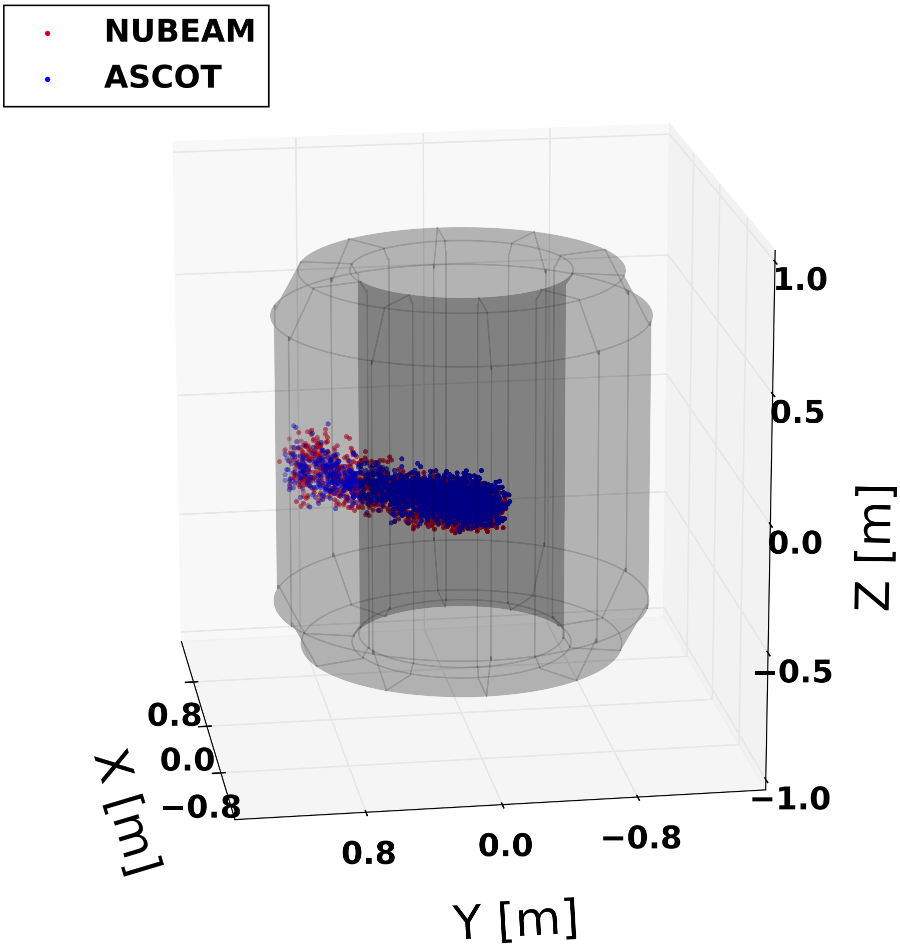
NUBEAM
ASCOT
1.0
0.5
0.0
−0.5
−1.0
Z [m]
0.8
0.0
−0.8
X [m]
0.8
0.0
−0.8
Y [m]

FIGURE 5.10: 3D trajectory of the beam.

5.3.3 ASCOT-NUBEAM comparison on EP slowing down

NUBEAM and ASCOT implement different physics within them, as listed in section 2.8. One of the most important differences is the implementation of charge-exchange losses, model implemented in NUBEAM but not in ASCOT. This difference is quite important for TCV, and this is why the interpretative modelling will be carried out with NUBEAM. Anyway, the difference in the two models (with the charge-exchange losses in nubeam minimized) is here analyzed, in order to confirm the limitation that ASCOT has when modelling TCV plasmas.

In figure 5.11 the difference in the power balance (at a given timeslice) is shown. The charge-exchange losses have been minimized in nubeam by minimizing the neutral density in the plasma. It can be seen that the shine-through differs by 2%, difference given by the different model of the beam in the two codes. The difference in the absorbed power is around 3% of the injected power and the power lost by orbits differs only by roughly 3%. The charge-exchange losses, calculated from NUBEAM, is around 8% of the injected power. The agreement between the two codes is good, bearing in mind the charge-exchange issue.

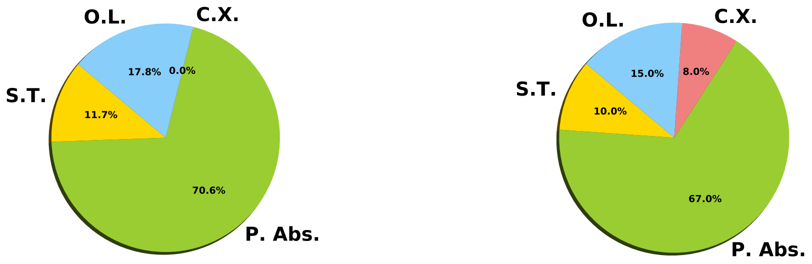

(A) Power balance computed by ASCOT.

(B) Power balance computed by NUBEAM.

FIGURE 5.11: Comparison in power balance scalars between ASCOT and NUBEAM. Light green is the absorbed power, yellow is the shine-through, blue is the orbit losses, red is the charge-exchange.

The comparison in slowing-down quantities such as total deposited power and distribution function in energy is satisfying as well. Figure 5.12 shows the comparison between the two codes for the total power deposited in the plasma and the unshielded driven current from the beam. The differences are small and this can be explained from the charge-exchange reactions. Figure 5.13 shows the energy distribution of the particles, and here as well the shape of the distribution function is similar. The small difference in magnitude can be as well explained because of the charge-exchange reactions.

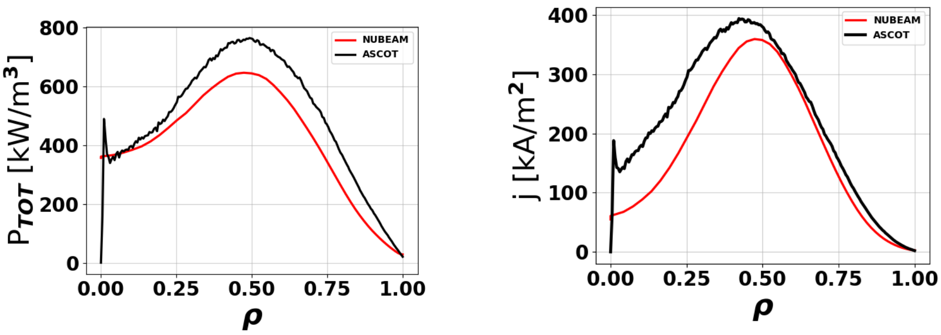

(A) Power deposition to plasma

(B) Shielded driven current in the plasma

FIGURE 5.12: Comparison in terms of power to plasma and driven current for ASCOT (black) and NUBEAM (red)

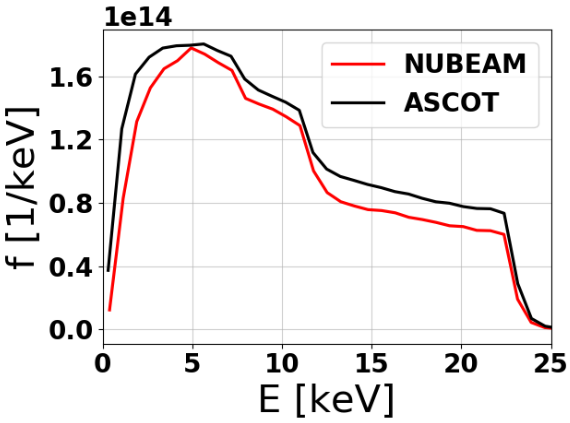

FIGURE 5.13: Particle energy distribution

5.4 Advanced tokamak scenarios on TCV under the EUROfusion consortium

Advanced tokamak (AT) scenarios on the TCV [90][91] have been improved in performance thanks to the additional power from the beam. The importance of this kind of scenarios is relevant within the EUROfusion consortium, and the Medium Size Device (MST) program [92] allocated resources for this topic.

One of the main objectives of the experimental campaign for AT scenarios under the MST program is to document performance (β) improvement with NBH in fully non-inductive, (ECCD-driven), stationary scenarios on TCV, with and without ITBs. Improvement in performance has been observed without ITBs, developing fully non-inductive plasmas using NBI. Figure 5.14 shows the results obtained for L-mode plasmas, each point representing the average over the time where the maximum value of β has been obtained for each shot. Increasing the additional power injected in the plasma, the higher values of β_N and lower values of loop voltage have been obtained, reaching fully non-inductive plasmas ($V_{LOOP} \approx 0$). In some cases, even negative V_{LOOP}

values have been seen.

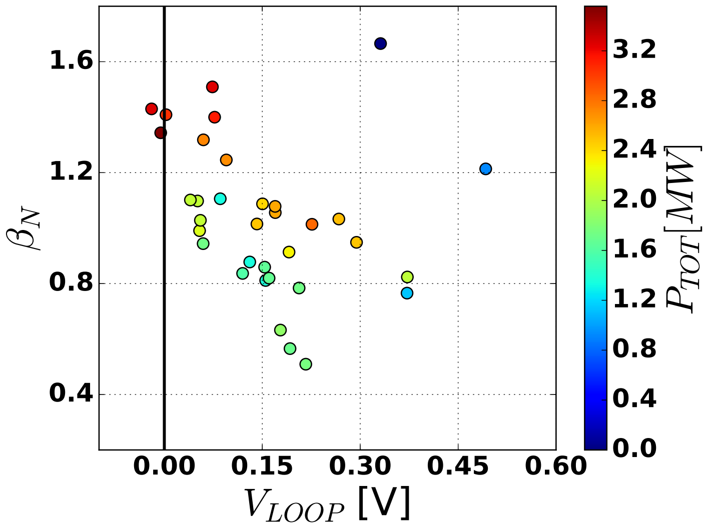

FIGURE 5.14: Performance of AT scenarios in TCV, under the MST program. The higher the additional power, the better performance are obtained (lower V_{LOOP} and higher β_N)

.

The impact of additional heating on this scenario is better seen in figure 5.15. The first figure (figure 5.15a) shows the impact of NBI power on the plasma normalised β. The fast ion pressure in this case increases the β_N significantly ($\sim$ 20%), at equal EC power. The electron energy (figure 5.15b), on the other side, seems not to increase with additional heating power from the beam. This means that the beam could deteriorate the heat confinement properties of TCV AT plasmas.

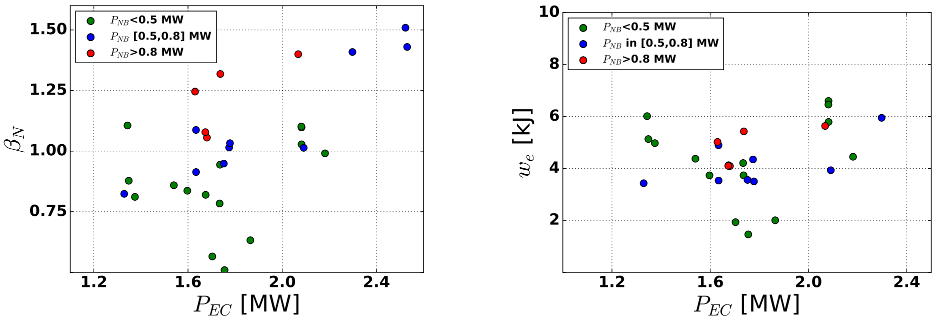

(A) β_N for the AT shots, at different EC power. The colorscale labels the NBI power range.

(B) w_e for the AT shots, at different EC power. The colorscale labels the NBI power range.

FIGURE 5.15: AT plasma performance as function of the additional power.

An internal transport barrier can be generated by reversing the q-profile using EC current-drive (ECCD) [93], although if this complex task has not been achieved yet because of the broad NB current drive profile, which deteriorates the q-profile reversal [94][95][96]. The starting condition is, furthermore, a fully relaxed q-profile, because it is not possible to reverse the profile at current ramp-up. Lastly, the EC system was not all the time fully operational and this interrupted the localised EC current drive, necessary for this purpose.

5.5 Effect of EC on TCV AT scenarios

5.5.1 Edge neutral pressure measurements

Neutral pressure at the wall is measured using baratrons similar to the ones installed at JET [97]. The typical values of neutral density at the edge n_0^{LCS} are around $2 - 8 \times 10^{16}\,\mathrm{m}^{-3}$, as figure 5.16a shows. The bump in edge neutral density before 0.5 ms is given by the initial filling of the plasma chamber. In this standard shot, after beam injection starts at 1.2 s, the edge neutral density increases because of the beam-injected neutrals, still remaining below $5 \times 10^{16}\,\mathrm{m}^{-3}$. Adding EC wave injection (figure 5.16b), the signal shows a steep increase of the edge neutral density. This probably happens because the EC power heats up the sensor or electronics of the baratrons, i.e. the measure gets distorted. This modification in the neutral density at the edge (which will result in a neutral density increase all-over the plasma) will affect charge-exchange losses by the beam.

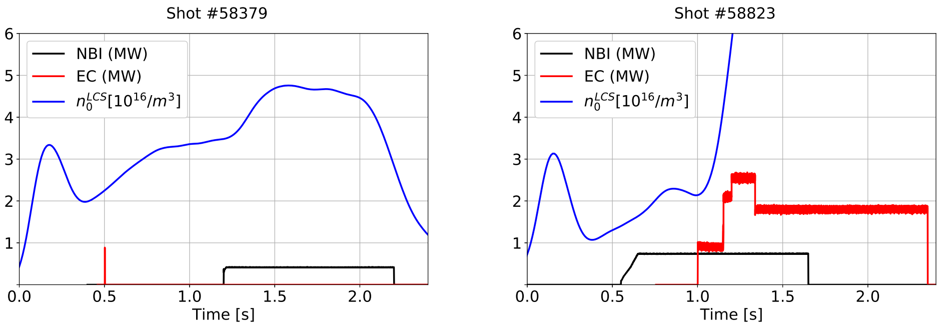

(A) Baratrons n_0^{edge} for a no-EC shot.

(B) Baratrons n_0^{edge} for an EC shot.

FIGURE 5.16: Baratrons measurements faults with additional power in TCV.

5.5.2 Impact of EC heating on plasma composition

In the discharges explored in this work, EC seems to cause a density pump-out which sums up with a high influx from the wall, causing both an increase of the plasma density, increase of neutral density (and CX EP losses) and increase of Z_{eff} (impurity density).

These observation started by calculating the components of the total plasma current. The three components are the ohmic current (driven by the loop voltage applied), the current driven (CD) by the additional heating systems, and the bootstrap (BS) current [98][99]. These three different components of the current can be computed with some assumption on the ohmic current: the loop voltage is assumed radially constant. The plasma resistivity is neoclassical [100]. The bootstrap current and the ohmic current are calculated starting from the experimental data. The current driven is calculated by subtraction, i.e.

$$I_{CD} = I_{TOT} - I_{OHM} - I_{BS} \tag{5.1}$$

Measurement of the ohmic contribution to the plasma current can be tricky. In particular, plasma resistivity linearly depends on the effective plasma electric charge. This dependency can be used to evaluate the plasma Z_{eff}:

- when no auxiliary heating is used, the plasma total current must be the sum of BS and ohmic current
- if the CD can be modelled, then the ohmic contribution (and the Z_{eff}) can be inferred.

The EC contribution to the current drive has been computed using the TORAY code, which is fully interfaced with TCV and used routinely. The NB contribution has been expected to be around $20 - 30\,\text{kA}$. An assumption on the NBCD can be quite bounding because of the strong dependency of the NBCD on the Z_{eff}, but these values have been measured in previous campaigns on TCV with the beam only.

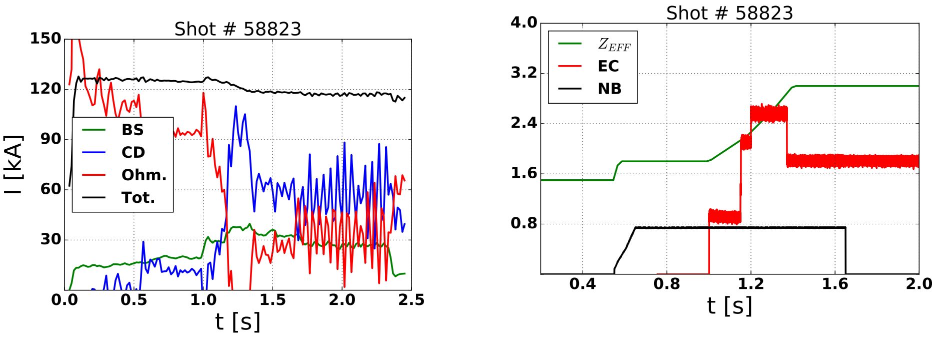

(A) Current drive and bootstrap for an AT shot in TCV.

(B) Inferred trend of the effective charge as function of additional power.

FIGURE 5.17: Computation of CD contribution to ohmic current.

The calculations for an AT shot on TCV are shown in figure 5.17. In figure 5.17a the contributions to the plasma current are shown. The high noise in the ohmic contribution to plasma current is given by the high variation in the V_{LOOP} measurement. Interesting is the time window 1.2-1.4 s, where the ohmic current drops to 0 A. In figure 5.17b the trend of the effective charge with the additional power is shown. NBH is expected to cause a slight increase in the effective charge due to the power deposition (and consequently erosion) of the beam duct and shine-through (causing sputtering from the wall). $Z_{eff} \sim 3$ has been inferred with EC: EC power arrives to the wall and causes higher recycling from the wall, causing an increase of the impurity content in the plasma.

This effect has been included for NBH modelling since the shielding of the NB CD and the power deposition is affected by the impurities.

5.6 EC impact on NBI-heated plasma - Shot 58823

5.6.1 Experimental results

One of the most successful shots (number 58823) obtained in TCV during the experimental campaigns has been chosen to study the impact of EC waves injection in a NBI-heated plasma. In figure 5.18 the experimental signals are shown. The current is around 130 kA, but the V_{LOOP} floats around 0 V. The values of β_N gets up to 1.5 using the available additional power (shown in figure 5.19a). The beam is set constant to 0.7 MW while the EC power should have been 2.5 MW but a fault in the gyrotrons made it possible only for a short time window. In this time window, the β is maximised. The electron density at two position of the normalised radius ($\rho = 0, 0.5$) are shown and when the EC power is turned on the effect of density pump out is clear, since the two values get close. The EC effect on the electron temperature is clear as well, with an increase of 2 keV in the plasma core. The magnetic configuration in this plasma didn't foresee an ITB, and this can be seen from the safety factor values shown. The minimum value of q is the one in the plasma axis, so no reversal is used in this shot. The beam is injected off-axis, in fact the plasma is displaces upwards of ~10 cm, as figure 5.19b shows.

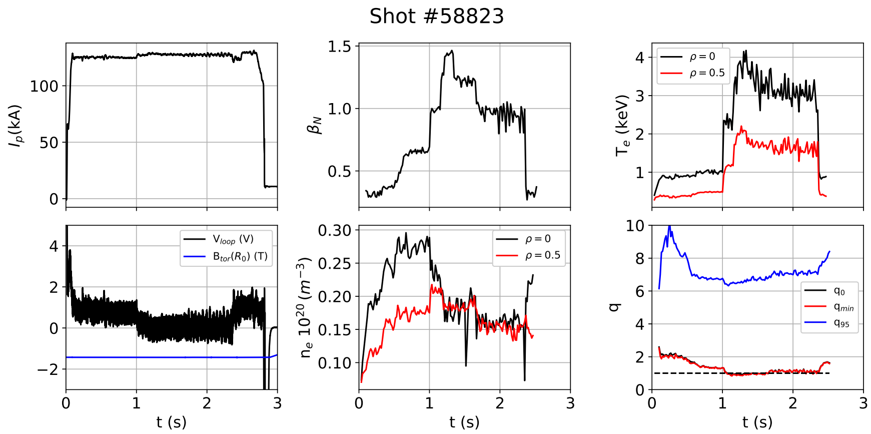

FIGURE 5.18: Experimental results for shot 58 823

5.6.2 Interpretative modelling with NUBEAM

NUBEAM has been used to study the impact of EC heating on the plasma and thus on the NBI power deposition. In this work, the EC has not been modelled: only the NBI has been studied, applied on a plasma influenced by EC wave injection heating. The input values have been read from the Thomson scattering diagnostic for n_e and T_e, while T_i has been read from the Charge-eXchange recombination spectroscopy. The ion density has been

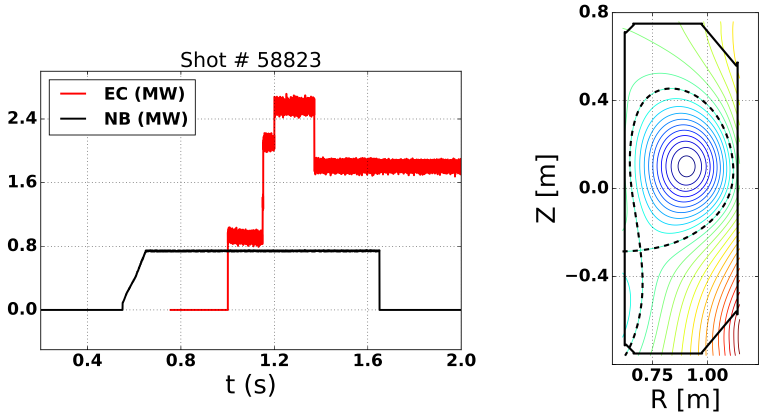

(A) Shot 58 823 additional power

(B) Shot 58 823 shape during flattop

FIGURE 5.19: Input auxiliary power and shape for shot 58823

computed from the Z_{EFF} considering only D and C in the plasma. The input volume-integrated values are shown in figure 5.20. The vertical lines in figure

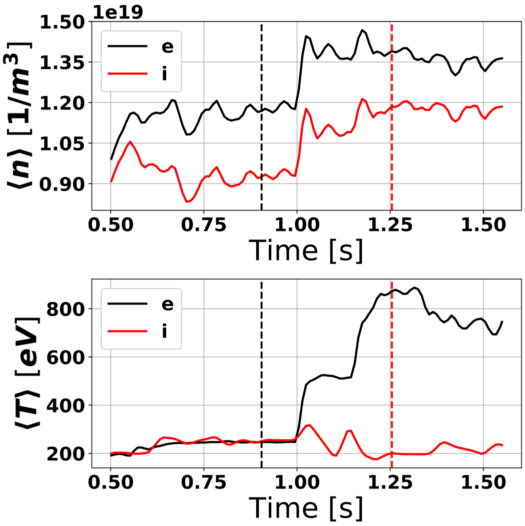

FIGURE 5.20: Volume-integrated temperature and density for NUBEAM analysis. Vertical lines represent the two time instants which will be used later in this work: 0.9 s is without EC heating, while 1.25 s is with maximum EC heating.

5.20 correspond to different additional power from the ECRH. The power in those cases is 0 MW at 0.9 s and 2.5 MW at 1.25 s. The power injected from the beam is 80% of the power shown in figure 5.19a because this factor accounts for the losses in the duct.

Benchmark with experimental data

In order to validate the input data used for NUBEAM/TRANSP simulations, the thermal energy of the plasma and the edge neutral density have been used as benchmark values.

The thermal energy of the plasma is measured in tokamaks using the diamagnetic loops and in the case of TCV the diagnostic is described in [101]. The plasma toroidal flux is measured, and this is defined as

$$\Phi = \int_{S_{PL}} (B_\phi - B_{\phi V}) dS = \frac{\mu_0^2 I_\phi^2}{8\pi B_\phi}(1-\beta_p) \tag{5.2}$$

where ϕ is the toroidal direction, the integral is computed over the plasma surface, $B_{\phi V}$ is the vacuum toroidal field, β_p is the poloidal beta

$$\beta_p = \frac{\langle p \rangle}{\frac{2\mu_0}{B_\theta^2(a)}} = \frac{2}{3}\frac{E}{\frac{2\mu_0}{B_\theta^2(a)}} \tag{5.3}$$

and so the plasma thermal energy density E can be evaluated. Integrating over the volume, we obtain the plasma thermal energy.

This measured quantity is compared to the plasma thermal energy calculated by TRANSP, which can be calculated as

$$E = \sum_i \frac{3}{2}(n_i - n_i^{fast})T_i + \frac{3}{2}E_{perp}^{fast} \tag{5.4}$$

being i the index labelling the thermal species in the plasma (electrons and ions). In the summation, the anisotropic population of fast ions must be removed, but the perpendicular energy of the fast particles (computed by TRANSP) is added to the sum. In figure 5.21 the comparison between the plasma energy is shown.

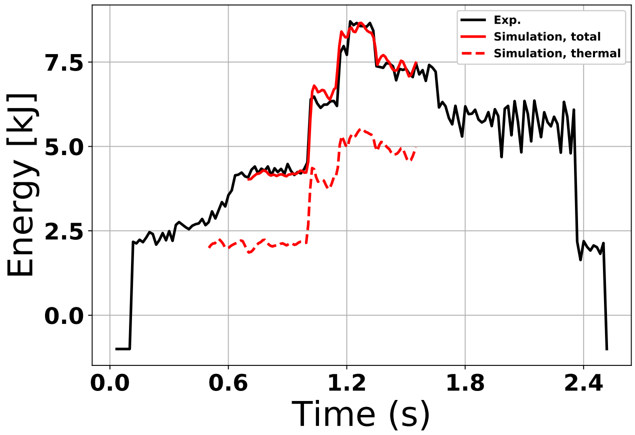

FIGURE 5.21: Benchmark between the measured thermal energy content (black) and TRANSP simulation (red). Continuous line is total plasma energy, dotted line is the thermal component to the energy,

Neutral content in devices such as TCV must be kept in consideration when simulating neutral beam injection. In TCV, as already reported in 5.5, the edge neutral density is measured using baratron gauges, and the measures from this diagnostic have been used as benchmark for TRANSP simulations. In TRANSP the particles confinement time can be manually set, allowing to control the ion outflux and consequently the particles recycling. In the cases here presented, the confinement time has been set so that the total plasma energy simulated matches the experimental plasma energy. Figure 5.22 shows the comparison in edge neutral density between the simulations and the experimental data for the case here studied.

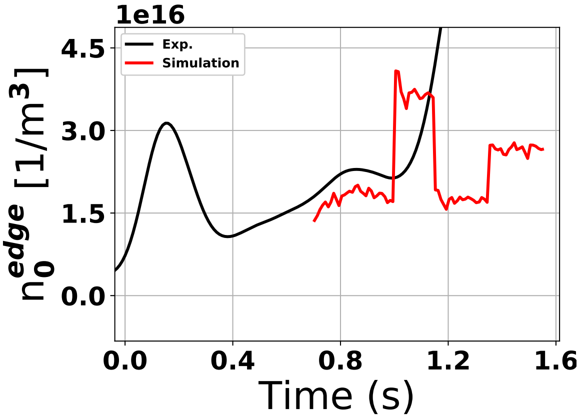

FIGURE 5.22: Neutral density edge value. Black line are experimental data while red line is simulated edge neutral density.

This comparison is acceptable only before 1 s because later on (with EC heating), the failure in the sensor prevents these data to be used. Before 1 s the simulation reaches a satisfying agreement with the experimental data when anomalous diffusion is neglected and with $Z_{eff} = 1.5$. After EC additional heating, no clues on the edge neutral density can be given by diagnostics, so the results shown here are so that the total plasma energy matches the experimental data. When setting the effective charge as stated in section 5.5 the edge neutral density drops strongly to unrealistic values and no match with experimental plasma energy could be reached. Furthermore, the best agreement is obtained with a constant value of $Z_{eff} = 1.5$. This information is opposite with respect to the analysis carried out in section 5.5. In that case, the simplified code accounting for the different contribution to plasma current prescribed an effective charge value of 3. The results for edge density obtained with TRANSP suggest that value is too high, so the value of 1.5 will be considered in the following analysis. The discrepancy between the two models can be explained by the simplified model used in the previous analysis (e.g. the loop voltage is assumed radially constant). It must be noted that the tool used for previous calculations is mostly useful for on-line interpretative analysis of the shot and does not account for current drive. In the neutral density profile, the value outside $\rho = 1$ is fixed in TRANSP through the whole discharge, so the value before EC injection will be used. This number is used to compute charge-exchange losses of fast ions outside the separatrix, so it is marginally impacting on the losses.

5.6.3 Power balance and power deposition to ions and electrons

The power which gets absorbed or lost during NBI has been calculated, and it is shown in figure 5.23. The loss channels are shine-through, orbit losses and charge-exchange losses. Turning EC on (starting from 1 s) a dramatic change in the power balance can be seen: in fact the power absorbed by the plasma drops from 50 % to 35 % (i.e. becomes 0.2 MW) and then further below 0.15 MW. This power gets lost in charge-exchange losses and orbit losses, being CX greater than 30%. The shine-through remains around 10, orbit losses increase to 20% Figure 5.24 shows the redistribution of absorbed power between ions and electrons. Most of the absorbed power (i.e. the one that doesn't get lost into orbit losses or charge-exchange) goes to electrons before 1 s but the power deposited to ions increases even when EC is added because of the increase in plasma temperature, which makes the critical energy to increase and thus the power deposition to be more effective to ions. Figure 5.24 bottom includes also the theoretical value G_i (volume-averaged, coming from equation 2.30) and we can see that it follows fairly well the fraction of power deposited to ions. The power deposited to electrons decreases when EC injection heating is added but the one to ions remains fairly the same.

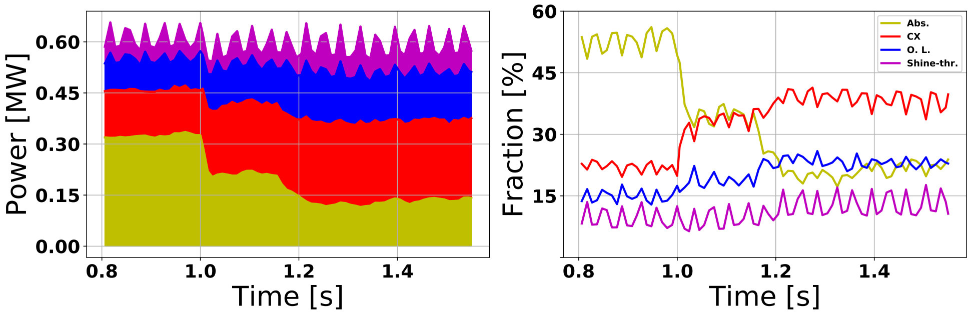

FIGURE 5.23: NB power balance. Left figure are the absolute values, right figure shows the relative values.

The radial profiles of the NBI-related quantities are shown in figure 5.25. Left figure shows the power deposited to ions and both a decrease in magnitude and an outward shift in the peak of deposited power can be seen. The power deposited to electrons decreases dramatically, showing as well an outward shift. The same shift is visible in the ion-deposited power (centre in figure 5.25) and this can be explained by an increase in the core slowing-down time: the fast ions deposit power slowly in the core with respect to the outer part. The right figure shows the fraction of fast ions with respect to bulk electrons and this value doesn't change much with EC injection. This confirms that the penetration length (and the EP radial generation zone) doesn't vary much with the EC injection (this is cross-checked by the low change in the shine-through value).

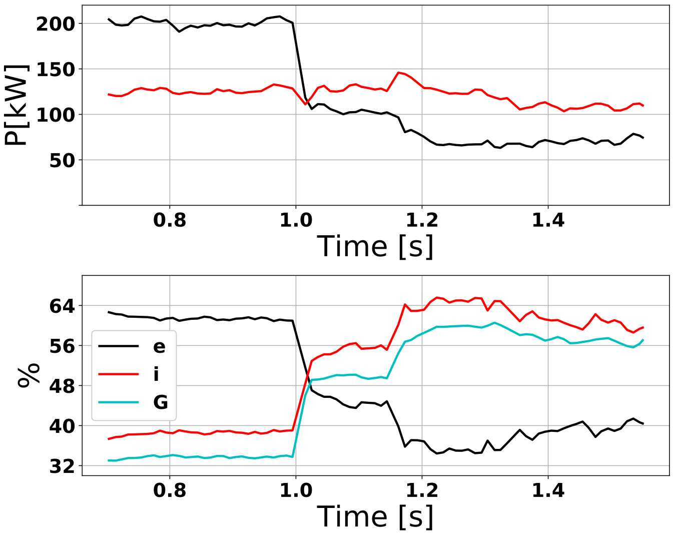

FIGURE 5.24: Power to ions (red) and electrons (black). Top: absolute values; bottom:relative values. Cyan line is the theoretical value for ions deposition

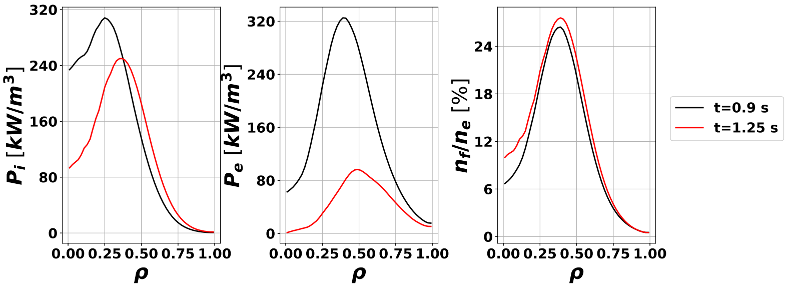

FIGURE 5.25: Radial profiles of power deposition and fast ion fraction for shot 58 823 at the different time-slices.

Current drive is modified as well (figure 5.26), both because of the change in plasma profiles and plasma composition (see section 2.6). Top-left figure shows that the unshielded current has a slight increase of ~50% with the additional heating by EC. On top-right the shielding factor $(1-\frac{I_{SH}}{I_{USH}})$ is shown and we can see that it drops from 45% to roughly 35% and its trend seems linked to the density profiles modification due to EC. Efficiency varies as well with varying driven current, reaching a maximum of 0.7×10^{18} A/Wm^2 with maximum additional power. The profiles in bottom-right figure show the decrease and the inward movement of the peak with increasing EC power.

The fast ion distribution function is strongly affected by ECH (Figure 5.27): energy distribution (figure 5.27a) is flatter with NBH only, while at the maximum EC power the peaks at NB full, half and 1/3 of injection energy (22.5 keV) are well pronounced. The EP energy distribution (~1/E) without ECH is typical for slowing-down without losses, but when EC power is added the slope of the curve tends to be positive, representing high EP losses (CX, orbit). Consequently, with NB only low-energy region (E<6 keV) are

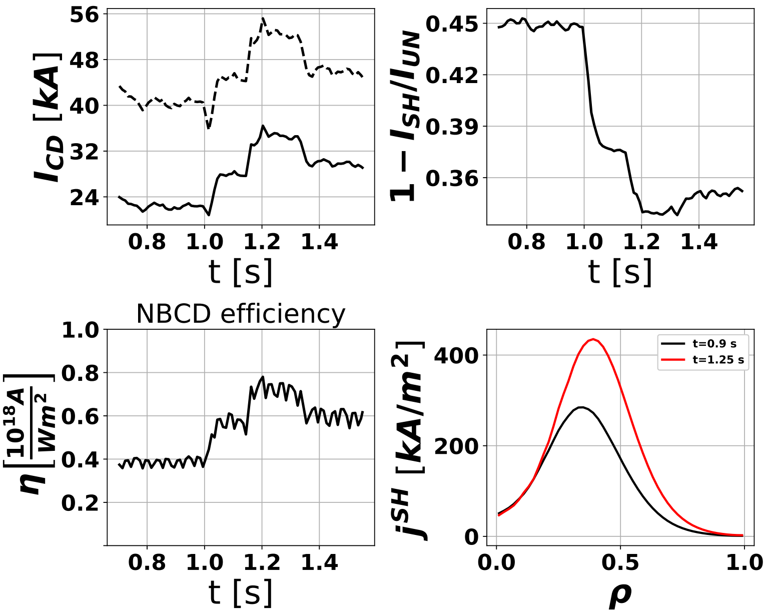

FIGURE 5.26: Neutral beam current drive for shot 58823. Top-left: shielded and unshielded current; top-right: shielding factor; bottom-left: NBCD efficiency; bottom-right: NBCD profiles

more populated. We can note from figure 5.27b that the pitch distribution is not affected that much: with full EC power the population of particles with higher pitch decreases slightly.

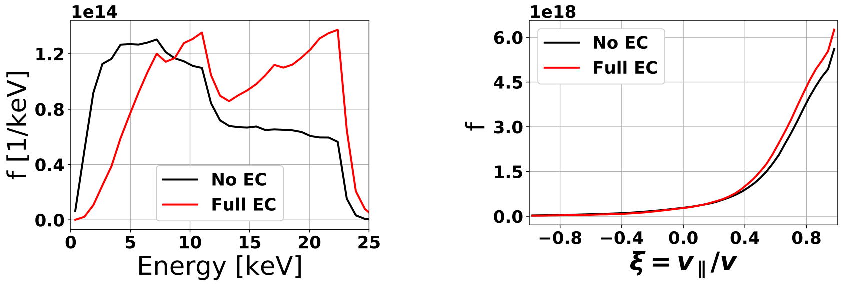

(A) Particle density in energy with and without ECRH

(B) Particle density in pitch with and without ECRH

FIGURE 5.27: Fast ion energy and pitch angle distributions as function of energy (a) and pitch (b). In (b) the difference between the two functions (no EC-max EC) is shown in red.

5.6.4 Interpretative wall loads using ASCOT

Power deposition of EP to the TCV wall has been calculated using ASCOT. The total wall losses increase with EC, in fact without ECRH the losses are around 95 kW, while adding EC the losses get to 165 kW.

In figure 5.28 the power loads to the wall with EC are shown. The NBI EP born position is around $\frac{3}{4}\pi$ in toroidal angle ϕ and 0 in poloidal angle θ. The losses span all the toroidal angle ϕ but they concentrate between $-\frac{\pi}{4}$ and 0 in θ. The hottest spot (red in the figure) are slightly below the midplane ($\theta = 0$). The small amount of losses below $-\frac{\pi}{2}$ are the losses getting to the wall following the plasma leg.

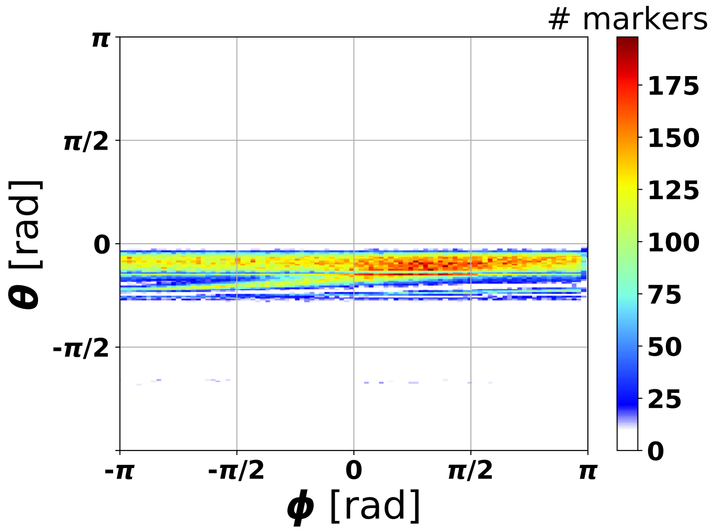

FIGURE 5.28: Maximum losses to the wall.

The configuration of the magnetic profile is important while assessing EP losses. The q-profile (i.e. the number of poloidal turns the magnetic field line accomplish in a single toroidal turn) is shown in figure 5.29. The profile with EC is lower because of a higher induced current in the plasma. Anyway the difference in the two profiles is not so dramatic to imply a strong difference in the EP orbits.

In figure 5.30 the projection of the wall losses in ϕ (fig. 5.30a) and θ (fig. 5.30b) are shown.

The blue area in ϕ projection is the area where the particles born. The ϕ projection shows that adding EC power the first orbit losses slightly increase of 2% (numbers in the legend) and the particles make a longer toroidal path before colliding the wall (the peak moves right). The θ distribution doesn't change much, apart from the magnitude.

The EC wave injection makes stronger variation in the wall distribution if we consider the total losses (i.e. prompt losses and diffusive losses) as shown in figure 5.31. This is given by the fact that the slowing-down time increases with EC power and the particles have more time to enter in unconfined orbits. In toroidal angle there is an almost uniform increase in magnitude (losses increase by roughly 17%. In poloidal angle distribution, the particles get lost in the same area but the amount of markers increases of a factor 4.

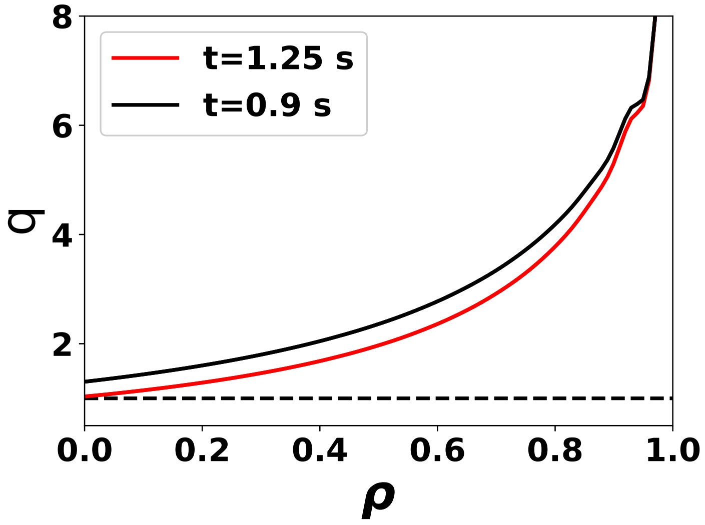

FIGURE 5.29: q-profile without EC (black) and with EC (red)

5.6.5 Initial position of lost EP

In this section, the initial position of the lost particles are studied. The results shown here consider only the markers which get lost to the wall. In figure 5.32 the initial ρ position of the markers is shown. Without EC (figure 5.32a) there is a step in the initial borning position corresponding to $\rho \sim 0.75$; this step is strongly reduced when EC power is added (figure 5.32b).

In figure 5.33 the R (major radius) position of EP born position is shown, with distinction between first orbit losses (red) and diffusive orbit losses (blue). A loss is considered first orbit if the EP lost energy is less than 0.5 keV. The prompt lost particles in both cases are mostly generated in the high field side of the plasma, exception made for a small contribution from the edge at the low field side. The EC injection makes the prompt losses to reduce (from 48.8% to 33.2%) with respect to the total losses, but this does not imply a reduced wall loads given by this particles because of the overall increase of losses.

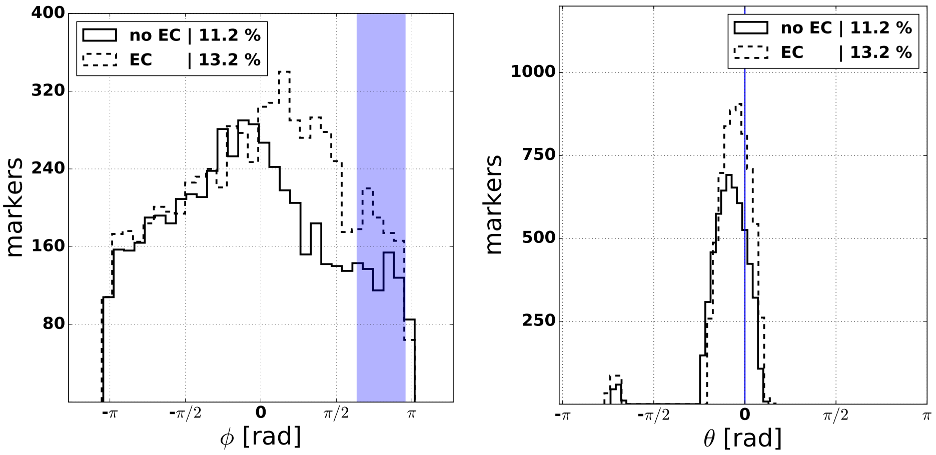

(A) Toroidal projection of wall losses (B) Poloidal projection of wall losses

FIGURE 5.30: First orbit losses with and without EC. Blue area indicates where particles are born.

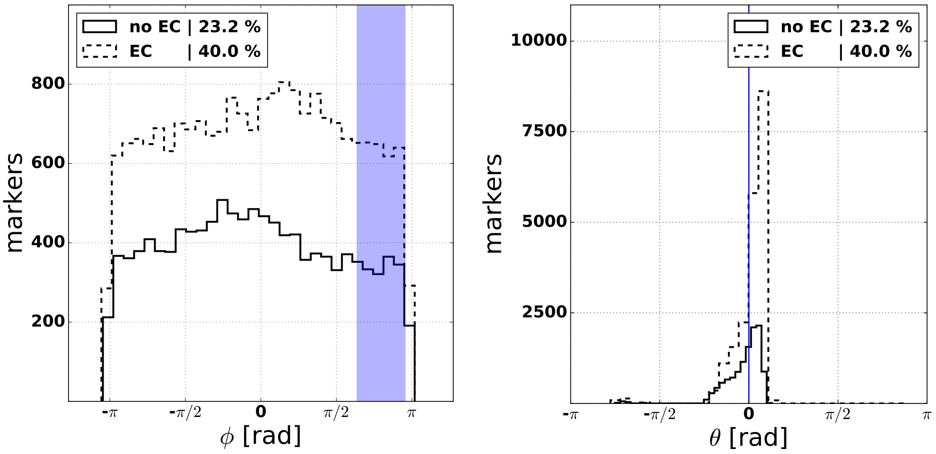

(A) Toroidal projection of wall losses (B) Poloidal projection of wall losses

FIGURE 5.31: Total orbit losses with and without EC. Blue area indicates where particles are born.

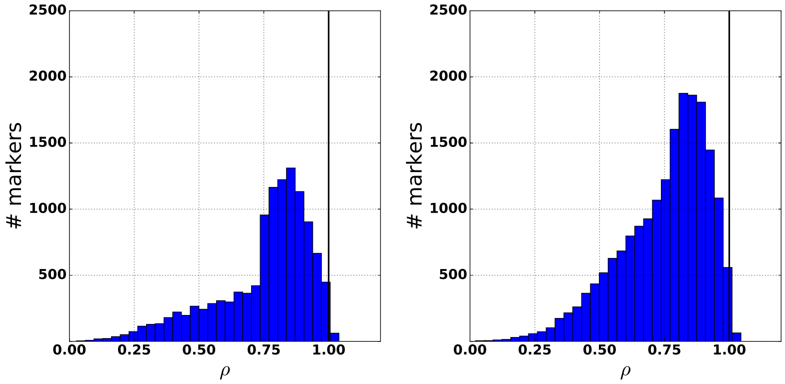

(A) ρ born position without EC (B) ρ born position with EC

FIGURE 5.32: ρ born position with and without EC.

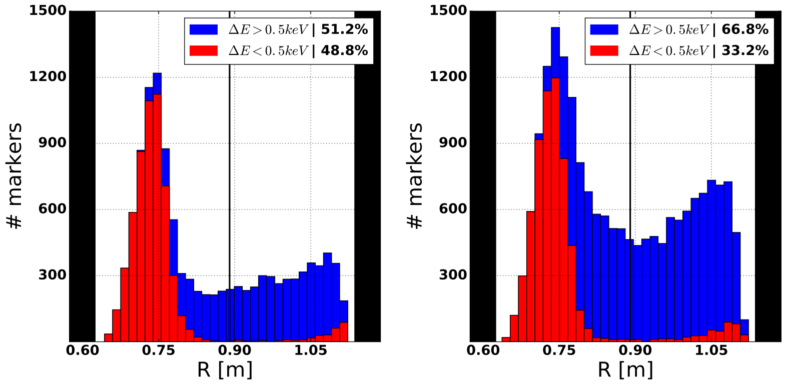

(A) Without EC (B) With EC

FIGURE 5.33: Major radius born position for first orbit losses and total losses with and without EC power.

5.7 Conclusion

In this chapter, the results of interpretative modelling activity on TCV advanced tokamak scenarios have been presented.

At first an overview of TCV neutral beam injector has been presented. The beam operated for three years so far, mostly at maximum particle acceleration (25 kV) and injected total energy (0.8 MJ) attainable. Nevertheless, also lower energies and powers are used since NBI could stabilise the plasma MHD activity by plasma rotation.

The energy injected is limited to 0.8 MJ because of the beam optics, which is different from the expected one. The foreseen beam divergence is 20×12mrad while the measured one is 36×8mrad due to incorrect fabrication of the beam acceleration grids. This measurement has been done with an in-house built device which consist of a W movable tile (along the beam direction) where the beam collides. The particles collide with the duct wall and then heat it up, causing unexpected impurity injection in the plasma. New grids are expected to be mounted and used, in order to be capable to reach the desired injected energy of 2 MJ.

H-mode plasmas with edge localised modes have been obtained using only the additional power of the beam. These scenarios can be a basis for the ITER-relevant H-modes developed in TCV.

The interpretative modelling activity has been carried out with NUBEAM and ASCOT. TCV data have been interfaced with NUBEAM/TRANSP through the OMFIT modelling framework. Beam geometries in ASCOT and NUBEAM are given in two different ways (the former is a beamlet-by-beamlet model, the second a narrow-beam model) so a comparison between the two ionisation positions of the markers has been made. The comparison gives good agreement, considering the different models used. A comparison between the two codes also after the calculation of the EP slowing-down has been carried out by setting to minimum the charge-exchange losses in NUBEAM (minimizing the neutral density). The agreement within the two codes is satisfying, still considering that some remaining power is lost through charge-exchange. This confirms that the two codes can be used for TCV simulations, bearing in mind that for plasma scenario NUBEAM is the most suitable tool, while for 3D calculations ASCOT can be used.

Advanced tokamak plasmas have been carried out at TCV within the EUROfusion framework and during internal campaigns. The additional power coming from the beam allows to obtain higher β_N values and current drive, as well as a strong population of energetic particles. In TCV AT plasmas we obtain an increase in β_N using the beam but the electron thermal energy content seems not to follow the same trend with increasing NB power.

Interpretative modelling has been carried out to assess the impact of EC heating on EP power deposition and slowing down. EC heating on TCV plasma has not only the effect of temperature increase and density pump-out: the impurity content changes as well and the measurement of edge neutral density get distorted. These effects have been kept in consideration when modelling NBI on EC-heated plasmas because of the impact they can have on charge-exchange losses.

NUBEAM interpretative modelling on a selected shot (number 58 823) shows that increasing the EC power injected in the plasma the NB injected power decreases, increasing both the orbit losses and the charge-exchange losses. The shine-through remains almost constant to 10%. Furthermore, the absorbed power is differently redistributed among electrons and ions, with higher absorption by ions with increasing EC power. This can be explained by the increase in T_e, which represents an increase in the critical energy (and slowing-down time). The shielded driven current increases, probably because of the increased slowing-down time and different transport of fast ions. The energy and pitch (projection of velocity on the direction parallel to the magnetic field) distribution change as well: the high losses make the energy distribution to get far from the $1/E$ typical slowing-down trend and peaks at the injection energy, typical of high losses, can be seen. The pitch distribution has a slight change in magnitude but the shape is not much affected.

ASCOT has been used to impact the 3D wall losses of the particles. ASCOT cannot compute yet charge-exchange losses, so it has been applied only for orbit losses. The losses increase of 70% when EC power is added. Without EC, they focus poloidally on the midplane and increase toroidally in the beam injection direction. With EC, a stronger concentration of the losses is seen the outer midplane. This is due to the fact that the density pump-out makes more particles born in the unconfined position, leading to higher losses in the low-field side. The first orbit losses (loss of energy below 0.5 keV) born mostly in the high-field side, while the total losses are spread all over the radial positions. Adding EC, the fraction of first orbit losses decreases, but still the overall amount increases. The shape of the q-profile in the two cases is quite similar, meaning that the magnetic field is not that different between the two cases. The increase in losses is mainly due by the different plasma profiles: a longer slowing-down time means a higher probability for the particles to get into unconfined orbits and then get lost.

This modelling activity outlines some unexpected EP behaviour in TCV advanced tokamak plasmas, with all the additional power available. This effect is due to the change in the plasma properties when adding ECRH. In TCV this phenomenology is quite harmful because in order to get satisfying AT scenarios there will be needing for both the additional heating systems, but the interplay between them seems detrimental for NBI power deposition and could explain why the target value of $\beta_N = 2.5$ has not been reached. An open question remains about NBI performance in H-mode scenarios, which would be probably used in next experimental campaign.

The models here used could be improved by adding the fast ion-fast ion collision term, which in TCV device could cause different physics behaviour to happen: in fact in TCV the EP density can reach up to 20% of the electron density, thus the collisions of fast ions within themself is no more negligible. Nevertheless, comparison with experimental data (such as neutron fluency and neutral energy spectrum) are foreseen to further validate the behaviour of fast ions in TCV AT tokamak plasmas.

Afterword

The work carried out during the three years of Ph.D. has been presented in this thesis. Magnetic confinement thermonuclear fusion relies on the injection of fast particles in the plasma in order to achieve the necessary temperatures for self-sustaining fusion reactions. The behaviour of the fast particles in standard and advanced tokamak plasmas has been studied using analytical models and Monte Carlo codes.

RFX-mod device is a medium-size device that can be used as a tokamak and nowadays it is under upgrade. Among the upgrades, the implementation of a neutral beam injector was took in consideration; METIS analytical code has been used to assess the impact of the beam fast particles on a set of standard tokamak plasmas in RFX-mod. At first, some discharges have been chosen and their behaviour has been reproduced for the first time within METIS. The results show that shine-through is a critical issue due to the fixed injection geometry of the beam, thus beam injection is secure only at higher plasma densities ($>1 \times 10^{19}\,\mathrm{m}^{-3}$). In these cases, current drive is negligible but the power deposited in the plasma allows to reach $T_i/T_e > 1$ regimes. Nevertheless the threshold for entering H-mode confinement regime is overpassed with neutral beam injection, allowing to widen the operational space of the machine and studying the impact of active saddle coils magnetic fields on edge localized modes. Monte Carlo code NUBEAM has been applied as well, checking if the approximations made in METIS are well-posed in case of low-field plasma such as RFX-mod. The comparison shows that the power lost by METIS is underestimated

One of the most advanced devices for studying neutral beam injection will be JT-60SA, under construction in Japan and foreseen to achieve the first plasma in 2020. The set of 14 neutral beam injectors has been implemented in ASCOT Monte Carlo modeling tool for predictive studies on the fast particles behaviour. The results show that neutral beam injection has low losses and come mostly from the counter-current injected positive beams, as expected. The high amount of power deposited to ions (electrons) by positive (negative) beams is necessary in order to achieve the performances requested, in particular considering advanced tokamak scenarios where the current induced by the negative neutral beams is fundamental to have a fully non-inductive scenario. The behaviour of fast particles with different plasma composition (i.e. Z_{eff}) has been studied, enhancing the importance of a correct impurity model also for neutral beam injection predictive modeling. Since the highly energetic particles injected with negative beams ($E_{INJ} = 500\,\mathrm{keV}$) will interact with Alfvén eigenmodes, also lower injection energies have been studied and this will pave the way for studies on wave-particle interaction. Now that the injection system is implemented in ASCOT, the torque injected by the beams will be studied, the impact of the beams during current ramp-up and ramp-down will be assessed and a power scan of the negative neutral beams will be performed in order to check the flexibility of the system.

Neutral beam injection heating has been possible in TCV since three years, when the beam has been installed and commissioned. The beam system is now operated routinely (also used in real time for β control) and upgrades will involve an optimization of the beam optics. The tools for modeling have been set-up in the framework of this thesis: NUBEAM has been interfaced with TCV data within the OMFIT suite and TCV beam geometry has been implemented in ASCOT. Comparison between the two injection geometries show good agreement. These tools have been applied to advanced tokamak scenarios in order to assess the impact that electron cyclotron wave injection has on neutral beam-injected energetic particles. The studies show that with increasing ECRH power the lost power increases, both in charge-exchange and orbit losses channels. Nevertheless, the change in plasma composition make the neutral beam induced current to remain the same, if not to increase. The particles lost to the wall increase as well with increasing wave injection power and the losses tend to concentrate in the outer midplane. Due to the high fraction of energetic particles in TCV plasmas, the numerical models applied up to now should be widened with the implementation of fast ion-fast ion collisions.

5.8 My personal contributions and publications

5.8.1 Contribution and proceeding in international conferences

- **M. Vallar**, J.F. Artaud, T. Bolzonella, H. Sakakita, M. Valisa, P. Vincenzi, *Requirements and modelling of fast particle injection in RFX-mod tokamak plasmas*, Prague (Czech Republic), 29th SOFT, 5-9 September 2016, poster contribution P4.028 **M. Vallar**, T. Bolzonella, R. Coelho, J. Garcia, T. Kurki-Suonio, L. Pigatto, K. Sarkimaki, J. Varje, M. Romanelli, *Neutral beam injection modelling in JT-60SA axisymmetric equilibria*, 44th EPS Conference, Belfast (United Kingdom), 26-30 June 2017, poster contribution P1.149

- **M. Vallar**, T. Bolzonella, R. Coelho, J. Garcia, T. Kurki-Suonio, L. Pigatto, K. Sarkimaki, J. Varje, M. Romanelli *Neutral beam deposition profiles in JT-60 SA at various plasma composition and different injection energies*, FISMAT 2017, Trieste (Italy), 1-5 October 2017, poster contribution

- P. Vincenzi, J. V., P. Agostinetti, J. F. Artaud, T. Bolzonella, T. Kurki-Suonio, Massimiliano Mattei, P. Sonato, **M. Vallar**, *Estimate of 3D power wall loads due to Neutral Beam Injection in EU DEMO ramp-up phase*, International Conference on Plasma Surface Interactions in Controlled Fusion Devices, Princeton University (NJ-USA), 17-22 June 2018, poster contribution 448

- **M. Vallar**, M. Agostini, T. Bolzonella, S. Coda, J. Garcia, B. Geiger, T. Goodman, M. Gorelenkova, A.N. Karpushov, T. Kurki-Suonio, C. Piron,

L. Pigatto, O. Sauter, N. Vianello, P. Vincenzi, M. Yoshida the TCV team and the MST1 team, *Nonlinear contribution of neutral beam injection in TCV EC-heated advanced tokamak scenarios*, 45th EPS Conference, Prague (Czech Republic) 02-06 July 2018, poster contribution P2.1068

- G. Granucci, S. Garavaglia, P. Agostinetti, T. Bolzonella, A. Cardinali, C. Castaldo, S. Ceccuzzi, D. Farina, L. Figini, R. Maggiora, D. Milanesio, A. Moro, G. Ravera, D. Ricci, **M. Vallar**, P. Vincenzi, *Expected performances of the DTT heating systems*, Prague (CZ), 45th EPS Conference, Prague (Czech Republic) – 02-06 July 2018, poster contribution P4.1071

- **M. Vallar**, A. N. Karpushov, M. Agostini, T. Bolzonella, S. Coda, B. P. Duval, A. Fasoli, B. Geiger, R. Jacquier, R. Maurizio, A. Pimazzoni, C. Piron, G. Serianni, D. Testa, M. Valisa, P. Veltri, N. Vianello, the TCV Team and the EUROfusion MST1 Team, *Status, scientific results and technical improvements of the NBH on TCV tokamak*, Taormina (Italy), 30th SOFT,16-21 September 2018, poster contribution P3.011

- P. Agostinetti, T. Bolzonella, P. Sonato, **M. Vallar**, P. Vincenzi, *Conceptual design of a Neutral Beam Heating system for DTT*, Taormina (Italy), 30th SOFT,16-21 September 2018, poster contribution P1.019

- G. Granucci, P. Agostinetti, T. Bolzonella, A. Bruschi, A. Cardinali, C. Castaldo, S. Ceccuzzi, F. Crisanti, L. Figini, S. Garavaglia, R. Maggiora, D. Milanesio, A. Moro, G. Ravera, P. Sonato, A. Tuccillo, **M. Vallar**, P. Vincenzi, *The heating systems capability of DTT*, Taormina (Italy), 30th SOFT,16-21 September 2018, poster contribution P3.025

- C. Piron, M. Agostini, M. Fontana, J. Garcia, G. Giruzzi, M. Gobbin, T. Goodman, A. Karpushov, A. Merle, J. Morales, S. Nowak, L. Pigatto, O. Sauter, D. Testa, **M. Vallar**, M. Yoshida, *Extension of the Operating Space of High-"β_N" Fully Non-inductive Scenarios on TCV Using Neutral Beam Injection*, Gandhinagar (India), 27th IAEA Fusion Energy Conference, 22-27 October 2018, poster contribution 169

- J. Garcia, C. Piron, T. Goodman, M. Agostini, M. Fontana, G. Giruzzi, M. Gobbin, A. Karpushov, M. Kong, A. Merle, J. Morales, S. Nowak, L. Pigatto, O. Sauter, D. Testa, M.Vallar, M. Yoshida, the TCV team and the MST1 team, *Optimization of high beta steady-state scenarios at TCV in support of JT-60SA*, Kanazawa (Japan), 2nd Asia-Pacific Conference on Plasma Physics (AAPPS-DPP2018), 12-17 November 2018, oral contribution

- **M. Vallar**, P. Vincenzi, R. Albanese, R. Ambrosino, J.F. Artaud, T. Bolzonella, A. Cardinali, A. Castaldo, S. Ceccuzzi, F. Crisanti, D. Farina, S. Garavaglia, G. Giruzzi, G. Granucci, P. Mantica, P. Martin, A. Pizzuto, G. Ramogida, G. Vlad, F. Zonca, *Integrated physical assessment of DTT reference scenarios*, Kanazawa (Japan), 2nd Asia-Pacific Conference on Plasma Physics (AAPPS-DPP2018), 12-17 November 2018, poster contribution

5.8.2 Publications in refereed journals

- **M. Vallar**, J.F. Artaud, T. Bolzonella, H. Sakakita, M. Valisa, P. Vincenzi, *Requirements and modelling of fast particle injection in RFX-mod tokamak plasmas*, Fusion Engineering and Design, 123, 349-352, 2017

- S. Peruzzo, (...) **M. Vallar** et al., *Overview of the RFX-mod fusion science activity*, Nuclear Fusion, 57(10), 102012, 2017

- P. Vincenzi, J. V., P. Agostinetti, J. F. Artaud, T. Bolzonella, T. Kurki-Suonio, Massimiliano Mattei, P. Sonato, **M. Vallar**, *Estimate of 3D power wall loads due to Neutral Beam Injection in EU DEMO ramp-up phase*, submitted to Nuclear Materials and Energy, 2018

- **M. Vallar**, A. N. Karpushov, M. Agostini, T. Bolzonella, S. Coda, B. P. Duval, A. Fasoli, B. Geiger, R. Jacquier, R. Maurizio, A. Pimazzoni, C. Piron, G. Serianni, D. Testa, M. Valisa, P. Veltri, N. Vianello, the TCV Team and the EUROfusion MST1 Team, *Status, scientific results and technical improvements of the NBH on TCV tokamak*, submitted to Fusion Engineering and Design

Bibliography

[1] *United Nations Energy Statistics yearbook*. 2017. URL: `https://unstats.un.org/unsd/energy/`.

[2] *United Nations Human Development Report*. 2016. URL: `http://hdr.undp.org/en/`.

[3] *International agreements on climate action*. URL: `http://www.consilium.europa.eu/en/policies/climate-change/international-agreements-climate-action/`.

[4] J. P. Freidberg. *Plasma physics and fusion energy*. Cambridge University Press, 2008.

[5] R.F. Post et al. "Concept for a High-Power-Density Mirror Fusion Reactor". In: *Phys. Rev. Lett.* 31 (5 1973), pp. 280–282.

[6] J. D. Lawson. "Some criteria for a power producing thermonuclear reactor". In: *Proceedings of the Physical Society.Section B* 70.1 (1957), p. 6.

[7] *ITER website*. URL: `https://www.iter.org`.

[8] P. Vincenzi. *Interaction between neutral beam fast particles and plasma in fusion experiments*. 2016.

[9] L. Spitzer. *Physics of fully ionized gases*. Courier Corporation, 2006.

[10] H. Eubank et al. *PLT neutral beam heating results*. International Atomic Energy Agency (IAEA): IAEA, 1979.

[11] J. D. Strachan et al. "Fusion power production from TFTR plasmas fueled with deuterium and tritium". In: *Physical Review Letters* 72.22 (1994), p. 3526.

[12] R. J. Hawryluk et al. "Confinement and heating of a deuterium-tritium plasma". In: *Physical Review Letters* 72.22 (1994), p. 3530.

[13] M. Keilhacker et al. "High fusion performance from deuterium-tritium plasmas in JET". In: *Nuclear Fusion* 39.2 (1999), p. 209.

[14] R.J. Hawryluk. "Results from deuterium-tritium tokamak confinement experiments". In: *Reviews of modern physics* 70.2 (1998), p. 537.

[15] M. Kikuchi et al. *Fusion physics*. 2012.

[16] A. C. Riviere. "Penetration of fast hydrogen atoms into a fusion reactor plasma". In: *Nuclear Fusion* 11.4 (1971), p. 363.

[17] C. D. Boley et al. "Enhancement of the neutral-beam stopping cross section in fusion plasmas due to multistep collision processes". In: *Physical Review Letters* 52.7 (1984), p. 534.

[18] K. Miyamoto. *Plasma Physics and Controlled Nuclear Fusion*. en. Google-Books-ID: QFdPEzEzfwsC. Springer Science & Business Media, Mar. 2006. ISBN: 978-3-540-28097-2.

[19] T. H. Stix. “Heating of toroidal plasmas by neutral injection”. In: *Plasma Physics* 14.4 (1972), p. 367.

[20] W. W. Heidbrink. “Basic physics of Alfvén instabilities driven by energetic particles in toroidally confined plasmas”. In: *Physics of Plasmas* 15.5 (2008), p. 055501.

[21] D. R. Mikkelsen et al. “Optimization of steady-state beam-driven tokamak reactors”. In: *Nuclear Technology-Fusion* 4.2P1 (1983), pp. 237–252.

[22] M. Honda et al. “Collisionality dependence of a shielding factor of a beam driven current”. In: *Nuclear Fusion* 52.2 (2012), p. 023021.

[23] D. R. Baker et al. “Toroidal rotation in neutral beam heated discharges in DIII-D”. In: *Nuclear fusion* 43.2 (2003), p. 142.

[24] F. D. Halpern et al. “Predictive simulations of ITER including neutral beam driven toroidal rotation”. In: *Physics of Plasmas* 15.6 (2008), p. 062505.

[25] B. Geiger et al. “Fast-ion D-alpha measurements at ASDEX Upgrade”. In: *Plasma Physics and Controlled Fusion* 53.6 (2011), p. 065010.

[26] W. Mandl et al. “Beam emission spectroscopy as a comprehensive plasma diagnostic tool”. In: *Plasma physics and controlled fusion* 35.10 (1993), p. 1373.

[27] J. F. Artaud et al. “Metis: a fast integrated tokamak modelling tool for scenario design”. In: *Nuclear Fusion* 58.10 (2018), p. 105001.

[28] R. J. Goldston et al. “New techniques for calculating heat and particle source rates due to neutral beam injection in axisymmetric tokamaks”. In: *Journal of computational physics* 43.1 (1981), pp. 61–78.

[29] A. Pankin et al. “The tokamak Monte Carlo fast ion module NUBEAM in the National Transport Code Collaboration library”. In: *Computer Physics Communications* 159.3 (2004), pp. 157–184.

[30] O. Asunta et al. “Modelling neutral beams in fusion devices: Beamlet-based model for fast particle simulations”. English. In: *Computer Physics Communications* 188 (2015), pp. 33–46.

[31] E. Hirvijoki et al. “ASCOT: Solving the kinetic equation of minority particle species in tokamak plasmas”. English. In: *Computer Physics Communications* 185.4 (2014), pp. 1310–1321.

[32] J. A. Heikkinen et al. “Monte Carlo simulation of runaway electrons in a toroidal geometry”. In: *Computer physics communications* 76.2 (1993), pp. 215–230.

[33] L. G. Eriksson et al. “Dynamics of energetic ion orbits in magnetically confined plasmas Plasma Phys”. In: *Control. Fusion* 43 (2001).

[34] R. J. Hawryluk. "An empirical approach to tokamak transport". In: *Physics of plasmas close to thermonuclear conditions*. Elsevier, 1981, pp. 19–46.

[35] M. Keilhacker et al. "H-mode confinement in tokamaks". In: *Plasma Physics and Controlled Fusion* 29.10A (1987), p. 1401.

[36] F. Wagner. "A quarter-century of H-mode studies". In: *Plasma Physics and Controlled Fusion* 49.12B (2007), B1.

[37] F. Wagner et al. "Development of an Edge Transport Barrier at the H-Mode Transition of ASDEX". In: *Phys. Rev. Lett.* 53 (15 1984), pp. 1453–1456.

[38] J. W. Connor et al. "A review of theories of the LH transition". In: *Plasma Physics and Controlled Fusion* 42.1 (2000), R1.

[39] Y. R. Martin et al. "Power requirement for accessing the H-mode in ITER". In: *Journal of Physics: Conference Series* 123.1 (2008), p. 012033.

[40] J. D. Galambos et al. "Commercial tokamak reactor potential with advanced tokamak operation". In: *Nuclear Fusion* 35.5 (1995), p. 551.

[41] E. Joffrin. "Advanced tokamak scenario developments for the next step". In: *Plasma Physics and Controlled Fusion* 49.12B (2007), B629.

[42] A. C. C. Sips et al. "Advanced scenarios for ITER operation". In: *Plasma physics and controlled fusion* 47.5A (2005), A19.

[43] A. G. Peeters. "The bootstrap current and its consequences". In: *Plasma Physics and Controlled Fusion* 42.12B (2000), B231.

[44] R. C. Wolf. "Internal transport barriers in tokamak plasmas". In: *Plasma Physics and Controlled Fusion* 45.1 (2002), R1.

[45] M. E. Puiatti et al. "Overview of the RFX-mod contribution to the international Fusion Science Program". In: *Nuclear Fusion* 55.10 (2015), p. 104012.

[46] M. Valisa et al. "High current regimes in RFX-mod". In: *Plasma Physics and Controlled Fusion* 50.12 (2008), p. 124031.

[47] R. Lorenzini et al. "Self-organized helical equilibria as a new paradigm for ohmically heated fusion plasmas". In: *Nature Physics* 5.8 (2009), p. 570.

[48] S. Peruzzo et al. "Design of machine upgrades for the RFX-mod experiment". In: *29th SOFT Symposium on Fusion Technlogy*. 2016.

[49] M. Gobbin et al. "Resonance between passing fast ions and MHD instabilities both in the tokamak and the RFP configurations". In: *Nuclear Fusion* 48.7 (2008), p. 075002.

[50] J. Waksman et al. "Neutral beam heating of a RFP plasma in MST". In: *Physics of Plasmas (1994-present)* 19.12 (2012), p. 122505.

[51] Y. Hirano et al. "Reversed Field Pinch experiment on a new large machine, TPE-RX". In: *17th Fusion energy conference*. 1999.

[52] J.K. Anderson et al. “Simulation of a Power Neutral Beam Injection in RFX-Mod”. In: *38th EPS conference on Plasma Physics*. 2011.

[53] H. Sakakita et al. “Characteristics of high-power-density and focused neutral beam system”. In: *32nd Conf. Plasma Physics Control. Fus., Terragona*. 2005, P4.

[54] H. Sakakita et al. “Development of strongly focused high-current-density ion beam system and its application for the alpha particle measurement in ITER”. In: *Proc. 21st IAEA Fusion Energy Conf.* 2007.

[55] S. Dal Bello et al. “Integration design of TPE-RX Neutral Beam Injector on RFX-mod”. In: *Fusion Engineering and Design* 86.6–8 (Oct. 2011), pp. 772–775.

[56] N. Pilan et al. “The Monte Carlo Simulation of a 1-MW Neutral Beam Injector on RFX-Mod”. In: *Plasma Science, IEEE Transactions on* 40.4 (2012), pp. 1042–1052.

[57] M. Vallar et al. “Requirements and modelling of fast particle injection in RFX-mod tokamak plasmas”. In: *Fusion Engineering and Design* 123 (2017). Proceedings of the 29th Symposium on Fusion Technology (SOFT-29) Prague, Czech Republic, September 5-9, 2016, pp. 349 –352. ISSN: 0920-3796.

[58] L. Marrelli et al. “Tokamak experiments in RFX-mod with polarized insertable electrode”. In: *43rd EPS Conference on Plasma Physics, Leuven*. 2016.

[59] Y. Kamada et al. “Plasma regimes and research goals of JT-60SA towards ITER and DEMO”. In: *Nuclear Fusion* 51.7 (2011), p. 073011.

[60] H. Shirai et al. “Progress of JT-60SA Project: EU-JA joint efforts for assembly and fabrication of superconducting tokamak facilities and its research planning”. In: *Fusion Engineering and Design* 109 (2016), pp. 1701–1708.

[61] VV.AA. *JT-60SA Research Plan - Research Objectives and Strategy Version 4.0*. 2018.

[62] L. Garzotti et al. “Analysis of JT-60SA operational scenarios”. In: *Nuclear Fusion* 58.2 (2018), p. 026029.

[63] S. Ishida et al. “Overview of the JT-60SA project”. In: *Nuclear Fusion* 51.9 (2011), p. 094018.

[64] G. Giruzzi et al. “Physics and operation oriented activities in preparation of the JT-60SA tokamak exploitation”. In: *Nuclear Fusion* 57.8 (2017), p. 085001.

[65] A. Kojima et al. “Demonstration of long-pulse acceleration of high power positive ion beam with JT-60 positive ion source in Japan–Korea joint experiment”. In: *Fusion Engineering and Design* 102 (2016), pp. 81–87.

[66] A. Kojima et al. “Achievement and improvement of the JT-60U negative ion source for JT-60 Super Advanced”. In: *Review of Scientific Instruments* 81.2 (2010), 02B112.

[67] A. Kojima et al. “Achievement of 500 keV negative ion beam acceleration on JT-60U negative-ion-based neutral beam injector”. In: *Nuclear Fusion* 51.8 (2011), p. 083049.

[68] A. Kojima et al. “100 s extraction of negative ion beams by using actively temperature-controlled plasma grid”. In: *Review of Scientific Instruments* 85.2 (2014), 02B312.

[69] A. Kojima et al. “Progress in long-pulse production of powerful negative ion beams for JT-60SA and ITER”. In: *Nuclear Fusion* 55.6 (2015), p. 063006.

[70] M. Yoshida et al. “22 A beam production of the uniform negative ions in the JT-60 negative ion source”. In: *Fusion Engineering and Design* 96 (2015), pp. 616–619.

[71] J. Garcia et al. “Physics comparison and modelling of the JET and JT-60U core and edge: towards JT-60SA predictions”. In: *Nuclear Fusion* 54.9 (2014), p. 093010.

[72] M. Schneider et al. “Simulation of the neutral beam deposition within integrated tokamak modelling frameworks”. In: *Nuclear Fusion* 51.6 (2011), p. 063019.

[73] M. Schneider et al. “On alpha particle effects in tokamaks with a current hole”. In: *Plasma Physics and Controlled Fusion* 47.12 (2005), p. 2087.

[74] N. Oyama et al. “Long-pulse hybrid scenario development in JT-60U”. In: *Nuclear Fusion* 49.6 (2009), p. 065026.

[75] B. J. Green et al. “ITER: burning plasma physics experiment”. In: *Plasma physics and controlled fusion* 45.5 (2003), p. 687.

[76] K. Tobita et al. “Compact DEMO, SlimCS: design progress and issues”. In: *Nuclear Fusion* 49.7 (2009), p. 075029.

[77] N. Hayashi et al. “Transport modelling of JT-60U and JET plasmas with internal transport barriers towards prediction of JT-60SA high-beta steady-state scenario”. In: *Nuclear Fusion* 57.12 (2017), p. 126037.

[78] N. Hayashi et al. “Predictive modelling of JT-60SA high-beta steady-state plasma with impurity accumulation”. In: *Nuclear Fusion* 58.6 (2018), p. 066001.

[79] S. Coda et al. “Overview of the TCV tokamak program: scientific progress and facility upgrades”. In: *Nuclear Fusion* 57.10 (2017), p. 102011.

[80] H. Meyer et al. “Overview of progress in European medium sized tokamaks towards an integrated plasma-edge/wall solution”. In: *Nuclear Fusion* 57.10 (2017), p. 102014.

[81] A. Fasoli et al. “TCV heating and in-vessel upgrades for addressing DEMO physics issues”. In: *Nuclear Fusion* 55.4 (2015), p. 043006.

[82] A. N. Karpushov et al. “Upgrade of the TCV tokamak, first phase: Neutral beam heating system”. In: *Fusion Engineering and Design* (2015).

[83] A. Sorokin et al. “Characterization of 1 MW, 40 keV, 1 s neutral beam for plasma heating”. In: *Review of Scientific Instruments* 81.2 (2010), 02B108.

[84] A. N. Karpushov et al. “A scoping study of the application of neutral beam heating on the TCV tokamak”. In: *Fusion Engineering and Design* 86.6 (2011), pp. 868–871.

[85] D. Fasel et al. “Supply equipment to the new NBH system for the TCV tokamak”. In: *Fusion Engineering and Design* 96–97 (Oct. 2015), pp. 447–451.

[86] M. Vallar et al. “"Status, scientific results and technical improvements of the NBH on TCV tokamak"”. In: *Fusion Engineering and Design (Submitted to)* (2018).

[87] O. Meneghini et al. “Integrated modeling applications for tokamak experiments with OMFIT”. In: *Nuclear Fusion* 55.8 (2015), p. 083008.

[88] *OMFIT website*. URL: `https://gafusion.github.io/OMFIT-source/`.

[89] B. Geiger et al. “Fast-ion transport in low density L-mode plasmas at TCV using FIDA spectroscopy and the TRANSP code”. In: *Plasma Physics and Controlled Fusion* 59.11 (2017), p. 115002.

[90] O. Sauter et al. “Steady-state fully noninductive current driven by electron cyclotron waves in a magnetically confined plasma”. In: *Physical review letters* 84.15 (2000), p. 3322.

[91] S. Coda et al. “High-bootstrap, noninductively sustained electron internal transport barriers in the Tokamak à Configuration Variable”. In: *Physics of plasmas* 12.5 (2005), p. 056124.

[92] *EUROfusion MST website*. URL: `https://www.euro-fusion.org/devices/medium-sized-tokamaks/`.

[93] T. P. Goodman et al. “Safety factor profile requirements for electron ITB formation in TCV”. In: *Plasma Physics and Controlled Fusion* 47.12B (2005), B107.

[94] Z. A. Pietrzyk et al. “Long-Pulse Improved Central Electron Confinement in the TCV Tokamak with Electron Cyclotron Heating and Current Drive”. In: *Phys. Rev. Lett.* 86 (8 2001), pp. 1530–1533.

[95] O. Sauter et al. “Inductive Current Density Perturbations to Probe Electron Internal Transport Barriers in Tokamaks”. In: *Phys. Rev. Lett.* 94 (10 2005), p. 105002.

[96] J. Garcia et al. “Critical threshold behavior for steady-state internal transport barriers in burning plasmas”. In: *Physical review letters* 100.25 (2008), p. 255004.

[97] U. Kruezi et al. “JET divertor diagnostic upgrade for neutral gas analysis”. In: *Review of Scientific Instruments* 83.10 (2012), p. 10D728.

[98] O. Sauter et al. “Neoclassical conductivity and bootstrap current formulas for general axisymmetric equilibria and arbitrary collisionality regime”. In: *Physics of Plasmas* 6.7 (1999), pp. 2834–2839.

[99] O. Sauter et al. “Erratum: “Neoclassical conductivity and bootstrap current formulas for general axisymmetric equilibria and arbitrary collisionality regime” [Phys. Plasmas 6, 2834 (1999)]”. In: *Physics of Plasmas* 9.12 (2002), pp. 5140–5140.

[100] F. L. Hinton et al. “Theory of plasma transport in toroidal confinement systems”. In: *Rev. Mod. Phys.* 48 (2 1976), pp. 239–308.

[101] J.M. Moret et al. “Fast single loop diamagnetic measurements on the TCV tokamak”. In: *Review of Scientific Instruments* 74.11 (2003), pp. 4634–4643.